12/10-2-91 9850 (1)

UCRL-ID-106159

Prototype Engineered Barrier System Field Test (PEBSFT) Final Report

Contributing Authors: Thomas Buscheck
Richard Carlson
William Daily
Kenrick Lee
Wunan Lin
Nai-hsien Mao
Abelardo Ramirez
Tzou-Shin Ueng
Herbert Wang
Donald Watwood

Scientific Editor: Abelardo L. Ramirez

Manuscript Date: October 1990
Publication Date: August 1991

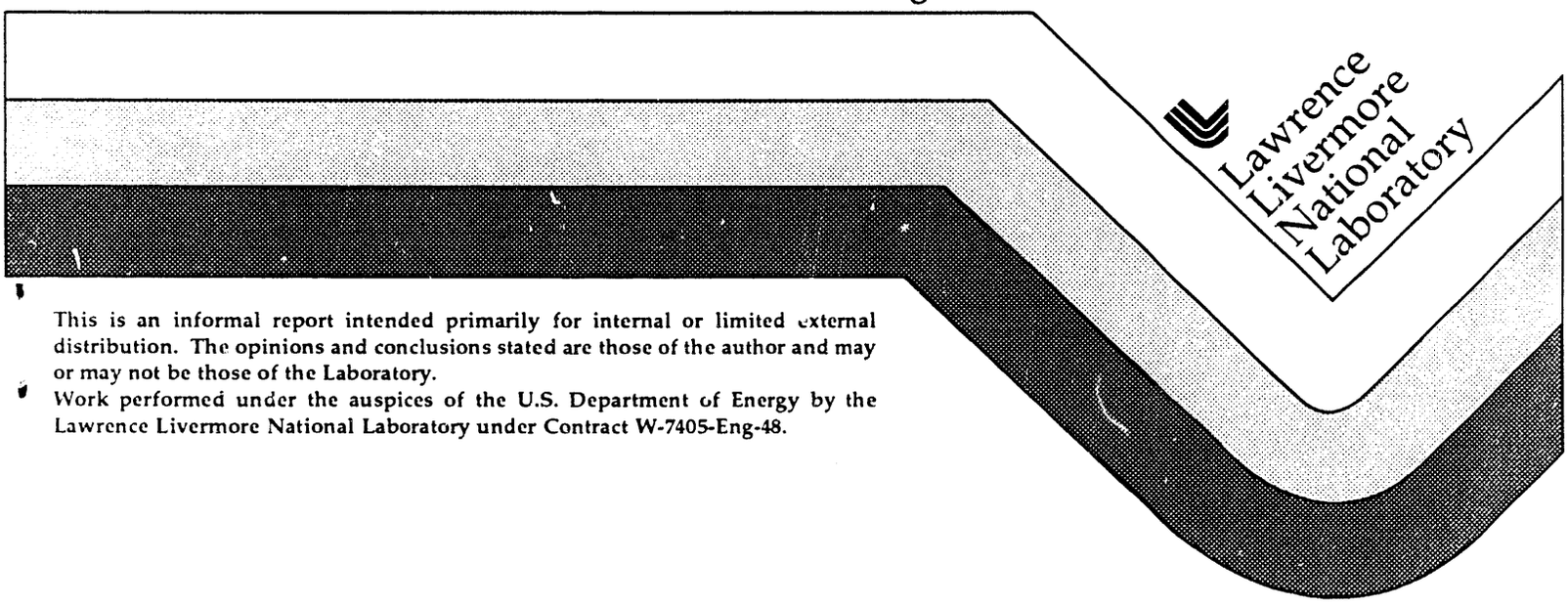

Work performed under the auspices of the U.S. Department of Energy by the Lawrence Livermore National Laboratory under Contract W-7405-Eng-48.

DISCLAIMER

Prepared by Yucca Mountain Site Characterization Project (YMP) participants as part of the Civilian Radioactive Waste Management Program. The YMP is managed by the Yucca Mountain Site Characterization Project Office of the U.S. Department of Energy, Las Vegas, Nevada.

UCRL-ID--106159

DE92 000102

Prototype Engineered Barrier System Field Test (PEBSFT)

Final Report

Manuscript date: May 1990

Contents

Acronyms and Abbreviations

DAS	data acquisition system
DOE	Department of Energy
EBSFT	Engineered Barrier System Field Tests
EMAS	Engineering Measurement Analyses Section
ESF	Exploratory Studies Facilities
GTUF	G-Tunnel Underground Facility
HFEM	high frequency electromagnetic
ID	inside diameter
LLNL	Lawrence Livermore National Laboratory
NTS	Nevada Test Site
OD	outside diameter
PC	personal computer
PEBSFT	Prototype Engineered Barrier System Field Tests
QA	quality assurance
RTD	resistance thermometer device
SCFM	standard cubic feet per minute
SIRT	simultaneous iterative reconstruction technique
SLM	standard liters per minute
TCP	thermocouple psychrometer
TD	total depth
TOUGH	transport of unsaturated groundwater and heat simulator
WP	water potential
YMP	Yucca Mountain Project

Executive Summary

This final report presents a summary of data and interpretations obtained from the Prototype Engineered Barrier System Field Test (PEBSFT) performed in G-Tunnel within the Nevada Test Site. The PEBSFT was conducted to evaluate the applicability of measurement techniques, numerical models, and procedures developed for future field tests that will be conducted in the Exploratory Studies Facilities (ESF) at Yucca Mountain. The primary objective of the test was to provide a basis for determining whether tests planned for the ESF have the potential to be successful. This final report is supplemented by a progress report (Ramirez and Wilder, Eds., 1989). Also, the data and interpretations discussed in the progress and final reports are described in more detail in individual reports identified in the Bibliography at the end of this document. The introduction discusses the expected evolution of hydrothermal behavior during the prototype test, the expected hydrologic environment, the test concept, the borehole configuration, and the parameters that were measured during the test.

Chapter 1 on high frequency electromagnetic tomography discusses the rock mass electromagnetic permittivity and attenuation rate changes that were measured to characterize the water distribution in the near field of a simulated waste container. The data are used to obtain quantitative estimates of how the moisture content in the rock mass changes during heating and to infer properties of the spatial variability of water distribution, leading to conclusions about the role of fractures in the system.

Chapter 2 discusses the changes in rock moisture content detected by the neutron logging probe. The neutron data for the rock directly above the heater first shows that the rock increases its moisture content as steam generated closer to the heater condenses in cooler adjacent areas. This "halo" of increased moisture moves away from the heater as temperatures increase. Change in moisture content plotted as a function of radial distance show that the changes are not always radially symmetric relative to the heater borehole axis. There are significant differences in drying and rewetting behavior above and below the heater. The boiling zone acts as an "umbrella," which shields the rock below the heater from water draining vertically downward. Conceptual models to account for the differences in behavior are discussed.

Chapter 3 on permeability tests discusses the characterization of the in-situ permeability of the fractured tuff around the borehole. The air permeability testing apparatus, the testing procedures, and the data analysis are presented. Results show that higher permeabilities correlate spatially with mapped fractures. Also, the heating and cooling cycle resulted in detectable increases in bulk permeability along the borehole, and several possible mechanisms are suggested. Recommendations are made for future tests.

Chapter 4 describes the moisture collection system installed in the heater borehole to trap and measure the moisture volumes. The peak moisture collection rate was significantly less than that predicted by scoping calculations, and two possible reasons are suggested.

Chapter 5 describes relative humidity measurements made with the thermocouple psychrometer and capacitance sensors. A discussion of how relative humidity measurements relate to water potential is presented, along with a discussion of the individual thermocouple psychrometer calibrations. The locations of the thermocouple psychrometers and the results from those readings are presented. Recommendations are made for future tests.

Chapter 6 discusses gas pressure measurements in the G-Tunnel, addressing the calibration and installation of piezoresistive-gaged transducers. Results show pressure variations during the

heating phase and the heater ramp-down period. Some aspects of the pressure history can be explained by the thermal expansion of gas in the pores of an intact rock mass.

Chapter 7 describes the calibration and installation of thermocouples for temperature measurements. Results show a temperature difference on the heater container, which is probably an intrinsic characteristic of the heater container, not caused by the surrounding rock mass. Results also show that temperature readings of the traveling thermocouple agree very well with those measured by the stationary thermocouples. Comparisons of results with a conduction model and predictions of the V-TOUGH code (Buscheck and Nitao, 1991) show very good agreement, indicating that conduction was the dominant heat transfer mechanism and that transport of water, vapor, air, and heat in fractured media only caused secondary perturbations on the temperature. Several ways in which fractures can affect temperature are discussed, as well as different boiling processes. Some recommendations for future tests are presented.

Chapter 8 discusses the results of the PEBSFT, interpretations of these results, and plans for future tests. Results confirmed many elements of the pretest conceptual model of hydrothermal behavior as described in the Introduction. Also, results that are considered surprising in terms of environmental conditions are presented. There is also a discussion of the instrumentation performance with respect to measurement techniques and hardware.

Introduction

Abelardo L. Ramirez

The Prototype Engineered Barrier System Field Tests (PEBSFT) were performed in G-Tunnel, which is located within the Nevada Test Site (NTS). The G-Tunnel is physically remote from Yucca Mountain and is in the Grouse Canyon tuff rather than the Topopah Springs tuff; however, welded tuffs with properties believed to be similar to tuffs in Yucca Mountain are located in a portion of G-Tunnel (Zimmerman and Finley, 1986). Prototype testing was initiated so that when the Engineered Barrier System Field Test (EBSFT) is performed, the techniques, instrumentation, models, and procedures will provide the information needed to characterize the waste package environment. The three general objectives for the prototype testing were:

1. Investigate the physical processes that should be incorporated into numerical models describing hydrologic and geochemical processes in fractured, porous, densely welded tuff.

2. Evaluate the effectiveness of various measurement techniques and instrumentation for monitoring the hydrologic and thermomechanical response under realistic conditions.

3. Develop quality assurance procedures and evaluate their effectiveness for the investigations that will be performed at Yucca Mountain.

The prototype test was designed to duplicate, to the extent possible, anticipated test conditions for EBSFT at Yucca Mountain; for this, the reader is referred to a paper by Yow (1985), in which the general concepts of a waste package environment test are described.

Although the concept for these tests has evolved with time, the overall concept of what we will be measuring and why remains largely as described by Yow. Early planning recognized that significant environmental differences might exist between horizontal and vertical emplacement holes. Because of budget limitations and the desire to get started, only hydrologic aspects were included in the first prototype test; geomechanical and geochemical aspects will be studied during the second, more complete prototype test. Since vertical emplacement is the reference case for the Yucca Mountain Project (YMP), the prototype testing of the vertical orientation will be conducted in the second, more complete prototype test. The horizontal orientation was constructed first and is the subject of this report.

Scope of this Report

A progress report presenting the interpretation of data obtained from the PEBSFT from start-up to November 1, 1988 was previously published (Ramirez and Wilder, Eds., 1989). In addition to initial interpretations of data, results of scoping calculations performed before the test, and descriptions of the data acquisition system, the progress report contained information on the performance strategy, the environmental conditions of concern, and the design strategy for the waste package. Rock mass temperatures expected during the period extending from 100 to 1000 years and the period after 1000 years were discussed; the reader is advised to refer to the progress report to obtain information on all these subjects. The concepts and data presented in the progress report and in this final report as well as other information related to the PEBSFT

have been discussed in more detail in a number of publications, which are listed in the Bibliography of this report.

Anticipated Hydrologic Environment

The near-field hydrothermal response to thermal loading is shown schematically in Fig. 1. This concept is supported by the experimental work of Daily and others (1986) as well as the numerical modeling of Buscheck and Nitao (1988), Nitao (1988), and Buscheck and Nitao (1989). The primary mechanisms of heat and fluid flow are depicted for an idealized example of a horizontal heater which is intersected by a near vertical fracture. The actual heater borehole was intersected by more than a dozen fractures. The rock mass consists of matrix blocks that are bounded by fractures and the borehole wall (for blocks immediately adjacent to the heater). Under ambient conditions, the matrix blocks are partially saturated and the fractures and borehole are essentially dry. The heater heats the borehole surface primarily via thermal radiation. As heat is conducted through the fractured rock mass, vaporization begins in matrix blocks closest to the borehole. Vaporization proceeds from outer surfaces of each matrix block in toward its center. Where temperatures exceed boiling point (including effects of pressure, elevation, and capillarity), vigorous boiling occurs. In order for water vapor to flow out of the matrix blocks, gas-phase pressures must increase from matrix block surfaces to their interiors, resulting in the elevation of the boiling temperature with distance into the matrix block. Water vapor that enters the fractures is subsequently driven by gas pressure gradients (including buoyancy effects) within the fracture network. In general, vapor flow in the fractures is directed away from the center of boiling, either radially outward or inward towards the heater hole. Vapor flow in the fractures will persist until condensation conditions are encountered. Condensed water in the fractures that is not immediately imbibed by the matrix flows under gravity and capillary forces in the fractures either (1) back toward the boiling zone where it reboils or (2) out of the condensation zone where it eventually is completely imbibed by the matrix. The width of the condensation zone is partly dependent on the mobility of the liquid within the fracture. Liquid mobility in the fracture is affected by the ratio of the volumetric liquid flux of water in the fracture divided by the product of the unsaturated porosity and the imbibition diffusivity of the matrix (Nitao and Buscheck, 1989b).

Test Concept and Borehole Configuration

An underground facility called the G-Tunnel Underground Facility (GTUF) has been constructed by the Sandia National Laboratories for the Yucca Mountain Project (YMP). The GTUF consists of drifts in the configuration as shown in Fig. 2. The prototype test was conducted in the Small Diameter Heater Alcove and the Rock Mechanics drifts. The prototype test effort included scoping calculations, laboratory tests, and field testing efforts in GTUF. The test measured several parameters as a function of location and time in the near field (within a few meters) of a heater emplaced in welded tuff. The test included an accelerated thermal cycle to examine the effects of the heating and cooling phases of a thermal load.

Figure 3 shows the planned thermal loading history for the test. The initial thermal loading for the 3-m (9.8-ft) heater was approximately 3.3 kW (1.1 kW/m). This initial loading was higher than the loading expected for the spent fuel canister (0.4–0.7 kW/m) in an attempt to increase the volume of rock disturbed in the relatively short period available for prototype testing and to create sufficiently high rock temperatures to result in boiling conditions. The duration of heating was chosen so that the boiling point isotherm would extend approximately 0.6–0.7 m (2.0–2.3 ft) from the heater borehole wall. This provided a sufficiently large volume to include several fractures.

This prototype test consisted of four measurement phases:

1. The ambient temperature phase consisted of the measurement of baseline conditions prior to heating.

2. The heating phase consisted of heating the rock according to the flat portion of planned power loading history shown in Fig. 3. The measured power loading history is shown in Fig. 7-1 of this report. This phase began when the heater was energized on September 7, 1988 at approximately 11:30 a.m. The duration of this phase was based on the extent of the boiling region as defined by temperature measurements.

3. The cool down phase started after approximately 4 months of heating at full power. This phase involved a stepped heater-ramp-down period lasting about 10 weeks. Of particular interest were the measurements obtained when the rock mass temperatures began to drop below the boiling point of water.

4. The post-thermal stage involved monitoring the rock mass for 3–4 months after the heater was de-energized.

Figures 4 through 9 show the borehole layout and the measurement stations for the various instruments used. The test location within G-Tunnel was bounded by the Small Diameter Heater Alcove and the Rock Mechanics Incline, as shown in Fig. 2.

The heater borehole was inclined slightly upward (elevation increases from the collar to the end of the borehole) from the Rock Mechanics Incline, as shown in Fig. 6. The diameter of the heater borehole was 12 in. (30.5 cm).

The remaining 12 boreholes were used to monitor the rock response; all of these were inclined downward (collar elevation is greater than bottom elevation). The majority of the boreholes were orthogonal to the heater hole axis, which provided better coverage of the variations in response that occurred radially outward from the heater. This arrangement allowed measurements in the direction of expected maximum thermal and hydrologic gradients. Three boreholes were drilled parallel to the heater borehole axis to monitor rock response beyond the ends of the heater.

All boreholes, with the exception of the heater borehole, were sealed with grout to prevent them from being flow paths to gas or liquid phase water. The grout consisted of a portland cement–sand–water mixture. It was installed in two stages. First, a very viscous grout was delivered to the borehole and allowed to cure for a few days; this mix was used to seal possible flow paths for the more fluid grout mix installed later. Second, the grout column was reamed out (leaving behind that grout which had penetrated the fractures to some degree). Third, the instrumentation packages or the borehole liners were inserted in the boreholes. Fourth, a more fluid (than the original) grout mix was installed in each borehole to facilitate the flow of grout around the instrument packages and borehole liners.

Boreholes NE3, NE4, and NE5 were the first boreholes to be drilled. A diameter of 2.4 in. (6.1 cm) was chosen to minimize the volume of grout to be sampled by the geophysical logging probes. The diameter for the remaining boreholes (NE1, NE2, NE6, NE7, P1, P2, P3, TC1, and TC2) was increased to 3.0 in. (7.6 cm) to alleviate the concerns that the grout would not fill all of the smaller annular space (these concerns were proved later to be unfounded). There was also evidence showing that the 2.4–in. boreholes deviated from the planned alignment more than expected. Boreholes P1, P2, P3, TC1, and TC2 were backfilled with grout with their corresponding instrumentation packages in place. Boreholes NE1 to NE7 were completed with a

grout/liner system which allowed access for the geophysical probes. The liner materials consisted of Teflon (where temperatures >100°C were expected) and polycarbonate (where temperatures <100°C were expected). The diameter of the liners in boreholes NE1, NE2, NE6, and NE7 was 2.0 in. O.D. (5.1 cm) and 1.75 in. I.D. (4.45 cm). The liner diameters in boreholes NE3, NE4, and NE5 were 1.75 in. O.D. (4.45 cm) and 1.63 in. I.D. (4.13 cm).

Boreholes P1, P2, and P3 contained thermocouple psychrometers and one microwave resonator to measure air humidity in the borehole. Boreholes TC1 and TC2 contained thermocouples to measure rock mass temperature. The remaining boreholes (NE1, NE2, NE3, NE4, NE5, NE6, and NE7) were used for electromagnetic and neutron probe measurements to monitor changes in moisture content. These measurements were, on occasion, supplemented by gamma–gamma density surveys to detect the slight variations in bulk density caused by changes in moisture content.

Measured Parameters

The following parameters were measured during the test. The way in which each parameter was used to infer rock mass behavior and the time interval between measurements are described.

- Temperatures were used to reconstruct the thermal response of the rock and to evaluate the performance of measurement equipment emplaced in hot regions of the rock mass. Temperatures were measured automatically every 60 minutes.

- Rock mass gas pressures and barometric pressure were needed to understand the flow of the gaseous phases in the rock mass. Both types of measurements were automatically recorded every 60 minutes.

- Air humidity measurements in the rock mass around the heater were used to determine the pressure of the liquid phase in the rock matrix. This measurement was recorded automatically every 30 minutes. (This was the standard setting for this system). Air humidity within the heater borehole was used to monitor the changes in relative humidity of the vapor/air mixture. This measurement was automatically recorded every 60 minutes.

- Cross-hole measurements of the relative dielectric constant of the rock and single-borehole measurements of thermal neutron counts and gamma ray counts were used to infer the spatial and temporal changes in the moisture content of the rock mass. These measurements were repeated every two weeks (approximately). The inferred moisture content information was used to reconstruct the distribution of liquid water in the rock mass as a function of space and time.

- Air permeability measurements performed within the heater borehole before and after heating of the rock were used to detect any permeability changes caused by the heating cycle.

- Heater wattage was recorded hourly to document the thermal loading history.

- Time was used as a reference for all measurements.

- Fracture locations and orientations were measured by borescope and/or borehole television surveys performed in all the boreholes before the heater was

energized and along the emplacement borehole after test completion. This information was needed to understand the effects of heating on the stability of the emplacement borehole walls and to understand the changes in fracture permeability caused by the heating and cooling cycles. This information also aided in the interpretation of the flow regime of vapor and liquid water in the rock mass.

- The volume of water vapor invading the heater borehole was measured to obtain estimates of how much vapor flows toward the heater borehole. This information was recorded automatically every hour.

A description of the data acquisition system and of the recording and archiving procedures can be found in Watwood and Beatty (1989).

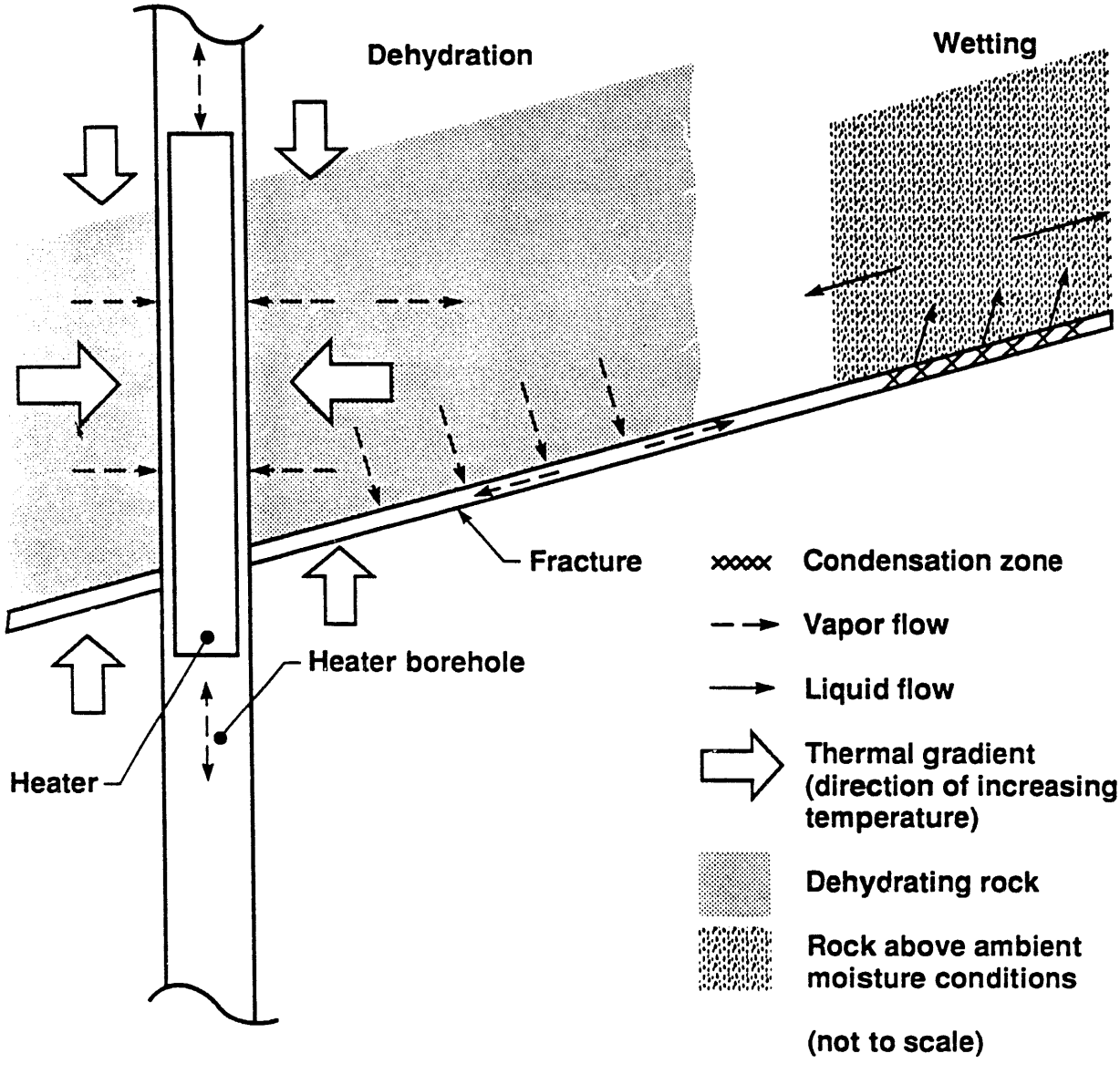

Figure 1. Schematic representation of a possible hydrologic scenario in partially saturated, welded tuff subjected to a thermal load. Orientation shown is side view of a heater placed horizontally.

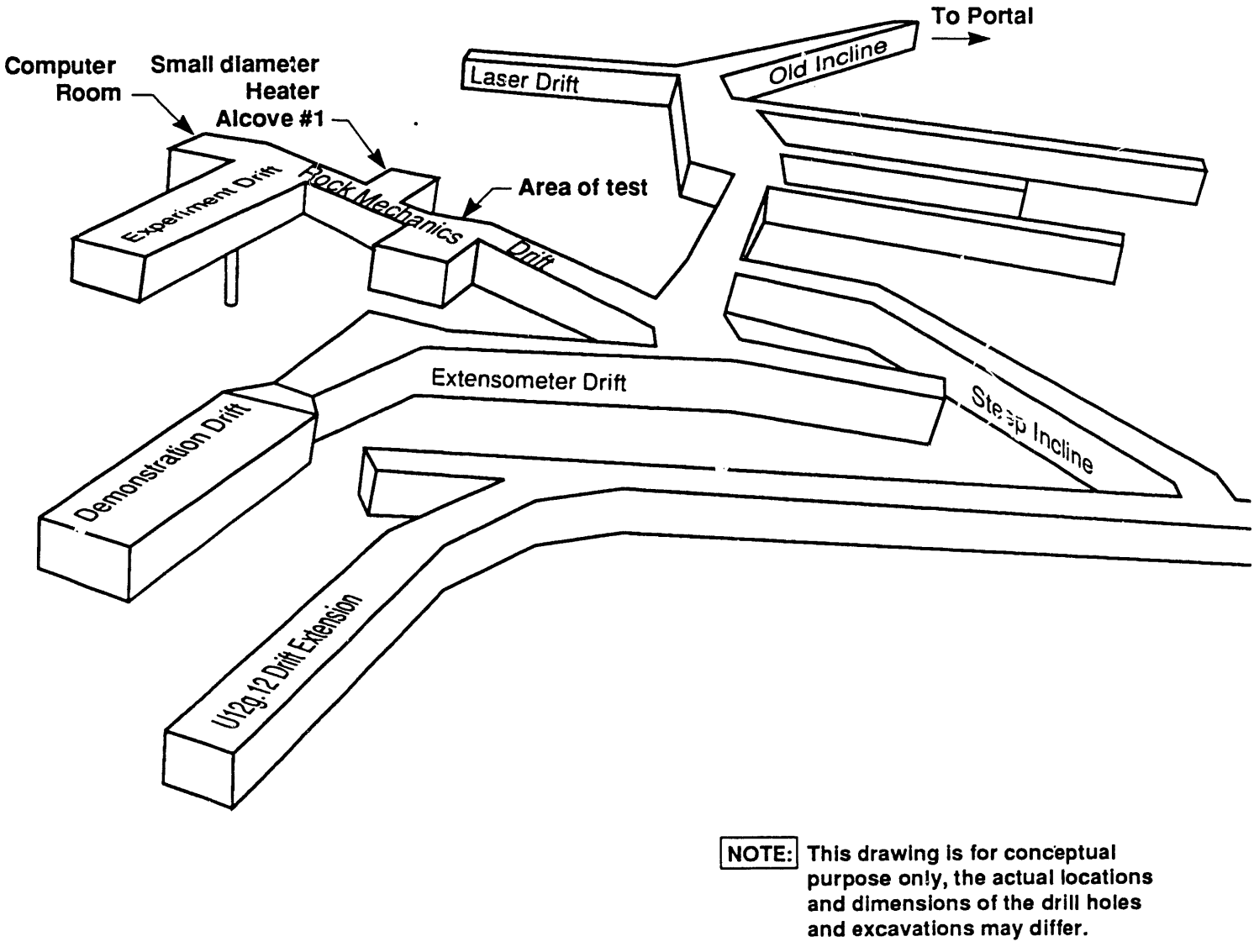

Figure 2. G-Tunnel Underground Facility and locations for the prototype test. The test region is bounded by the Small Diameter Heater Alcove and the Rock Mechanics Incline.

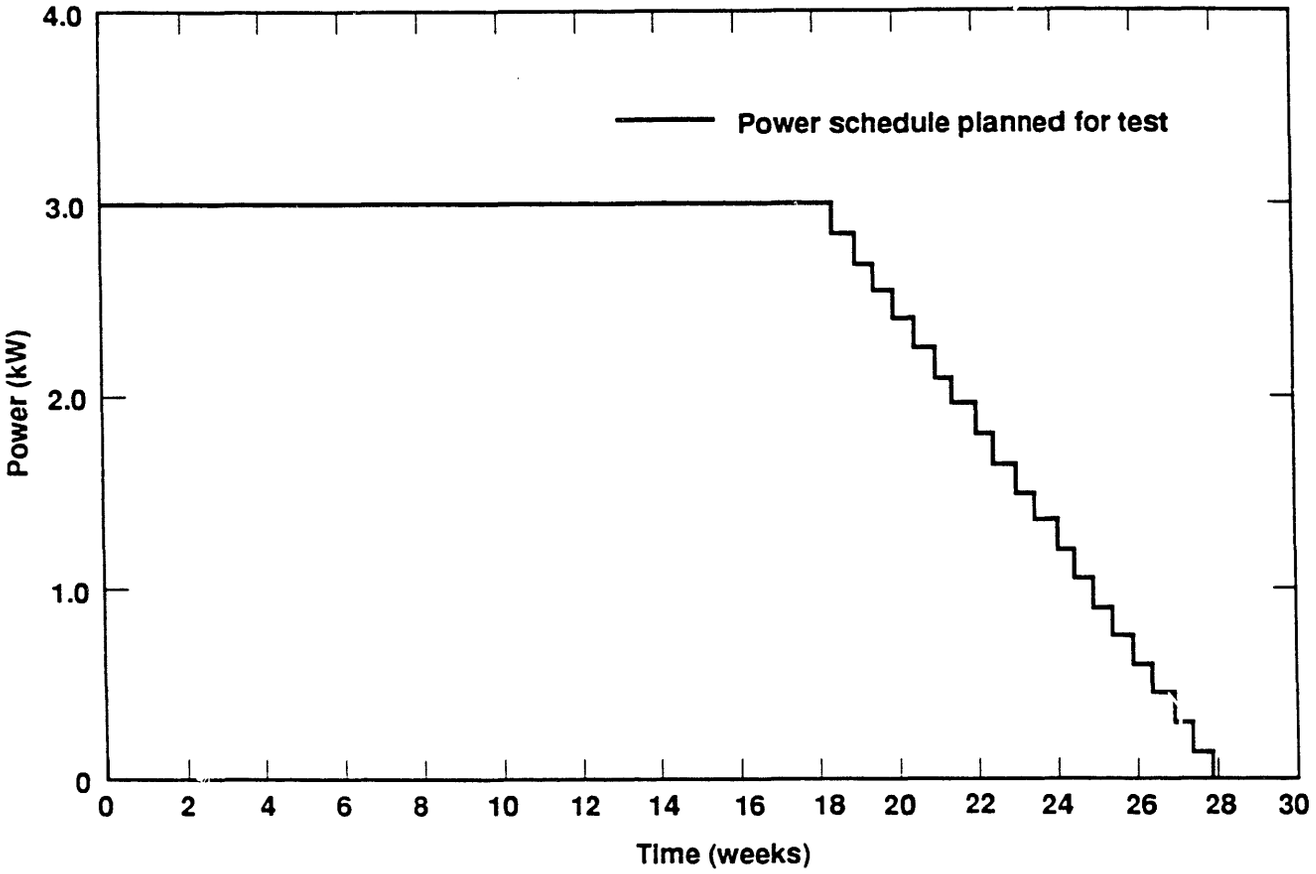

Figure 3. Planned power loading history for the test. The actual measured power levels are shown in Fig. 7-1 of this report.

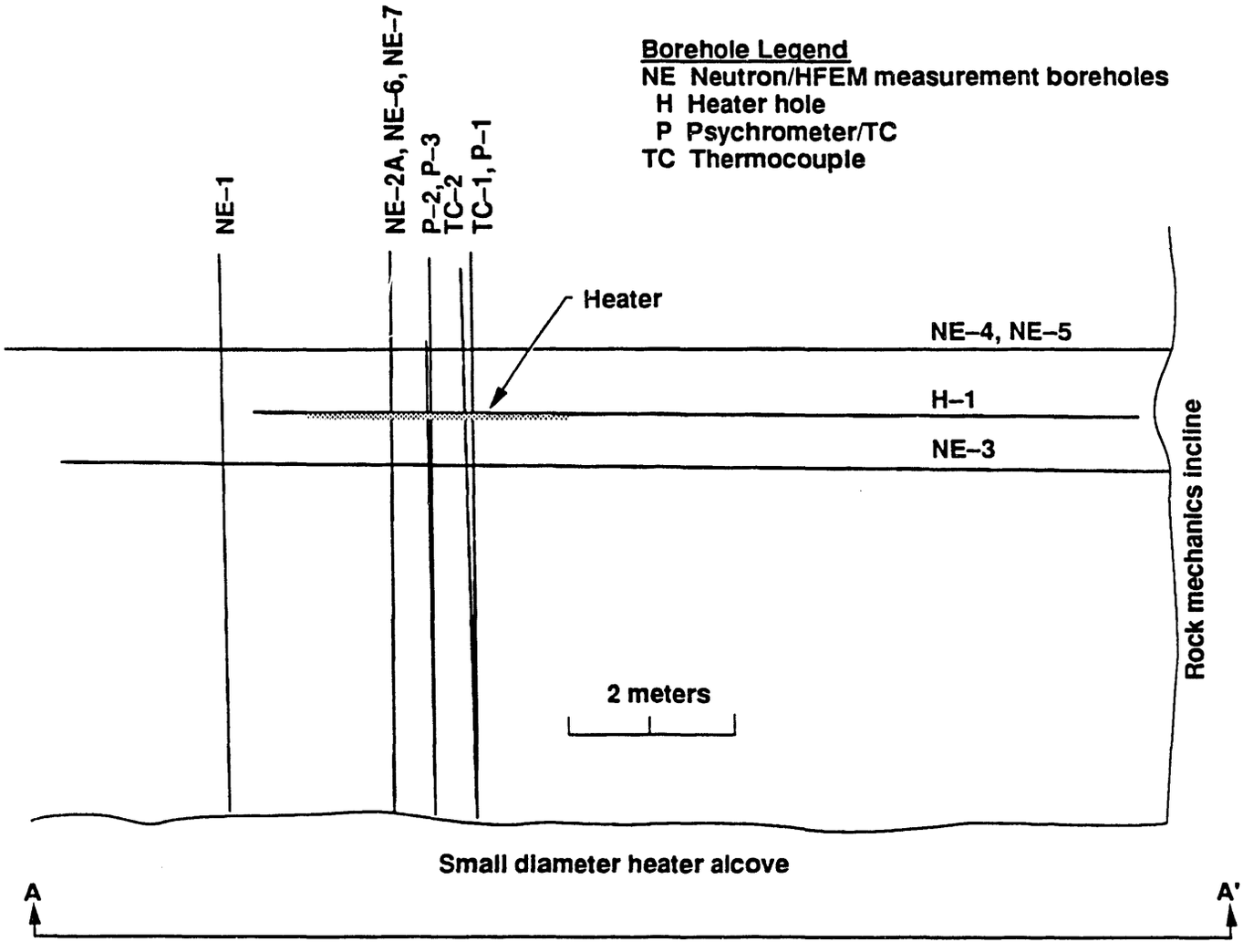

Figure 4. Plan view of the as-built borehole layout. The location of the Rock Mechanics Incline and the Small Diameter Heater Alcove in G-Tunnel are shown for reference.

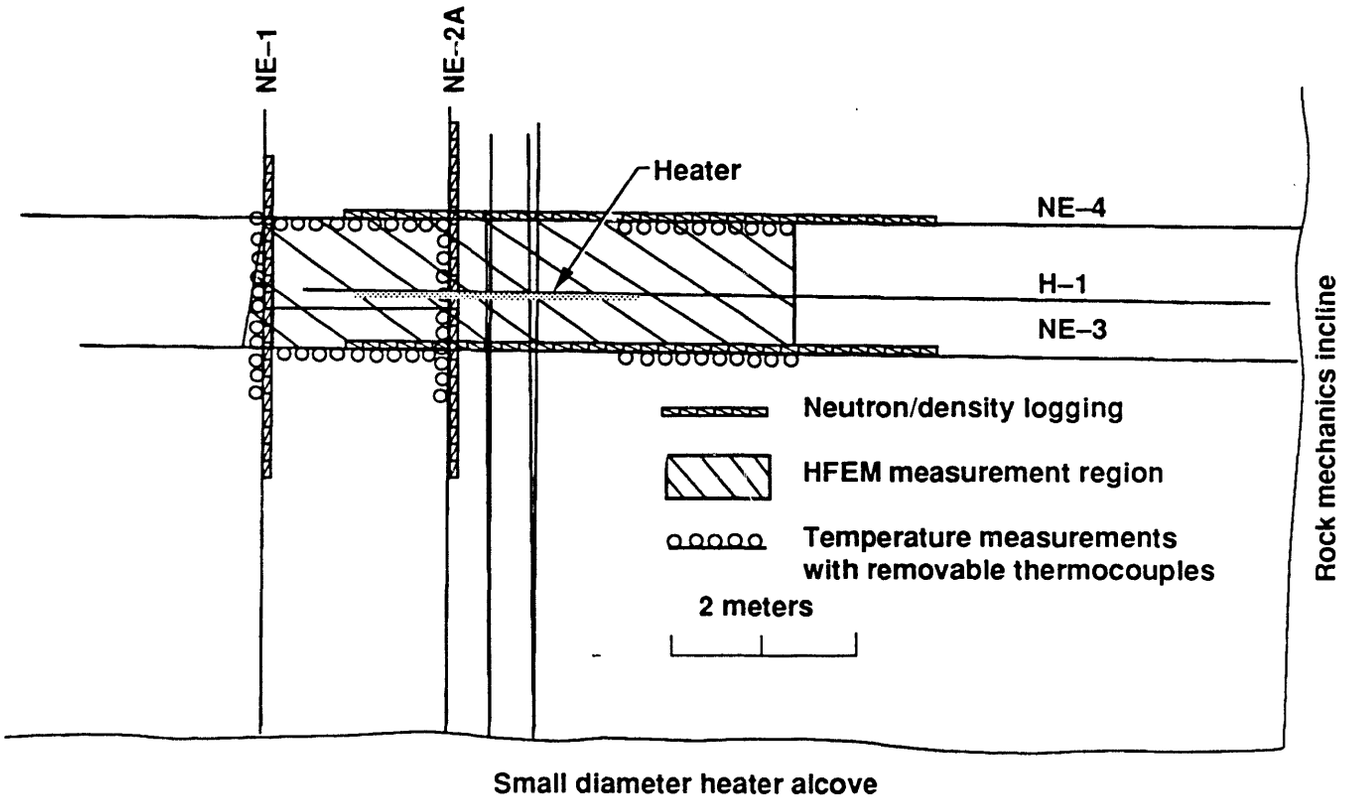

Figure 5. Plan view of the as-built borehole layout. Also shown are the measurement stations and cross-hole measurement planes used for geophysical surveys during the test.

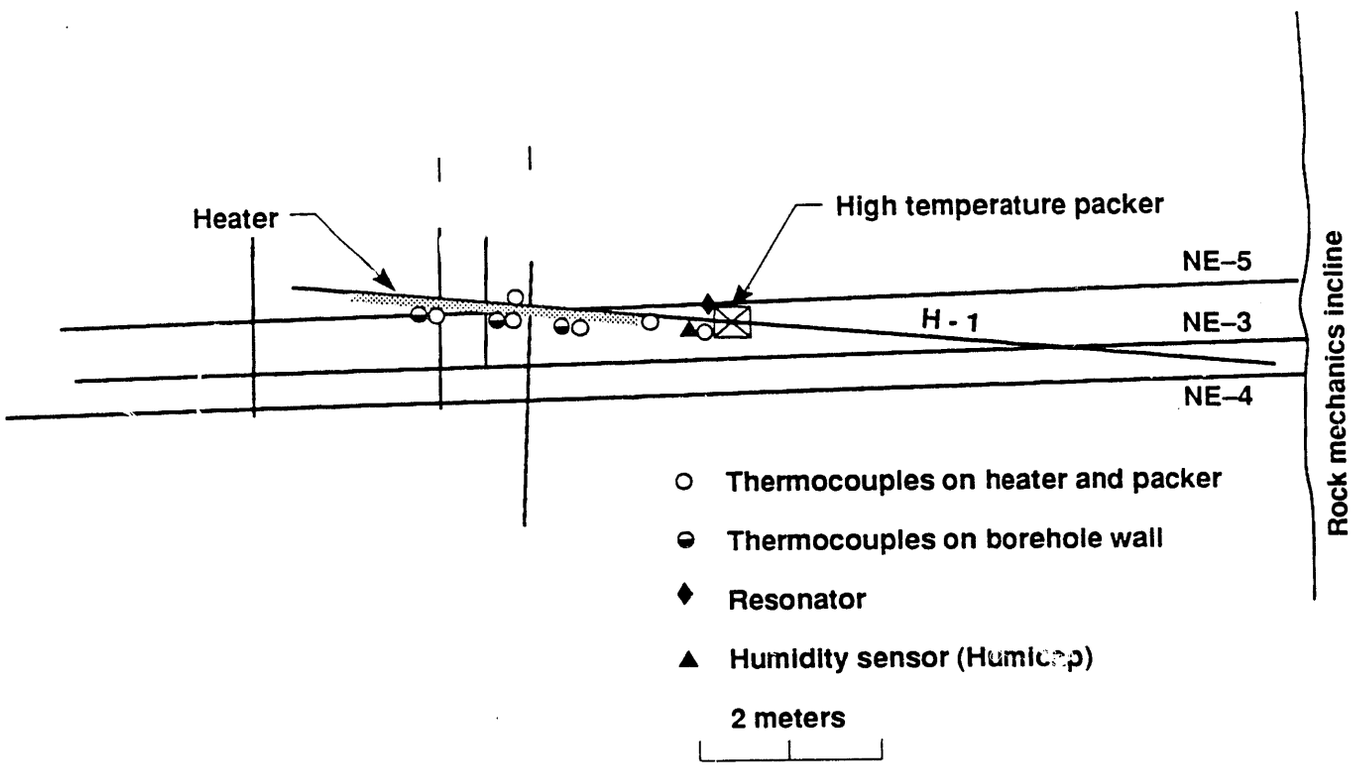

Figure 6. Side view of the as-built borehole layout as observed from the Small Diameter Heater Alcove. Also shown are the measurement sensors installed within the heater borehole.

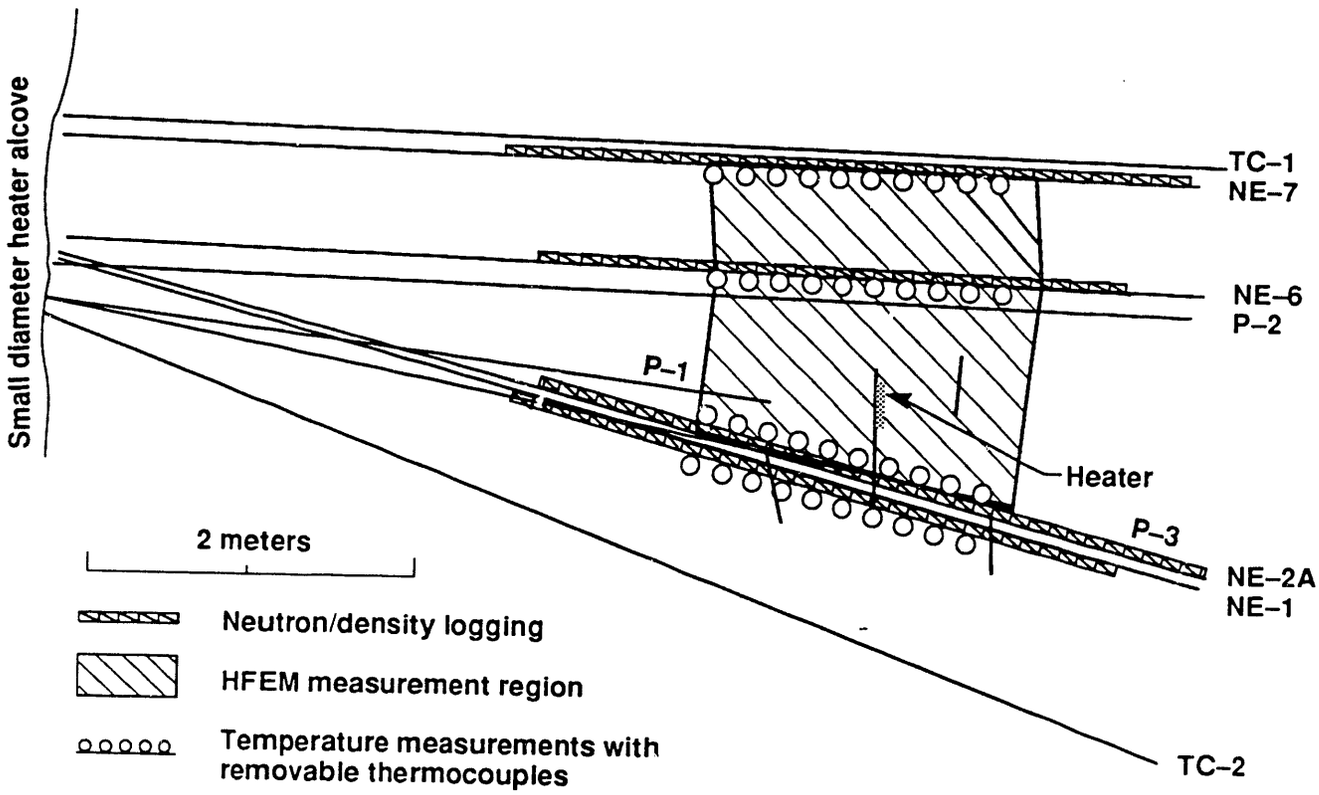

Figure 7. Side view of the as-built borehole layout as observed from the Rock Mechanics Incline. Also shown are the measurement stations and cross-hole measurement planes used for geophysical surveys during the test.

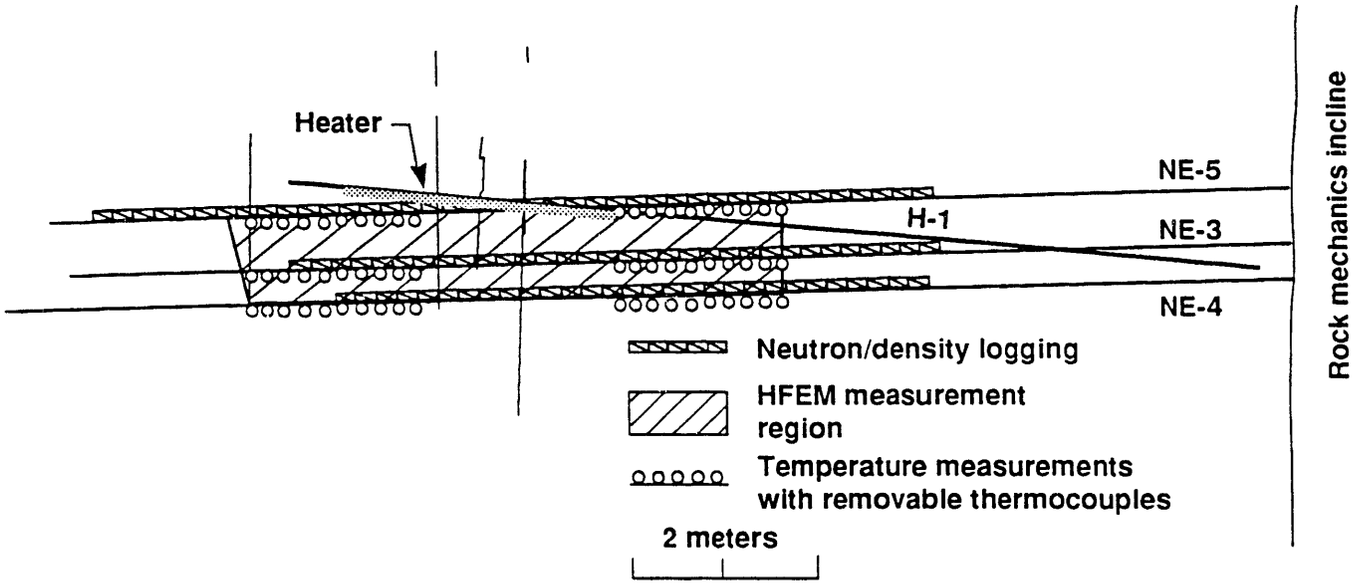

Figure 8. Side view of the as-built borehole layout as observed from the Small Diameter Heater Alcove. Also shown are the measurement locations and cross-hole measurement planes used for geophysical surveys during the test.

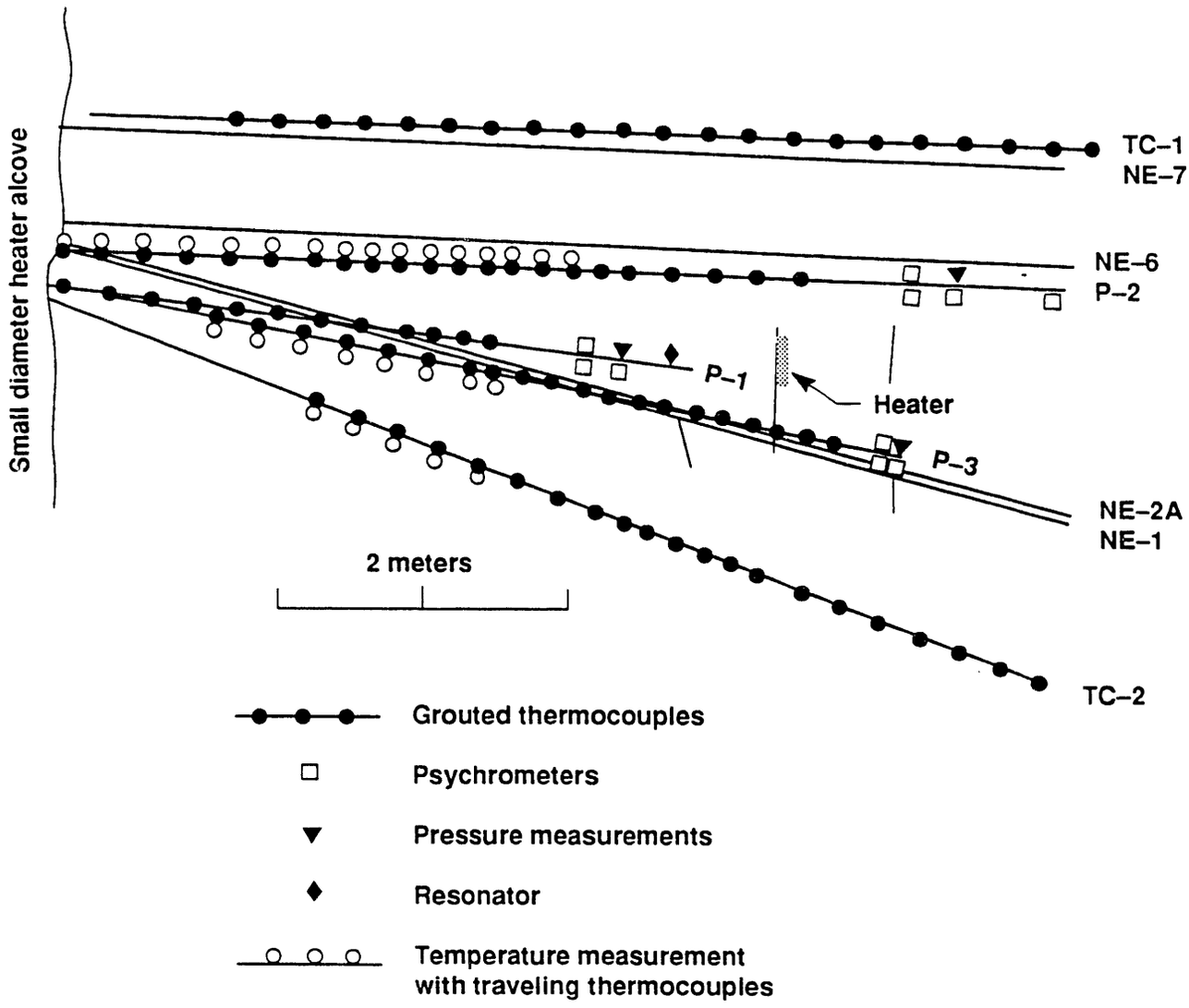

Figure 9. Side view of the as-built borehole layout as observed from the Rock Mechanics Incline. Also shown are the locations of various sensors grouted in various boreholes.

Chapter 1

High Frequency Electromagnetic Tomography to Infer Hydrology in Heated Welded Tuff

William Daily and Abelardo Ramirez

High frequency electromagnetic tomography is one technique that can be used to remotely characterize hydrology near the heater (Ramirez and Daily, 1987). By cross-hole transmission of 200-MHz electromagnetic signals and tomographic reconstruction of these data, we mapped the electromagnetic permittivity and attenuation rate of the rock mass in the plane between the boreholes and infer changes in rock moisture content from these data. Additional details of this work can be found in Daily et al. (1990).

Experimental Procedure

Seven boreholes were available for high frequency electromagnetic (HFEM) measurements (see the borehole layout described in the Introduction). These same holes were also used for neutron logging. Six regions were chosen to be tomographically imaged using these boreholes. The regions were chosen to define flow paths and the dehydration that takes place at the elevated temperatures around the heater.

All measurements were made using an automatic network analyzer, controlled by a computer (Fig. 1-1). Electrically short (physical length less than one wavelength), sleeve dipole antennae were used for transmitting and receiving. At each antenna position, the signal amplitude was measured at 200 MHz (CW) and the phase change was measured as the frequency was swept from 190 to 210 MHz. Using

$$r \frac{\varepsilon^{1/2}}{\varepsilon_o^{1/2}} = c \, \Delta\psi/\Delta\omega \qquad (1\text{-}1)$$

where $\Delta\psi$ = the measured phase change,

$\Delta\omega$ = the angular frequency change (20 MHz),

r = the known ray path length,

ε = the electromagnetic permittivity of the rock, $\varepsilon_r = \varepsilon/\varepsilon_o$

ε_o = the electromagnetic permittivity of free space, and

c = the speed of light,

we can obtain the line integral permittivity, $r\,\varepsilon^{1/2}$, along each straight ray (Dines and Lytle, 1979). Equation (1-1) is valid for a homogeneous medium in the far field (about one wavelength in the medium) of the transmitting antenna.

Data Analysis

Image reconstruction is by an algorithm developed by Dines and Lytle (1979). The region in the plane between the boreholes is represented by the material parameter such as velocity $v(x,y)$ or attenuation rate $\alpha(x,y)$, which is to be calculated iteratively by fitting collected data to the model generated results. Iterative methods, especially suitable for computer solutions, have been devised that work well on under determined and inconsistent data. We have used the simultaneous iterative reconstruction technique (SIRT).

Data Interpretation

The tomographs generated in this work are of electromagnetic permittivity of the rock mass. Of course, images of this parameter by itself are of little help in determining the near-field environment of the heater canister. To be useful, the data must be interpretable in terms of water content in the rock, because this property is indicative of its hydrological behavior.

A quantitative interpretation requires laboratory calibration of the electromagnetic properties of densely welded tuff, that is, measurement of the dielectric properties as a function of water content and temperature. This calibration allows inference of in situ water content from tomographic dielectric properties. Figure 1-2 shows preliminary results from one sample measured at room temperature with water from Well J-13 at Yucca Mountain, Nevada as the pore fluid. These data were acquired using an automatic network analyzer to measure the transmission and reflection coefficients of a tuff sample machined to fit in an air line, and from these the sample permittivity was calculated (Freeman et al., 1979). These data show a nearly linear, monotonically increasing relation between water content and dielectric permittivity at 200 MHz. Because we can only measure changes in electromagnetic properties, the slope of the model calculation which fit the data will be used to infer changes in rock mass water content. This slope implies a 3.4 vol% change in water content per unit change in relative permittivity.

This interpretation is valid only when the porosity is constant. This was the case with the data in Figure 1-2 from a single sample and it is also the case comparing the same region of two tomographs of a rock mass taken at two times. Because the porosity is constant, changes in permittivity can only be attributed to changes in moisture content (or changes in temperature, which can be shown to be a small effect compared to those expected from moisture content changes). Two different rocks with the same moisture content but different porosity will have different electromagnetic permittivity since there is a different content of void (permittivity unity) in them. This means that there may be an error comparing two different parts of a permittivity tomograph to infer differences in moisture content in those parts of the rock mass. However, since the relative permittivity of the silicate matrix is only about 4 and that of water is about 81, only relatively small differences in permittivity can be accounted for by variations in porosity. The only reasonable explanation for the larger permittivity differences in two portions of the rock is differences in moisture content. For example, if the porosity at two points in the rock is 11 and 15% (values typical of samples measured from the test region) but the moisture content is the same, the relative permittivity for those regions would be 10.1 and 10.0, respectively. On the other hand, if the moisture content at the two points in the rock is 11 and 15% by volume (again, typical values) but the porosity is the same, the relative permittivity for those regions would be 11.0 and 13.3, respectively. For this reason, in the interpretation of the data below we assume that the spatial variations in permittivity are due entirely to variations in moisture. We assume that the approximation of constant porosity introduces only a small error using this interpretation.

To obtain the variability in the images due to repeatability errors in the measurement system we compared images from data sets taken at different times but over an interval when changes in the rock mass are expected to be minimal. This procedure shows that for the central part of the image plane $\varepsilon_r^{1/2}$ varies by about ±0.04 (Daily and Ramirez, 1989).

Results and Discussion

Ray Data

The data shown in Fig. 1-3 are the measured relative permittivity along rays for which the transmitter and receiver were at common depths in their respective boreholes. Each point is a measure of the right-hand side of Eq. (1-1), divided by the ray path length. For example, the points at 11.0-m depth represents the average permittivity (at various times) for the rock along a line that connects the transmitter and receiver at 11.0-m depth. We present this data first because they are the input to the reconstruction algorithm. In this format, the spatial information generated by the reconstruction is absent, but the artifacts generated by the reconstruction are also absent so that quantitative interpretation of the results should be more reliable.

Figure 1-3 shows an example of these data between NE4 and NE5. This plane is parallel to the heater, 0.75 m to one side and below the heater in elevation. Between August 26, 1988 and March 29, 1989, the relative permittivity ε_r decreased from approximately 11.5 to 8.4 (changes in $\varepsilon_r^{1/2}$ of about 0.5). Of course the rock mass is not homogeneous; therefore, this is a rough average over the region. If the rock mass were at 20°C during the period, this variation in relative permittivity of 3.1 would represent a change in fractional water content of about 0.11 (from the lab data in Fig. 1-2, 3.1+29). If we assume the rock mass was always at 100°C, the calculated water content change would be 0.15 (3.1+21). The actual change in water content is likely between these values. The average effective porosity of several samples from the test region was determined to be 0.128 ±0.023; therefore, either figure represents a substantial drying of the rock mass at a distance of more than 1 m from the end of the heater.

To account for the temperature effect mentioned above in image interpretation, we would need the temperature distribution in the image plane. Since this information is not available, we will use the room temperature calibration data in Fig. 1-2. This will not result in significant interpretation errors since the slope of the solid and dashed curves in Fig. 1-2 are nearly the same, which means that corrections for this temperature effect would be less than the measurement precision inherent in the relative permittivity.

The dehydration measured between NE4 and NE5 appears not to be monotonic. The initial permittivity decrease was followed by an increase recorded on September 26, which might correspond to a saturation halo preceding the drying front. If so, the data indicate an increase in fractional moisture content up to 3% over initial conditions. The increase between January 19 and February 27 is of similar magnitude and both increases are of the order of the system calibration error and so that the significance of the data is uncertain.

Cross-borehole ray data between holes NE2A to NE6 and NE6 to NE7 indicate that before the experiment started there was a higher water content in the rock mass below the heater than above. These two data sets are from the highest and lowest elevations of the rock where HFEM measurements were made. Because of the proximity of the metallic heater to NE6, data from the full length of that hole cannot be used for reliable calculation of permittivity values. However, data at the extremes of the range measured show that above the heater (between NE6 and NE7) the typical relative permittivity is about 7.8 while below the heater (between NE2A and NE6) the permittivity is typically about 10.0 (remember that these absolute values

are not accurate because of uncertainties in system calibration but the relative magnitudes are reliable). If these data are representative of the rock mass adjacent to the experiment, the upper part of the rock might be dryer than that below (lower fractional water content of about 0.08). We have no way of knowing if this was a pristine condition. On the other hand, a possible external source of such a moisture gradient is the drill water used for the 11 boreholes. Drill water draining downward along fractures would tend to increase moisture content at the lower elevations more than at higher elevations. Based on these data air drilled holes should be considered for future testing.

Tomographs During Heating

During the 10-month experiment, data were acquired for more than 100 tomographs; each data set required collecting 441 individual data points. Figures 1-4(a) through (e) show examples of the tomographs taken before, during, and after the heating phase. Figures 1-4(a) through (d) are from the region between boreholes NE4 and NE5 in the interval 9.5 and 11.5-m depth. Unfortunately, the data used for these reconstructions were influenced by the proximity of this plane to the heater. However, comparing images with and without the heater in place, we have determined that between 10.5 and 11.5 m, the reconstructed permittivity is changed by less than ±0.15 by the proximity of the heater. Shallower than 10.5 m, the influence can be larger but varies depending on the location within the image. Deeper than 10.5 m, the reconstruction reflects more accurately the heterogeneity in the rock mass permittivity before heating began. For this part of the image plane, the variation in $\varepsilon_r^{1/2}$ introduced by measurement imprecision is ±0.04 [estimated by comparing two tomographs taken when no known changes were occurring in the rock mass (Daily and Ramirez, 1989)].

Figure 1-4(a) is the tomograph between NE4 and NE5 before heating. The range of imaged relative permittivity deeper than 10.5 m is from about 6.2 to 16.0. The (extrapolated) calibration data in Fig. 1-2 suggests that this represents a fractional moisture content contrast of about 0.34. This is a fairly large range and is possible for only two small regions, each represented by a single pixel (each 8 by 9 cm). A more representative range of permittivity is 9.0 to 12.2, which implies a contrast of 0.11 in fractional water content. This is close to the 0.128 ±0.023 average fractional porosity we measured for laboratory samples of this rock mass. The approximate correspondence in the in situ measured range of pre-heating moisture and the laboratory measured porosity implies that the rock mass saturation varied over most of its possible range, i.e., the rock was nearly saturated initially and nearly dry toward the end of heating.

In this same reconstruction, the region near NE4 at about 960-cm depth is imaged as a very low permittivity. Even though these data are contaminated by the presence of the heater, our tests indicate that this anomaly is indicative of a rock mass anomaly. This region is likely a highly fractured zone with apertures too large to retain a significant amount of water by capillarity. The preheating borehole logging identified a highly fractured zone exactly at this location in NE4. Typically, fracture orientation was measured in these logs. At this location, however, orientation could not be determined because of the high fracture density. An interesting speculation is that a particularly high porosity was created during drilling as a washout in an intensely broken zone. Except for this one region, there seems to be a poor correlation between logged fractures in either borehole and either high or low permittivity image anomalies.

Figure 1-4(b) is an image of the same region taken 19 days after the heater was energized. This alterant image is formed as a pixel-by-pixel difference with the base-line data [Fig. 1-4(a)], such that positive values of $\Delta\varepsilon_r^{1/2}$ reflect an increase in permittivity with respect to initial conditions. This represents a portion of the saturation halo seen in the ray data and described in the preceding section; it appears as a slight increase in permittivity over the image plane

and not a sharp, well-defined front. This increase of 0.2 in the square root of relative permittivity (seen best in Fig. 1-3) is indicative of about a 5% increase in moisture content.

The alterant image at the end of the heating phase is shown in Fig. 1-4(c). (The ramp-down in heater power started January 13, 1989.) This image is also a difference image relative to the base-line data [Fig. 1-4(a)], such that positive values of $\Delta\varepsilon_r^{1/2}$ reflect an increase in permittivity. Much of the imaged structure between 9.5 and 10.5 m was contaminated by the heater interference. However, the strong positive anomaly at 9.6 m, earlier identified with a broken zone in NE4, is probably real. This positive anomaly persists throughout the heating period. If real, it means that the fracture zone intersecting NE4 at this location is wetter than its preheating state throughout heating. At least two explanations are possible.

First, this might be a fracture zone that is draining condensate from the saturation halo above the heater to the rock mass below, where the water is lost to the system. Model calculations of Nitao and Buscheck (1989) indicate that, if the matrix porosity in this zone is sufficiently high (assuming the capillary tension data used in the model are appropriate), a significant flux of liquid water is unlikely in this fracture system. Liquid water might flow in the fractures if the fracture porosity is sufficiently large relative to the matrix porosity and if the capillary tension data used in the hydrothermal scoping calculation (Buscheck and Nitao, 1989; Nitao and Buscheck, 1989) are not representative of this rock.

The other explanation is that the additional water in this zone is from capillary condensation of moisture-laden vapor moving through the fractures. The source of this vapor could be water driven from the rock by heating or ambient vapor moved by buoyancy.

Deeper than 10.5 m, the image is more quantitatively reliable. As in the base-line image, there is no other correlation of image anomalies with borehole fractures. This means that these fractures are neither wetter (acting as a flow path for liquid water) nor dryer than the surrounding rock and perhaps contribute little to the hydrology of the system.

Figure 1-4(e) shows tomographs taken between holes NE3 and NE4 during full-power heating. The heater is directly over one end and about 1 m above this plane. Below the heater, there is no increase in water content during the heating phase. This is evidence that no condensation front is established directly below the heater, because any vapor moving through fractures and condensing at temperatures below the dew point can drain by gravity (imbibition is slow relative to the velocity of liquid water draining down the fracture) and be lost from the system. A small increase in saturation is seen off the end of the heater and appears to wrap around the end of the heater; in subsequent images, it moves further from the heater with time. This might be condensate forming above and running off the end of the zone of active boiling surrounding the heater.

Tomographs During Cool Down

Figure 1-4(d) shows an example of the tomographs between NE4 and NE5 taken 4 months after the heater power was turned off. By this time, temperatures in this region had declined from about 100°C to about 20°C. Notice that there are relatively small changes in rock mass permittivity relative to the heating phase [Fig. 1-4(c)]. In fact, the increases in relative permittivity are about equal to the measurement uncertainty. This is evidence that the rewetting rate of the rock mass during cool down is slow relative to the drying rate of the rock mass during heating. This conclusion is also true for the plane below the heater between NE3 and NE4 and is the main conclusion that can be reached from the data taken during cool down.

Summary

HFEM data was used to characterize the spatial and temporal changes of water distribution near field a heater placed in welded tuff. First, we used data from individual ray paths to determine quantitative estimates of how moisture content in the rock mass changes during heating. This interpretation is an average over the ray length between the boreholes and has little information on spatial variability. However, the results are semiquantitative; only with a valid calibration of the measurement system could the results be quantitatively reliable. With such a quantitative measurement, a determination of absolute water content of the rock mass might be possible. Second, we used the tomographs generated from the cross-borehole data to infer properties of the spatial variability of water distribution. This interpretation lead to conclusions about the role of fractures in the hydrologic behavior of the system.

The parallel scan data and the tomographs suggest that the rock immediately around the heater begins to dry soon after the heater is turned on. Rock further from the heater shows an early wetting episode probably caused by condensation of steam in cooler portions of the rock. Following this wetting, the rock begins to dry as temperatures and evaporation rate increase. Some fractures and highly fractured zones might remain wetter than preheating conditions long after the surrounding rock matrix has begun dehydration. Our data do not directly indicate whether this water is stationary or flowing. However, since other parts of the rock mass in these image planes are drying and these fractures are not, it is likely that these fractures are conduits for water movement during the heating process.

We learned two important lessons which should be considered for any future use of HFEM imaging for this work. First, a practical calibration of the HFEM system is important. This would allow a reliable measurement of absolute relative permittivity and this is an important requirement for determination of absolute moisture content. Such a calibration has recently been described by Daily et al. (1989). Second, interference from anomalies placed in the rock mass (especially the heater canister) must be minimized. This could be accomplished by model calculations and by careful in situ measurements guided by results from this test.

Acknowledgements

The authors are thankful for helpful discussions with J. Berryman, D. Wilder, and T. Buscheck. Also, J. Beatty, D. Watwood, and J. Carbino provided valuable technical support.

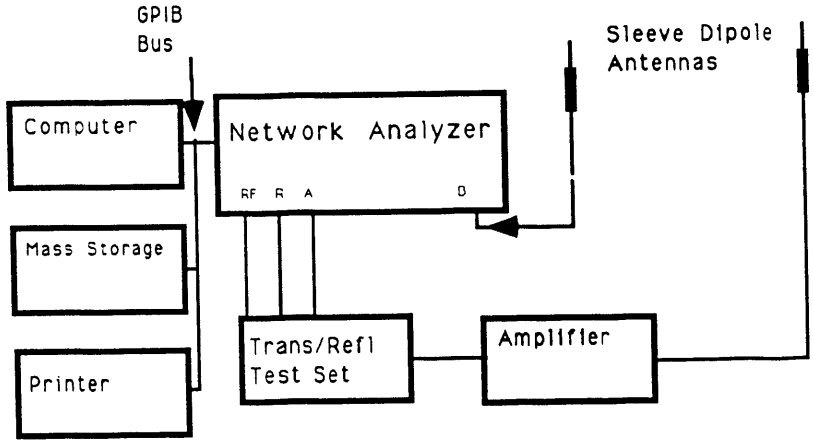

Figure 1-1. Block diagram of the high frequency electromagnetic (HFEM) system.

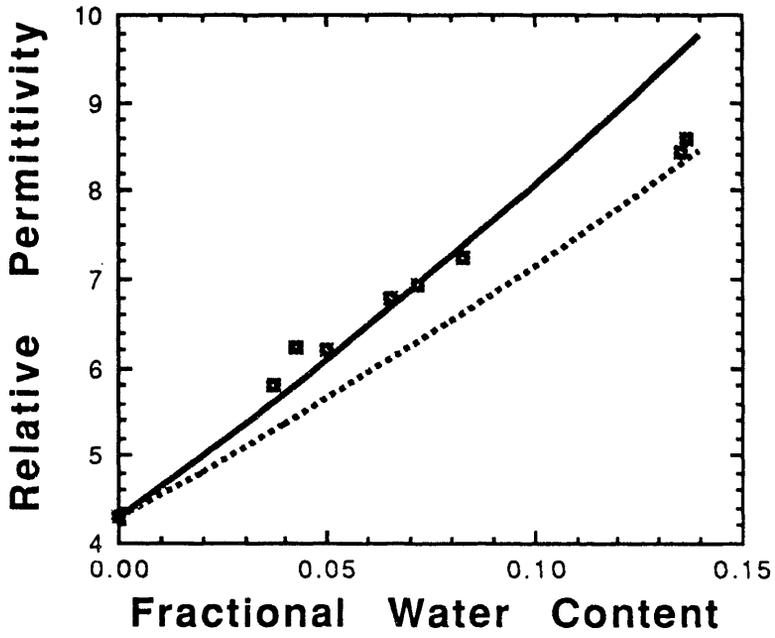

Figure 1-2. Laboratory measured and model calculations of the relative permittivity as a function of water content. The points are laboratory measurements of the electromagnetic permittivity (real part) of densely welded, Grouse Canyon tuff of porosity 0.14. Reflection and transmission coefficients measured in a coaxial air line at 200 MHz were used to calculate the permittivity. Water from Well J-13 was used as the pore fluid. The solid line is the relative permittivity as a function of water content for a multiphase, dielectric mixture model. Spherical inclusions of air ($\varepsilon_r = 1$) and thin needle inclusions of water ($\varepsilon_r = 81$) are dispersed in a background of silicate material ($\varepsilon_r = 5$) of total porosity 0.14. The dashed line is for the same model but with a water permittivity of 56, which is appropriate for pore water at 100°C.

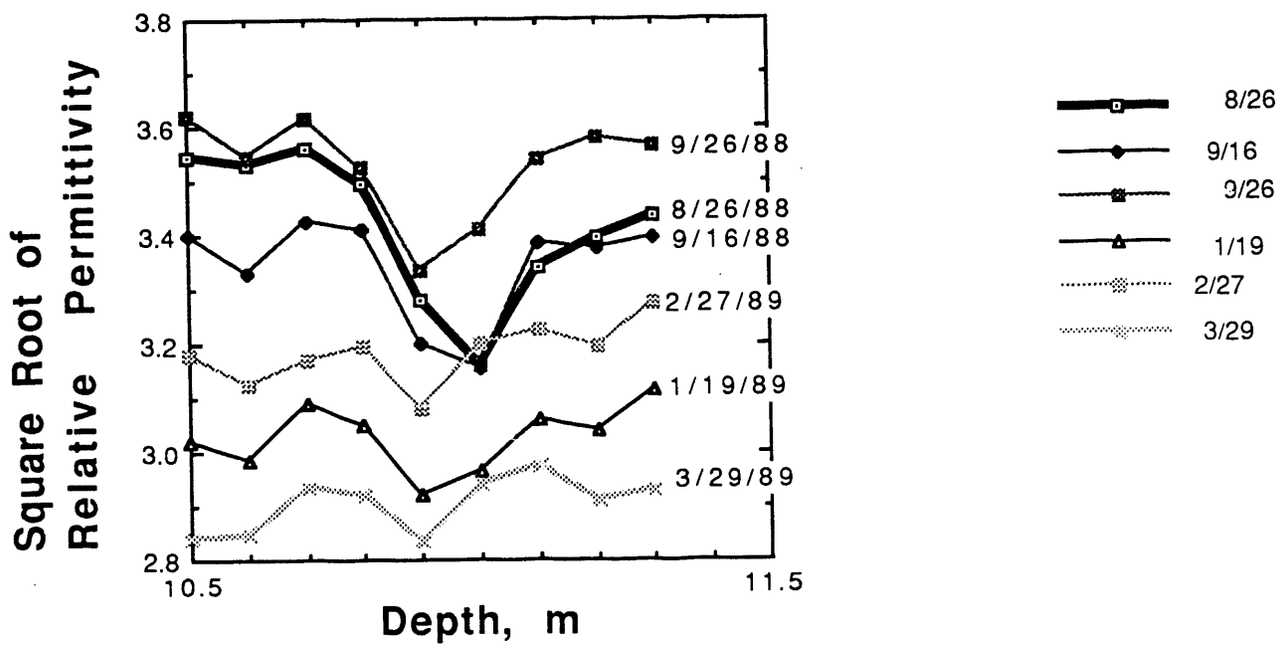

Figure 1-3. Measured square root of relative permittivity as a function of time, along rays for which the transmitter in NE4 and receiver in NE5 were at common depths. Each point is a measure of the right-hand side of Eq. (1-1) divided by the ray path length.

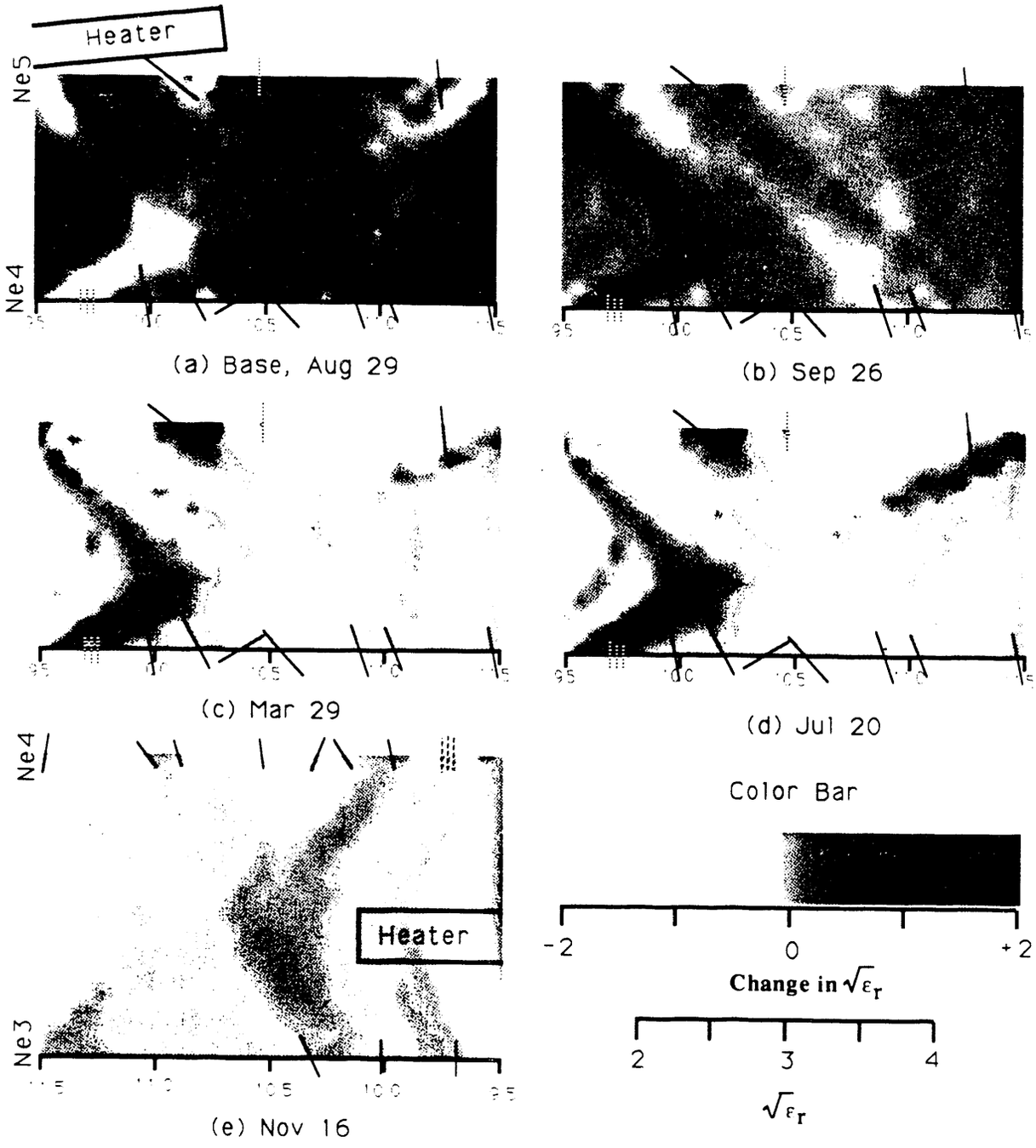

Figure 1-4. Tomographs between NE4 and NE5 and between NE3 and NE4 from 9.5 to 11.5-m depth. (a) Base-line image between NE4 and NE5 of $(\varepsilon_r)^{1/2}$ taken before the heater was turned on, August 26, 1988. Fractures and approximate orientation are shown as logged in both boreholes before the test began. The approximate location of the heater is projected into the image plane. The lower scale of the color bar shows the appropriate range of $(\varepsilon_r)^{1/2}$. (b) Alterant image between NE4 and NE5 of $\Delta(\varepsilon_r)^{1/2}$, for September 26, 1988 (19 days after heater was turned on). The color scale represents the change in $(\varepsilon_r)^{1/2}$ calculated by subtracting the base-line tomograph from the image taken on this date so that an increase in permittivity is positive in the alterant image. The upper scale on the color bar shows the range of $\Delta(\varepsilon_r)^{1/2}$. The image area is 2 by 1 m, contains 416 pixels (each about 9 by 8 cm) and is reconstructed from phase measurements along approximately 440 ray paths. (c) Alterant image as in (b), for March 29, 1989 (8 days after heater was turned off). (d) Alterant image as in (b), for July 20, 1989. (e) Alterant image between NE3 and NE4 of $\Delta(\varepsilon_r)^{1/2}$, for November 16, 1988 (70 days after the heater was turned off). The color scale represents the change in $(\varepsilon_r)^{1/2}$ calculated by subtracting the base-line tomograph from the image taken on this date so that an increase in permittivity is positive in the alterant image. The upper scale on the color bar shows the range of $\Delta(\varepsilon_r)^{1/2}$. The image area is 2 by 1.25 m and is reconstructed from phase measurements along approximately 440 ray paths.

Chapter 2

Changes in Rock Moisture Content Based on Thermal Neutron Measurements

Abelardo Ramirez, Richard Carlson, and Thomas Buscheck

A neutron logging probe was used to detect changes in rock moisture content during the prototype test. The purpose of this activity was to investigate the physical processes that should be represented in conceptual models describing hydrologic processes in fractured, porous, densely welded tuff during a heating and cooling cycle. Single-borehole measurements of thermal neutron counts were used to infer the spatial and temporal changes in the moisture content of the rock mass. These measurements were repeated every two to four weeks. The inferred moisture content information was used to reconstruct the distribution of liquid water in the rock mass as a function of space and time. Conceptual models are proposed based on these data.

This chapter only provides a sample of the data collected, and summarizes key observations, conclusions and proposed conceptual models based on the neutron surveys; most of the data supporting the conclusions described are not shown due to space limitations. The reader is referred to Ramirez et al. (1990) where all of the supporting data is presented and described in detail. The neutron logging probe contains a source of high-energy neutrons and a slow (thermal) neutron detector. The hydrogen present in the water in the rock slows the neutrons for detection. Seven boreholes were used for the moisture content measurements. The measurements were made before the heater was turned on; the measurements were repeated after the heater was energized to monitor temporal and spatial changes in moisture content. Measurements were made every 10 cm (3.9 in.) or 20 cm (7.9 in.), depending on the borehole location, with the probe stationary for 16 s during each measurement; along the remaining boreholes measurements were made with the probe remaining stationary at each location for 16 s (Figs. 3, 4, and 5 in the Introduction of this report show the measurement locations). A paraffin shield included with the probe was sampled at the beginning and end of each logging day to verify that the tool was functioning properly.

Borehole Construction

The layout of boreholes sampled by the neutron surveys is shown in the Introduction (Figs. 4, 5, 7, and 8). The boreholes sampled were NE-1, NE-2A, NE-3, NE-4, NE-5, NE-6, and NE-7. The boreholes surveyed with this tool were sealed with a grout and liner system so that steam and liquid flow along the boreholes were minimized. The presence of the liner/grout system (grout consisted of portland cement, sand, and water; liners were either polycarbonate or Teflon, depending on the maximum borehole temperatures) probably had an effect on the measured values of absolute moisture content. Portland cement grout is made up of hydrated (i.e., bound water) minerals which could have lost water as cement temperatures increased; also, the grout probably had water trapped in its pore space. The behavior of the water in the grout column during the test is unknown. For future tests, laboratory experiments should be performed to quantify this effect and to calibrate the instrument, taking into account the effects of water in the grout. We have chosen to present the data as changes in moisture content rather than absolute values as is discussed below. This should eliminate the effects of constant sources of hydrogen such as the liner material; however, the grout (preheating) contained water trapped in its pore space as well as water of hydration, which probably changed during heating. In the discussions that follow, it is assumed that changes in grout moisture content more or less

parallel the changes in moisture content of the rock. We recognize that changes in grout moisture content impact the measured values, but in a qualitative sense, we expect the measured values to be representative of the changes in the moisture content of the rock mass. This is reasonable given that the data will only be used to propose mechanisms for fluid flow which explain the observations; we will not attempt to use the measurements presented here to quantify these mechanisms. Furthermore, assuming a spherical volume of investigation for the probe with a diameter of 15 cm, it can be shown that approximately 70% of the sampled volume consists of welded tuff; for the 6.1-cm boreholes, approximately 85% of the sampled volume consists of welded tuff. This suggests that the expectation that the measured values represent qualitatively the rock moisture content is reasonable.

Data Reduction

For a counting time of 16 s, the number of counts is approximately 9000 (typical of measurements before heating); assuming that a Poisson's distribution describes the counting process, we estimate that the precision of a single measurement (two standard deviations confidence level) is ±0.0042 g of water per cm^3 (or ± 0.42 vol %). This number multiplied by $\sqrt{2}$ gives us an estimate of the precision in a difference trace of ±0.006 g/cm^3 (0.6 vol%).

A spatial filter was applied to each difference log to smooth the spikes in the trace and to further improve precision. This spatial filter calculates a weighted average for each depth location using 5 points (measurements were made with the probe stationary for 16 s during each measurement every 10 cm (3.9 in.) along radial boreholes NE-1, NE-2A, NE-6, and NE-7; along the parallel boreholes NE-3, NE-4, and NE-5, measurements were made every 20 cm (7.9 in.). Each difference trace was smoothed using this filter to enhance spatial and temporal trends in the data and to improve the repeatability of each difference trace. The precision estimate for the filtered points is ±0.003 g/cm^3 (0.3 vol%). Filtering improves the precision of the data by a factor of 1.96 over the unfiltered data. This precision estimate means that, for any one point on a difference trace that equals or exceeds ±0.003, there is a 95% probability that the difference is caused by true changes in the measurement and a 5% probability that it is caused by random fluctuations.

Sample of Results

Boreholes NE2A, NE6, and NE7 are three coplanar boreholes located near the center of the heater, as illustrated in Figs. 4 and 5 in the Introduction. The data collected along these boreholes can be combined and plotted as a function of radial distance to the center point of the heater assembly as shown in Fig. 2-1. Figures 2-2 and 2-3 show selected samples of radial profiles of changes in moisture content during various stages of the test. Note that these radial profiles are not composed with data collected along a single radial traverse; instead, the profiles represent borehole traverses that sampled many different radial distances along a nonradial route. The changes to be shown were calculated relative to preheating moisture measurements. Each figure consists of two plots that show the same data at two different scales so that the smaller changes, which occur at the more distant locations, can be observed. These radial profiles are used to evaluate the degree of radial symmetry relative to the heater for moisture distribution along the rock sampled by the neutron surveys.

Figure 2-2 shows a radial profile of moisture content change 70 days after the heater was energized. This data was collected near the midpoint of the maximum power phase of the test. As expected, the rock closest to the heater is losing substantial amounts of moisture. However, the rock near borehole NE2A is drying at a faster rate than is the rock near NE6. This might also be due to the way steam condensate drains in the fractures; once condensate forms in the

fractures, water starts draining vertically downward (assuming gravity forces are the controlling factor and not suction pressure gradients). For rock above the heater, the upward penetration of the dry region is slowed by the condensate that drains back along the fractures to the boiling zone, as shown in Fig 2-1. Below the heater, the dry region can penetrate more because the condensate quickly drains and imbibition is slow relative to the velocity of liquid water draining down the fractures.

The radial profile of moisture content change for day 127 (not shown due to space limitations, refer to Ramirez et al. 1990) showed that the rock along NE-6 at radial distances between 0.5 and 1.1 m continued to dry until it approximately matched the conditions along NE-2A. Note that the NE-2A profile shows very little additional drying when compared to Fig. 2-2, while the NE-6 profile showed significant additional drying. Both profiles are now closely matched with the caveat that the width of the drying region appears to be slightly wider near NE-2A. The closely matched profiles suggest that the rock near NE-2A and NE-6 was almost completely dry (at radial distances less than 0.75 m). Also, very little additional drying occurred near NE-2A (at radial distances less than 0.75 m) during the last 57 days while the heater continued to operate at constant power. The radius of the dry zone achieved was approximately 0.7 m; this is consistent with the test objective of achieving boiling conditions within a 0.6–0.7 m radius.

On day 128, the power ramp-down phase began, and on day 195, the phase ended. Other data in Ramirez et al. (1990) show that relatively small changes occurred during the power ramp-down phase. Figure 2-3 shows the changes in moisture content measured 100 days after the heater was turned off (day 301) and the rock temperatures had recovered to within a few degrees of initial conditions. Figure 2-3 shows a similar trend with the exception that the section of NE6 at a radial distance of approximately 0.6–0.75 m (this rock is directly above the heater location) is recovering more moisture than the rock along NE2A at the same radial distance. This means that the rock above the heater is regaining moisture at a relatively faster rate than is the rock below the heater. Mechanisms that explain rewetting behavior are proposed in the next section.

Fractures are an important component of the hydrothermal environment that developed during the test. Data in Ramirez et al. (1990) show that fractures served as flow paths for steam, served to increase the penetration of the drying front, served as condensation points where sufficiently cool temperatures existed, and also served as drainage flow paths for condensate forming in the cooler regions.

Fractures also affected the rewetting observed during the test. Further insights into the rewetting process can be gained by calculating changes in moisture content relative to the last day of full-power heating. Figure 2-4 presents changes in moisture in borehole NE2A, where "after" minus "before" changes are calculated relative to day 127 (i.e., the "before" data corresponds to day 127, next-to-last day of the full-power heating phase of the test). The data were obtained during the power ramp-down and postheating phases of the test when the rock was cooling and rewetting. Also shown are fractures mapped along the boreholes.

Note that the rock regions that show the largest rewetting are clustered around the fractures in NE2A. This is an indication that fractures might play a role in the rewetting process. Numerical modeling conducted for this study indicates rewetting behavior might be dominated by the movement of vapor, primarily by binary diffusion, along fractures. Saturation gradients in the rock mass result in relative humidity gradients that drive water vapor back toward the dried-out zone. As this water vapor reaches the dried-out zone, it condenses along the fracture walls and is imbibed by the matrix. Fractures dominate the bulk permeability of the rock mass (Lee and Ueng, 1989). Relative to an unfractured rock mass, the presence of fractures (and the

very high mobility of vapor driven by binary diffusion) effectively shortens the distance over which water must be imbibed in order to rewet the dried-out region.

Conceptual Models for Drying and Rewetting Behavior

The models proposed below are, to a large extent, similar to the starting conceptual model shown in the Introduction because the results described here and in Ramirez et al. (1990) can be interpreted in a manner consistent with the conceptual model shown in the Introduction. The most significant modifications to the pretest conceptual understanding concerned the contribution of the gas phase to rewetting of the fractured rock mass. Test results showed rewetting occurring along fractures that were considered to be dry. Re-examination of the rewetting behavior predicted by our numerical models showed substantial vapor flux along fractures from wet to dry regions. Other important observations that can be made is that the distribution of changes in moisture was not radially symmetric relative to the heater axis. It has been shown that the rock above the driest zone dried slower but rewetted faster than the rock below the heater. Fractures seem to have increased the rate of drying and rewetting.

The conceptual models shown in Figs. 2-5 and 2-6 propose explanations for these observations. Figure 2-5 presents a conceptual model for the case of a vertical fracture striking parallel to the heater. As temperatures increase, the evaporation rate of pore water increases. As a result, the pressure of the vapor phase also increases and drives gas flow. Note also that the pressure rise elevates the boiling point temperature. In unfractured rock, the vapor phase flow is primarily outward because gas pressure is greater toward the heater; however, near a fracture, vapor phase flow is preferentially toward the fracture because the fracture acts a pressure sink. At a given temperature, rock near a low pressure, high permeability boundary will dry faster because vapor has a shorter distance to travel through a relatively low permeability matrix; therefore, rock near fractures dries faster than the surrounding rock, as shown in the conceptual model. Once the hot gas is in the (approximately) vertical fracture, it will tend to flow upward because fractures are at ambient pressure; the net result is that more steam is likely to condense above the heater location than in other parts. This mechanism may be one reason why the rock above the heater dried slower and rewetted faster than the rock below.

The drainage of steam condensate also plays a role in the proposed model. Water condensing in the fractures will start draining vertically downward. Note in Fig. 2-5 that for the steam flow and condensate flow directions shown along the fracture, the upward penetration of the dry region will be slowed by the condensate that drains back to the boiling zone. Below the heater, the dry conditions reach farther away from the heater because the condensate drains away from the boiling region. The authors believe that the wetting region below the heater location was not detectable during this test because the matrix imbibition flux was small relative to the flux of liquid water draining down the fractures. However, the lower wetting region is likely to extend farther below the heater than the wetting region does above because of condensate drainage along longer vertical paths. The net result of this conceptual flow system is that there is more imbibition of condensate above the dry zone because it stays in contact with the matrix for longer times than below the dry zone where it can escape; these two conditions favor more imbibition of condensate above the heater. Figure 2-6 illustrates this effect better by depicting flow directions for the case of a vertical fracture striking perpendicular to the heater axis. The net effect is that the hot dry rock zone intercepted by the fracture plane acts as an umbrella that stops the downward flow of condensate and gradually sheds it to the sides. This model has also been used to explain temperatures that remained near the boiling point for long periods of time during the test (Lin et al., 1990). Drips of condensate along fractures are also shown in the conceptual model as an additional mechanism that could slow the penetration (upward and sideways) of the dry region.

During the ramp down of power to the heater, temperatures around the heater responded quickly to the decline in heat load. Boiling became less vigorous and ceased roughly midway into the ramp down. During this time, the moisture content of the dried-out zone began to slowly increase, with regions above and to the sides of the heater gaining moisture faster than regions below the heater. Figure 2-7 is a simplified schematic depicting the main rewetting features that might have given rise to the differences in rewetting rates. As the heater power was reduced, boiling continued even though at decreasing rates. Even after boiling ceased, heating of the rock around the heater continued to facilitate evaporation. Recall that above the heater the return flow of condensate in fractures slowed the progress of the boiling front away from the heater, while below the heater condensate drainage in the fractures had little effect on the rate of drying of the matrix. If the region above the heater was being heated linearly from a plane source of heat, there would be a critical heat flux rate at which the return flow of condensate would be balanced by the rate of boiling. For heat flux rates in excess of this critical rate, the boiling front would move away from the heater. For heat flux rates less than the critical rate, the boiling front would move toward the heater. For this test, radial heat flow from the heater complicates this relationship between heat flux and the velocity of the boiling front. However, it should be apparent that as the heating rate is reduced, the boiling front eventually begins to recede towards the heater. To the sides of the heater, the situation is somewhat more complex as condensate draining down fractures from regions above begins to rewet the rock at a faster rate than the boiling rate. Below the heater the rock is essentially shielded from condensate draining down fractures due to the presence of the umbrella provided by the overlying dried-out zone. Therefore, rewetting of the rock below the heater occurs without the benefit of liquid water movement in fractures. Above the heater, liquid water movement along fractures does contribute to rewetting because longer residence times for the condensate allow more imbibition and condensate does not have to travel through a dried-out zone to reach the matrix above the heater.

In the numerical modeling study, it was found that simple matrix imbibition cannot adequately account for the moisture movement observed during the ramp-down and postheating phases. Moreover, below the heater, rewetting rates were observed to be greater in regions of higher fracture density. The fractures appeared to be contributing significantly to rewetting even though it is unlikely that liquid flow was occurring in the fractures below the heater. In the numerical modeling study, it was noted that saturation gradients in the matrix are associated with relative humidity gradients in the gas phase in the fractures as well as the matrix. It was found that large mass flow rates of vapor occurred down the relative humidity gradient due to binary diffusion of water vapor and air.

Darcy flow (i.e., driven by pressure gradients) of air through fractures might have also brought humidity to the dry region. As the hot, dry rock cooled and water vapor condensed, the gas-phase pressure dropped. These lower pressures would drive flow of vapor in the fractures. Capillary condensation of the water vapor occurred along the fracture faces in the dried-out zone with subsequent movement of this condensate into the matrix due to imbibition. Relative to an unfractured rock mass, the presence of fractures (and the very high effective mobility of vapor driven by binary diffusion) effectively shortens the distance over which water must be imbibed in order to rewet the dried-out region. Vapor-phase movement in fractures contributed to rewetting behavior throughout the fractured rock mass. Therefore, even for regions above and to the sides of the heater where liquid movement in the fractures was rewetting the rock, binary diffusion driven flow and Darcy flow in fractures were also contributing to rewetting behavior. Just like the fractures, the heater borehole can serve as a capillary condensation surface as shown in Figure 2-7. The borehole can serve as a vapor pathway connecting the dry region to regions with higher air humidity. Thus, capillary condensation may help re-wet the dry rock around the borehole.

Summary and Conclusions

Thermal neutron logs have been collected to monitor changes in moisture content during the test. Thermal neutron measurements were made before, during, and after the heater was energized. For each borehole, the differences between the "before" and "after" measurements have been calculated ("after" heating minus "before" heating, or "during ramp down" minus "last day of heating"). A spatial filter was applied to each difference log to smooth the spikes in the trace caused by the random fluctuations in the number of neutrons generated by the radioactive source in the probe. The imprecision estimate for the filtered points is ± 0.003 g/cm^3 (0.3 vol%) (95% confidence level). The possibility of changes in the moisture content of the grout column within the sampling boreholes introduces an unknown but possibly significant error on the measured values. Grout column changes might be distorting the moisture content measurements of the rock adjacent to the grout column.

The neutron surveys can be interpreted in a manner consistent with the pretest conceptual model shown in the Introduction chapter. The data show that the moisture content at an arbitrary point in rock above the heater first increases its moisture content as steam generated closer to the heater condenses in cooler adjacent areas. This "halo" of increased moisture subsequently subsides as the temperatures and evaporation rates at this point increase. The diameter of the drying region grows faster at first, and then at an increasingly slower rate as the volume of rock to be heated increases. As the heater power decreases, the moisture content at this point slowly increases. As expected, the drying front appears to have penetrated farther along some fractures during the maximum power stage; fractures also increased the rewetting rate during the cool down and postheating stages of the test. The neutron surveys can also be interpreted in a manner consistent with the conceptual model based on HFEM results (Chapter 1).

Plots of change in moisture content as a function of radial distance show that the changes are not radially symmetric relative to the heater borehole axis. The data show that there are significant differences in drying and rewetting behavior of rock above and below the heater. The rock below the heater dried faster than the rock above the heater at equal radial distances. During the power ramp-down and postheating phases, the rock directly above the heater rewetted at a slightly faster rate than did the rock below.

Conceptual models have been developed based on the results shown here and in conjunction with the numerical modeling study to explain differences in the drying and rewetting behavior above and below the heater. In general, water vapor generated in a matrix block moves toward the closest fracture face (or surface of the heater borehole if the block is adjacent the borehole). Upon entering the fracture, water vapor tends to move radially outward through the fracture system until it condenses. Due to the heater borehole moisture collection system and condensation on the heater packer, some of the vapor in the fractures moves radially inward toward the heater hole. Water that condenses above the heater drains downward through the fractures. Much of this downward flow intersects the boiling zone and is reboiled, thereby slowing the upward progress of the boiling front. Some downward flow of condensate was observed to be reboiled at the lower flank of the heater, thereby stabilizing the boiling front at that location. Water that condenses below the heater drains away from the boiling zone. Because matrix imbibition is slow relative to the condensate generation and drainage rates, most of the downward drainage of condensate below the heater leaves the system before it can be subsequently reboiled. It was also observed that the boiling zone effectively acts as an "umbrella" shielding the rock below the heater from the downward drainage of condensate generated above the heater. Rewetting of the rock above the heater and to one side of the heater was observed to be partially the result of condensate drainage in fractures. Throughout the fractured rock mass, rewetting also occurred via binary diffusion of water vapor (driven by relative humidity gradients) and via Darcy flow (driven by pressure gradients). As this water

vapor reaches drier rock, it condenses along the fracture faces (by capillary condensation) and is imbibed by the matrix.

Recommendations for Future Work

As a result of the work described in this report, we can propose recommendations for the use of neutron logging tools in future tests of the near-field environment around a heater. The effect of the grout-liner system needs to be better understood and/or minimized. It can be minimized by: (1) reducing the size of the annular space filled with grout, and (2) using a probe with a substantially bigger sampling volume (this will lower spatial resolution). If a cement grout is used again, there is a need to establish quantitatively the influence that the grout column has on the measured values of moisture content; this can be done via a calibration process wherein the moisture content of large welded tuff cores (with grout sealed boreholes) is determined as a function of temperature by correlating weight changes versus thermal neutron counts. The test results suggest that there is an asymmetrical distribution of moisture content that develops around the heater. To better characterize this distribution, we suggest that radial boreholes (i.e., parallel to heater borehole radii) be considered; in particular, a radial vertical borehole is strongly recommended. Moisture measurements also need to be made well below the boiling zone in order to track the vertical and lateral extent over which condensate drainage in fractures can occur.

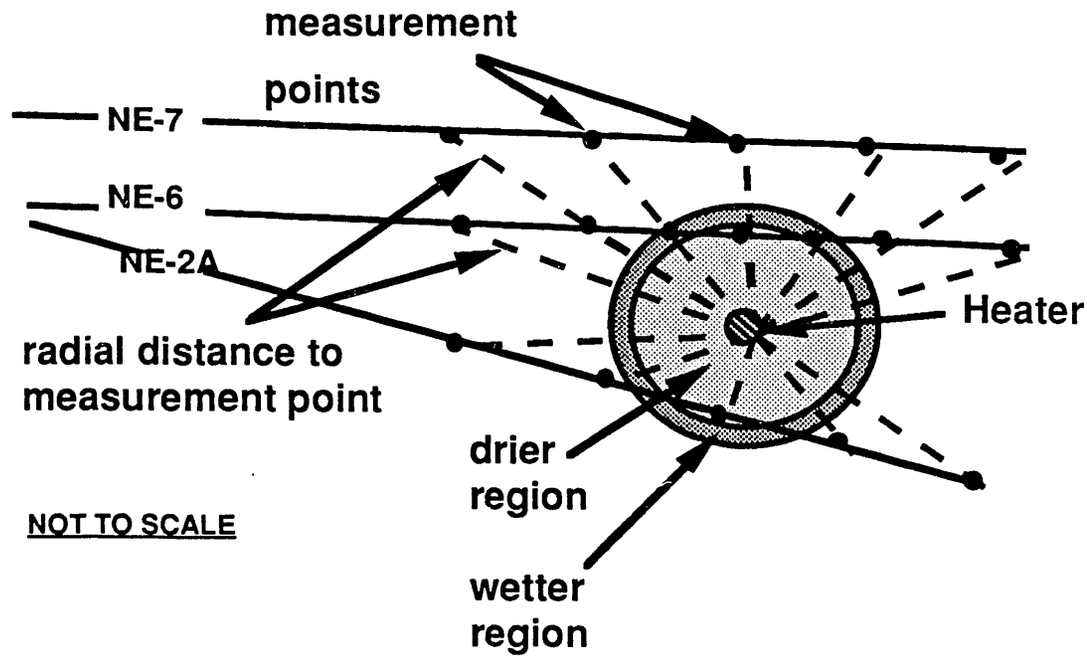

Figure 2-1. Data collected along three coplanar boreholes near the middle of the heater (boreholes NE-2A, NE-6 and NE-7) can be plotted as a function of radial distance as illustrated above.

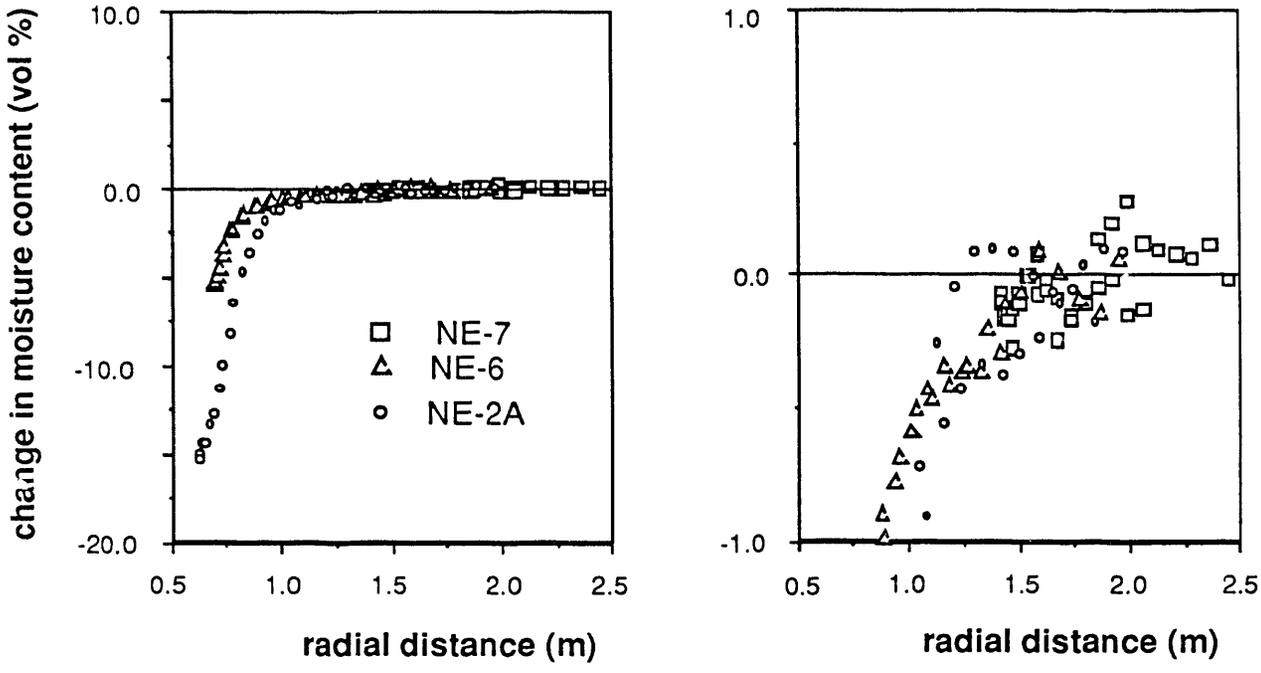

Figure 2-2. Changes in moisture content plotted against radial distance after 70 days of heating (approximately midway through the full-power phase). Changes are calculated relative to preheating moisture conditions.

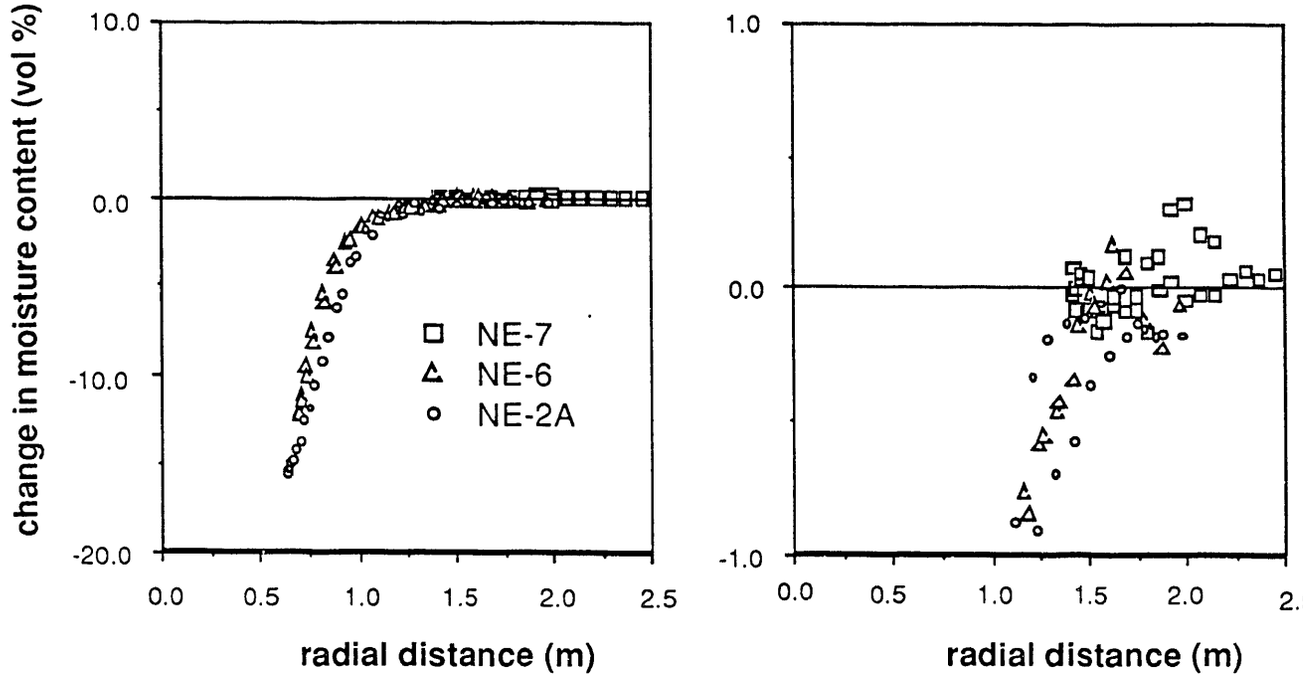

Figure 2-3. Changes in moisture content plotted against radial distance 301 days after start of heating (106 days after heater was de-energized). Changes are calculated relative to preheating moisture conditions.

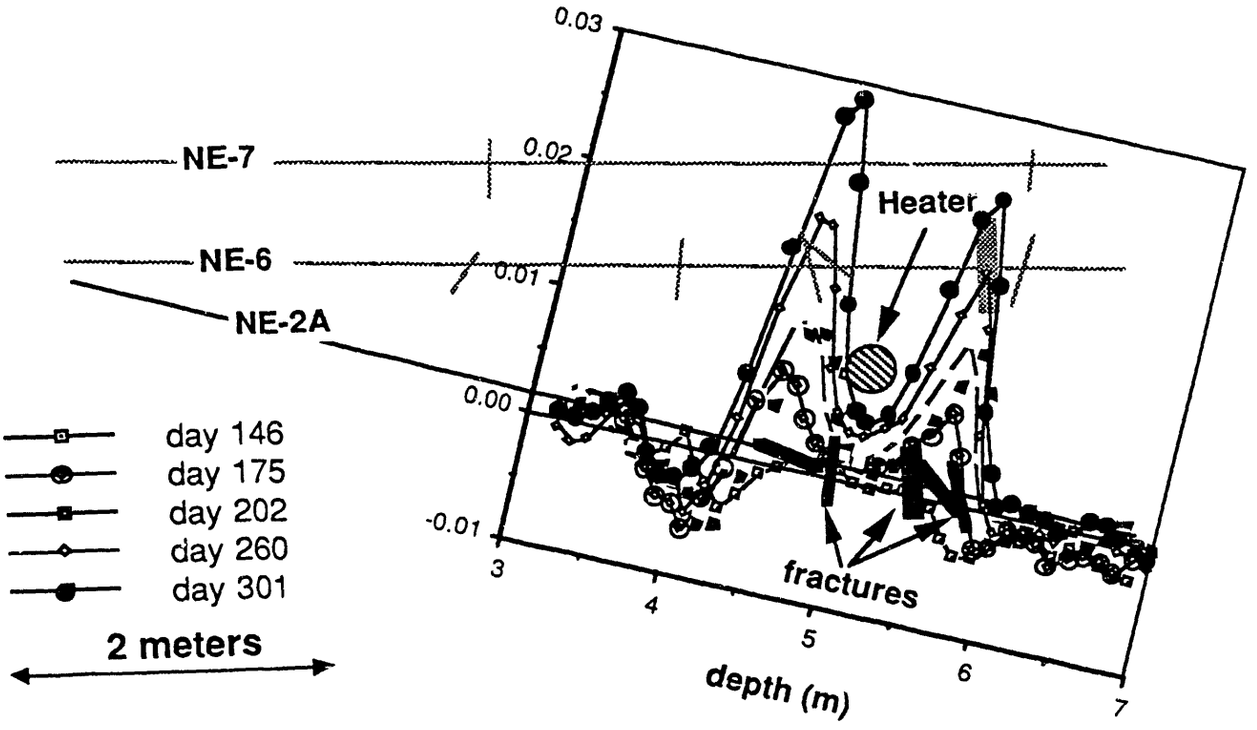

Figure 2-4. Changes in moisture content (in vol%) mapped along borehole NE2A. Changes are calculated relative to the last day of full-power heating, which was on day 128. Also shown are the location of boreholes NE7, NE6, fractures mapped with a borehole TV camera, and the heater.

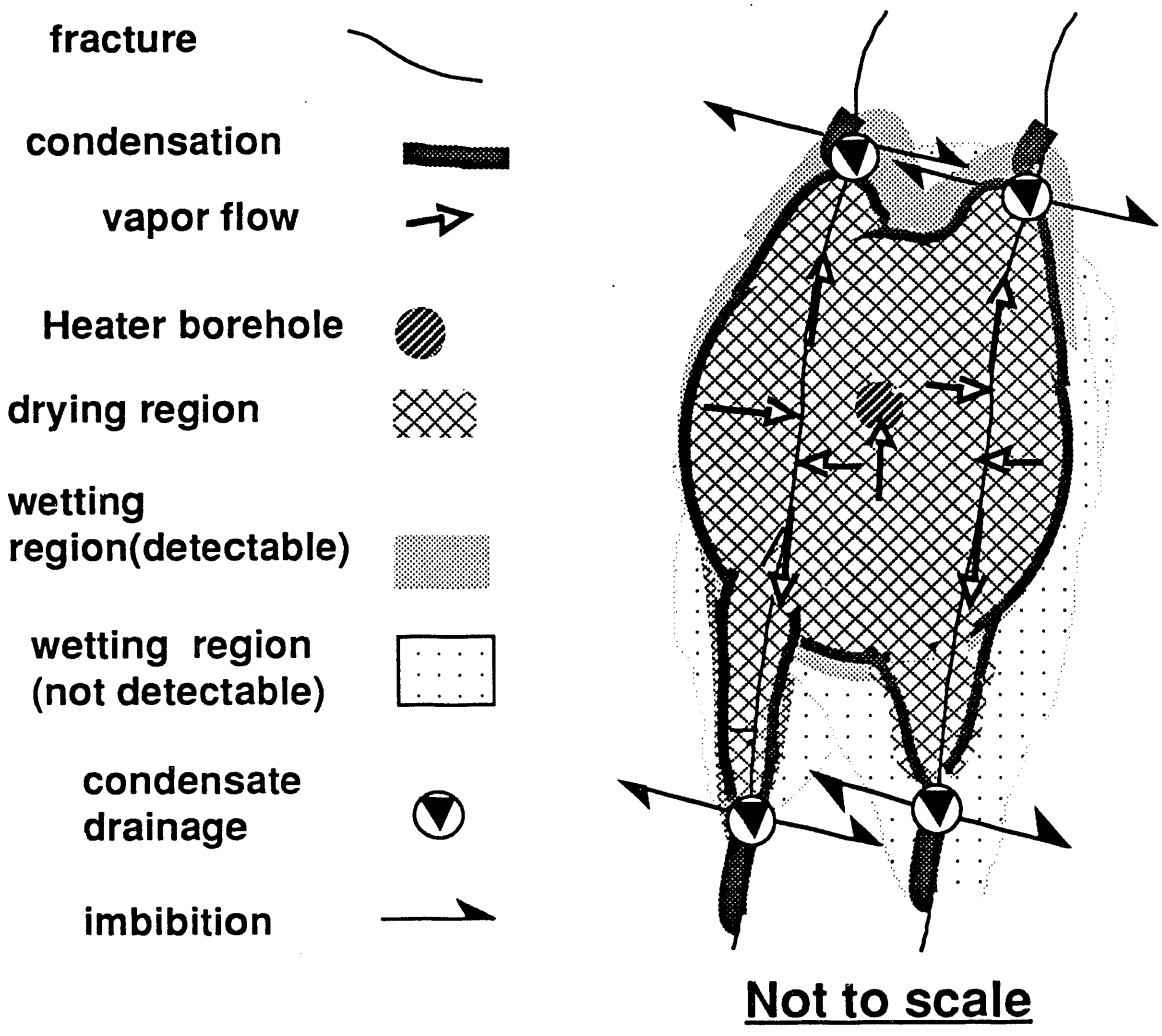

Figure 2-5. Conceptual model proposed for the flow above and below the heater for the case of a fracture striking parallel to the heater axis. A transect along a matrix block intersected by a fracture is shown.

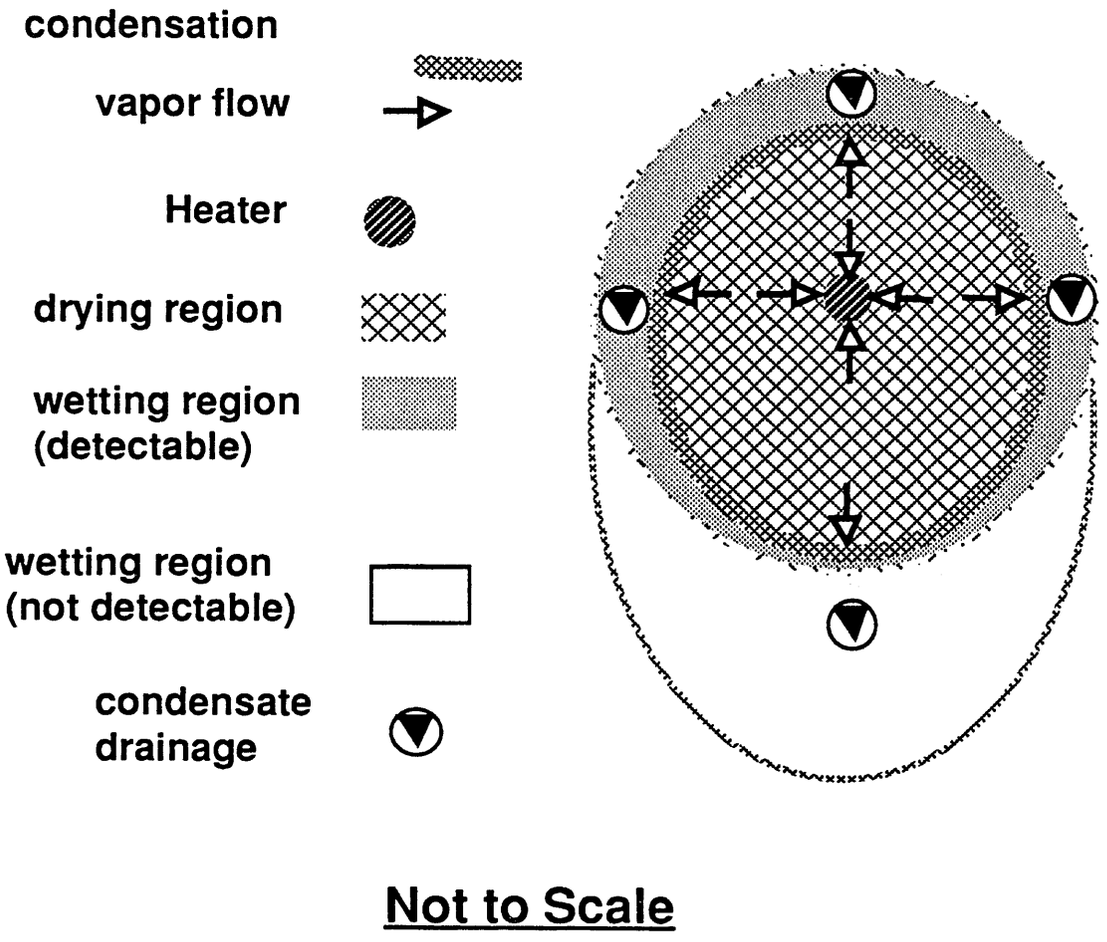

Figure 2-6. Proposed flow phenomena for the case of a vertical fracture perpendicular to the heater axis. The view is along the fracture plane.

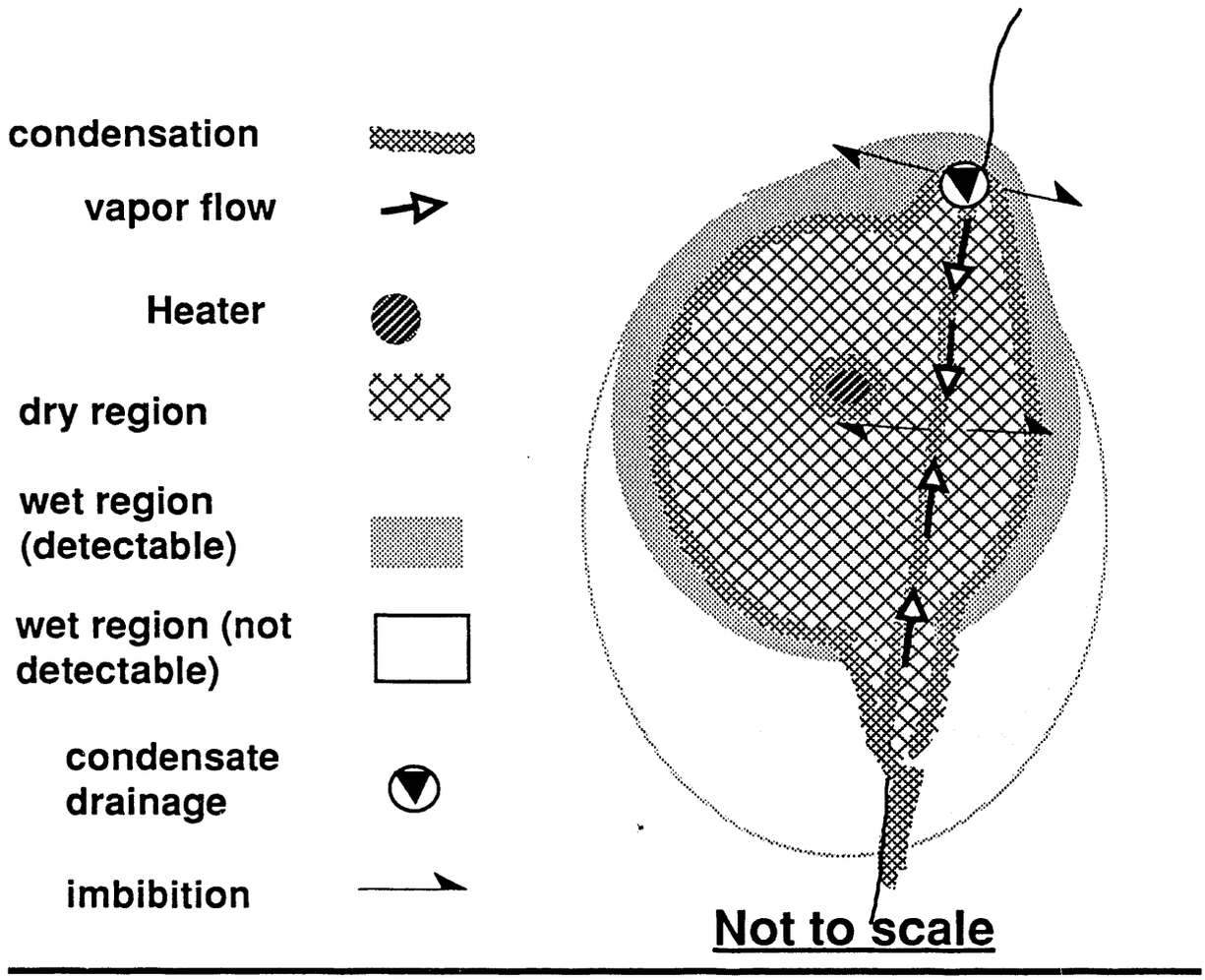

Figure 2-7. Proposed conceptual model of the mechanisms that dominate the rewetting process of the dry region during cooldown of the rock mass. A transect along a matrix block intersected by a fracture is shown.

Chapter 3

Permeability Tests

Kenrick Lee and Tzou-Shin Ueng

As part of the PEBSFT in G-Tunnel, we conducted single-borehole air injection tests to characterize the in-situ permeability of the fractured tuff around the heater emplacement borehole and to determine the effect of a heating and cooling cycle on the rock mass permeability. Prior to heating the rock mass, we used inflatable pneumatic packers to isolate and test selected borehole intervals. The equivalent porous medium (or bulk) permeability of the rock adjacent to a test interval, and the aperture of fractures intersecting the interval, were computed from the air flow rate, temperature, and pressure at steady state. After the heating and cooling cycle, we repeated these tests and compared the preheating and postheating borehole permeability profiles.

This chapter presents a brief description of the permeability testing method and a summary of the results. Additional details will be published in a separate report now being prepared.

Apparatus

Figure 3-1 shows the arrangement of the G-Tunnel air permeability testing equipment. The straddle packer assembly, composed of three inflatable packers, was fitted to a 51-mm (2-in.) aluminum pipe. Each packer had a seal length of 43 cm (16.9 in.) and an uninflated diameter of 27.9 cm (11 in.). The length of the borehole test zone straddled between two packers was 36 cm (14.2 in.). A single 6.35-mm (1/4-in.) line was used to inflate all three packers to about 689 kPa (100 psi) with nitrogen supplied from a cylinder. When the packers were inflated, the assembly isolated three zones in the 30.5-cm (12-in.) borehole. Air was injected through separate 25-mm (1-in.) lines leading to the isolated zones. The temperature in each zone was measured with a Type E thermocouple. The air pressure was transmitted through a plastic tube and measured with a pressure gage located outside the borehole. The thermocouple and the plastic tube were fitted to two ports provided at the back end of each packer. The thermocouple extension wires and the plastic tubes were fed through the aluminum pipe.

The compressed air from the G-Tunnel line flowed through an air filter and a pressure regulator before it entered a four-branch manifold. Each branch contained a flow meter capable of measuring a different range of flow rate. The manifold covered flow rates ranging from 0.5 to 6300 Standard Liters per minute (SLM) (0.018 to 222 SCFM). The pressure regulator maintained a constant test zone pressure as the flow rate adjusted to the steady-state condition. To determine the mass flow rate of a highly compressible fluid such as air, the thermodynamic character of the fluid expansion must be considered. Therefore, the temperature and pressure of air leaving the manifold were measured by an in-line thermocouple and a pressure gage before being transmitted to the isolated zones.

Pressures were read by pressure transmitters with an accuracy of 0.5% of full scale. These transmitters provided mechanical readings as well as electrical signals for automatic recording. Variable area flow meters measured flow rates with an accuracy and repeatability of 2% and 0.5% of full scale, respectively. Calibrations of the pressure gages, flow meters, and thermocouples were performed before and after field testing. Temperatures and pressures measured in the manifold and isolated test zones were recorded by the data acquisition system (DAS).

Testing Procedures

The packer assembly was first placed in the deepest location—about 30 cm from the bottom of the borehole. To secure the packer assembly, the aluminum pipe was attached to rock bolts adjacent to the borehole collar. We then inflated the packers to isolate three zones in the borehole: Zone 1, between the central packer and the packer nearest the borehole collar; Zone 2, between the central packer and the deepest packer; and Zone 3, behind the deepest packer. Zone 1 and Zone 2 each had a fixed length of 36 cm (14.2 in.), while the length of Zone 3 varied with the location of the packer assembly.

Compressed air was injected into Zone 2 at three to five different steady-state pressures ranging from about 14 to 207 kPa (2 to 30 psi), followed by similar injections into Zone 3. Zone 1 functioned only as an observation zone. To approximate steady-state conditions, air injection was continued until the observed flow rate and test zone pressure remained constant for at least 10 min. The injection pressure was limited to a maximum value of about 207 kPa (30 psi) to minimize the effects of fracture deformation and turbulence, which might introduce significant errors in the measurements. For borehole intervals that included very large fractures, it was not possible to establish steady-state pressures of more than a few psi and, therefore, only one or two steady-state pressures were used.

During air injection, the flow rates and test zone pressures were recorded manually. In addition, the DAS recorded temperatures and pressures in the manifold and borehole zones automatically at 1-min intervals. When a test zone was pressurized, the remaining two zones served as observation zones. Pressures and temperatures were monitored in observation zones to warn of any air leakage around or through the packers.

When one packer assembly location was completely tested, the assembly was moved outward about 25 cm (9.8 in.) and tests on Zones 2 and 3 were repeated. This sequence was repeated until a length of about 4.5 m (14.8 ft), measured from the bottom of the borehole, was completely tested.

Data Analysis

The use of fluid injection for bulk permeability tests in fractured rock assumes that the scale of the fractures is small relative to the scale of measurement, so that an equivalent continuum analysis is justified. For gas flow through porous media, under both laminar and turbulent conditions, the appropriate flow equation is Forchheimer's quadratic equation, which in radial coordinates is (Katz et al., 1959)

$$-\frac{dP}{dr} = \frac{\mu q}{k} + \beta \rho q^2 \qquad (3\text{-}1)$$

where

P = gas pressure
r = radial flow distance
μ = viscosity
q = Darcy velocity
k = bulk permeability
β = turbulence factor
ρ = density.

The relevant continuity and constitutive equations are:

$$Q_m = 2\pi r \rho q L \tag{3-2}$$

and

$$\rho = \frac{MP}{ZRT} \tag{3-3}$$

where

Q_m = mass flow rate
L = length of borehole interval
M = molecular weight of gas
Z = gas compressibility factor (approximately 1.0 for the low pressures used here)
R = universal gas constant
T = absolute temperature.

For steady-state radial and isothermal flow of a gas injected into a packed-off borehole interval, Eqs. (3-1), (3-2), and (3-3) can be used to derive the following equation from which the bulk permeability is obtained:

$$\frac{\pi L M (P_b^2 - P_e^2)}{\mu R T Q_m \ln(r_e/r_b)} = \frac{\beta Q_m (1/r_b - 1/r_e)}{2\mu\pi L \ln(r_e/r_b)} + \frac{1}{k} \tag{3-4}$$

where P_b is the borehole injection pressure, r_b the borehole radius, and r_e the effective radius, or radius at which the pressure returns to the ambient value P_e.

Equation (3-4) may be rewritten in the form of a linear equation:

$$Y = \beta X + \frac{1}{k}. \tag{3-5}$$

This linear relationship can be plotted to obtain the bulk permeability k from the inverse of the intercept and the turbulence factor β from the slope. Therefore, k and β can be determined for a borehole test interval by conducting steady-state injection tests at two or more injection pressures.

One practical difficulty in applying Eq. (3-4) to single-borehole fluid injection measurements is the need to measure two boundary pressures in the rock. The first boundary pressure is the injection pressure, which is easily measured in the packed-off borehole interval. The second boundary pressure is usually taken as the ambient fluid pressure, which for this test is barometric pressure. Therefore, an effective radius r_e, or radius of influence, must be estimated. Because the test area is bounded on one side by a wall of the small-diameter heater alcove at a distance of 5 m from the heater borehole axis (see Fig. 4 in the Introduction), we use 5 m as an estimate for r_e.

To make rough estimates of the apertures of fractures intersecting the heater borehole, we assume that the fractures behave like smooth, parallel plates oriented normal to the borehole

axis. For n fractures of equal aperture intersecting a borehole interval of length L, the aperture is

$$e = \left(\frac{12Lk}{n}\right)^{1/3} \tag{3-6}$$

Preheating Permeability Results

Figure 3-2 shows bulk permeability values that were calculated from measurements along the length of the heater borehole, from 6.25 m to a total depth (TD) of 10.72 m. Mapped fracture locations are also shown. The bar location and width represent the actual position and width of the test interval. The permeability varies from a minimum of 0.08 darcy at a depth of 9.23 m to a maximum in excess of 144 darcys. We were unable to quantify the largest permeabilities, which occurred within intervals centered at depths of 6.73, 7.48, and 7.73 m, where highly fractured zones were mapped. At these locations, flow rates in excess of 100 scfm were generated by injection pressures of only a few KPa. Therefore, we were unable to make at least two sufficiently distinct pressure measurements to allow application of Eq. (3-4) for bulk permeability determination. In general, higher permeabilities correlated with mapped fractures.

Figure 3-3 shows estimates of the equivalent parallel plate apertures of fractures along the borehole. Estimated apertures vary from a minimum of 70 microns at a depth of 9.23 m to a maximum of about 589 microns at a depth of 6.98 m. As with the bulk permeability results, measurements made in the highly fractured zones could not be used to estimate apertures. At some test intervals along the borehole, Fig. 3-3 shows fracture apertures estimated where no fractures were mapped. Since the matrix permeability of the rock is on the order of microdarcys (Appendix A), it appears that the resolution of the television camera mapping (Ramirez and Wilder, 1989) accounted only for relatively major features, omitting smaller fractures that allowed substantial flows in some intervals where no fractures were mapped. For these intervals with no mapped fractures, an equivalent single fracture aperture was computed. One such borehole interval, centered at 9.23 m, yielded the minimum aperture of the profile.

Effect of Heating and Cooling Cycle

The heating and cooling cycle resulted in some significant increases in bulk permeability along the borehole. In Fig. 3-4, the borehole permeability profile prior to heating is compared with the profile following the heat cycle. Because the measurement system could not adequately measure the high permeabilities of the test intervals centered at 6.73, 7.48, and 7.73 m, we were unable to make any meaningful comparisons at these three intervals. Computed permeability increases vary from 10% to more than one order of magnitude. It is significant that there is always an increase. If the changes were due to random error, scatter would be expected. Figure 3-5 shows the percentage increase as a function of depth along the borehole. The maximum increase is 1830% at a depth of 8.98 m. Higher percent increases in permeability seem to occur closer to the midpoint of the heater axis, implying that sections of the rock mass that are heated to higher temperatures show larger percent permeability increases. However, the higher relative increases also occur in the intervals of lower initial permeability, most of which happened to be located closer to the midpoint of the heater axis.

To determine any possible effects of the repeatability of the measurements on comparisons between preheating and postheating results, six air injection measurements were repeated to determine any deviations from the original bulk permeability values. Deviations ranged from

0.5 to 8.7%. The maximum deviation is quite small considering the large permeability changes observed over small distances.

Discussion of Results

The reasons for the observed increases in permeability along the heater borehole are unclear, however, we can suggest a few possible mechanisms. Thermal expansion might have caused some relative movement or shearing across the fracture surfaces. For a fracture of significant roughness, such movement would result in some dilation as surfaces ride up asperities causing an increase in the average fracture aperture. Contraction associated with cooling might have lessened the aperture increase but probably not attain the original fit to return the aperture to its preheating value. Nonrecoverable fracture aperture and rock mass deformation have been identified by previous investigators, particularly for fractures experiencing shearing. Some implications of this for permeability changes due to waste (heater) emplacement are discussed in Wilder (1990).

Thermally induced microfracturing is another possible cause for the permeability increase; significant microcracking has been observed in granites heated above 200°C (Wang et al., 1989) but was not identified in quartz monzonite exposed to both radiation and heat (but lower than 200°C) at the Spent Fuel Test—Climax (Beiriger and Durham, 1984). Thermally induced microfracturing could have created new fractures and propagated existing fractures. However, since the bulk permeability of this welded tuff is dominated by larger fractures, it is doubtful that microfracturing could have been the major mechanism responsible for the observed large increases in permeability. The original permeability noted in areas where no fractures were seen were in the order of 1 darcy. Presumably, this was due to fractures too small to be seen. An increase in number of these small scale fractures would account for a change of no more than a few to a few tens of darcys since permeability is a linear function of number of fractures (see Eq. 3-6), but is a function of the cube of the aperture.

Dehydration of clay minerals might have also contributed to the permeability increase. Although no attempt was made to analyze the filling material from fractures logged from the heater and instrument boreholes, smectites are present in small to moderate amounts (1–10%) in virtually all stratigraphic units in Yucca Mountain (Bish, 1985). If a significant amount of clay was present in the fractures tested in G-Tunnel, then clay dehydration could have resulted in an increase in average fracture void volume, and, therefore, an increase in bulk permeability of the rock. As noted in Eq. 3-6, permeability changes as cube of aperture but only linearly with number of fractures. Therefore, a small change in aperture from clay dehydration would result in a possibly significant change in k.

Finally, a higher water saturation in the fractures prior to heating, compared with the water saturation following the heat cycle, has the potential to cause an apparent permeability increase. However, when the matrix is partially saturated, the fractures are essentially dry because of the higher capillary suction forces in the matrix pores adjacent to the fractures (Klaveter and Peters, 1986). Therefore, it would seem that essentially all the drilling fluid pumped into the rock (drilling ended about two months before the beginning of permeability measurements) was either drained away through the predominantly vertical fractures or imbibed into the rock matrix. It is possible that the relative permeability to gas through the rock matrix would be considerably higher once water was removed from all the pores. However, the k values in matrix are so small that even an order of magnitude increase would not cause the substantial increase noted in k.

Conclusions and Recommendations

The bulk permeability measured in intervals along the heater emplacement borehole showed a high degree of heterogeneity, varying from a minimum of 0.08 darcy to a maximum of more than 144 darcys. Equivalent parallel-plate hydraulic apertures of fractures intersecting the borehole varied from a minimum of 70 microns to a maximum of about 589 microns. A comparison of borehole permeability profiles before and after the heat cycle showed significant permeability increases resulting from the heat cycle. Increases ranged from 10 to 1830%.

In future tests, an attempt should be made to eliminate uncertainties concerning the possible effects of preheating and postheating fracture saturation differences. This can be accomplished by a third measurement of the borehole permeability profile, after a sufficiently long period is allowed for the rock to return close to the moisture conditions that existed during the preheating measurements. The rewetting process might be accelerated by flooding the borehole and then measuring the rock moisture content with either neutron gage or high frequency electromagnetic (HFEM) methods to determine when the preheating moisture conditions are attained.

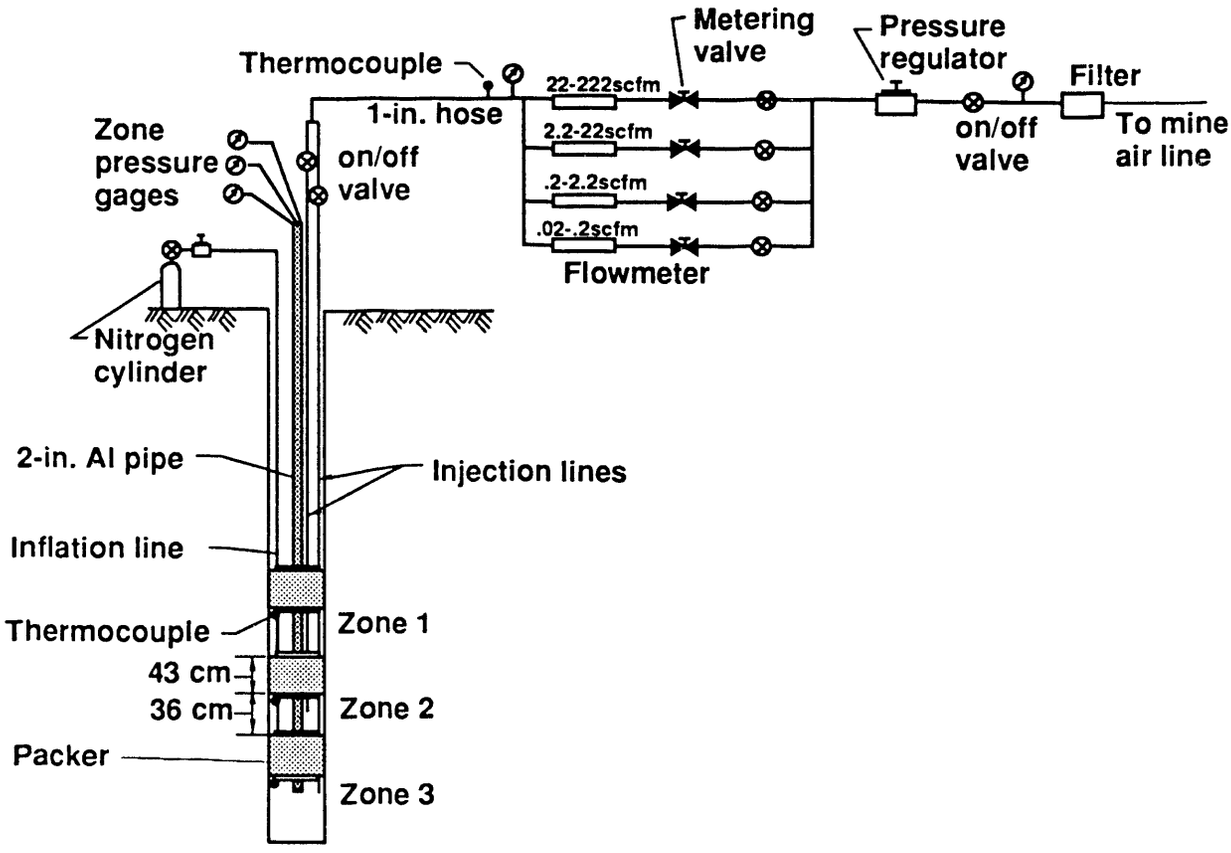

Figure 3-1. Schematic of gas permeability measurement apparatus.

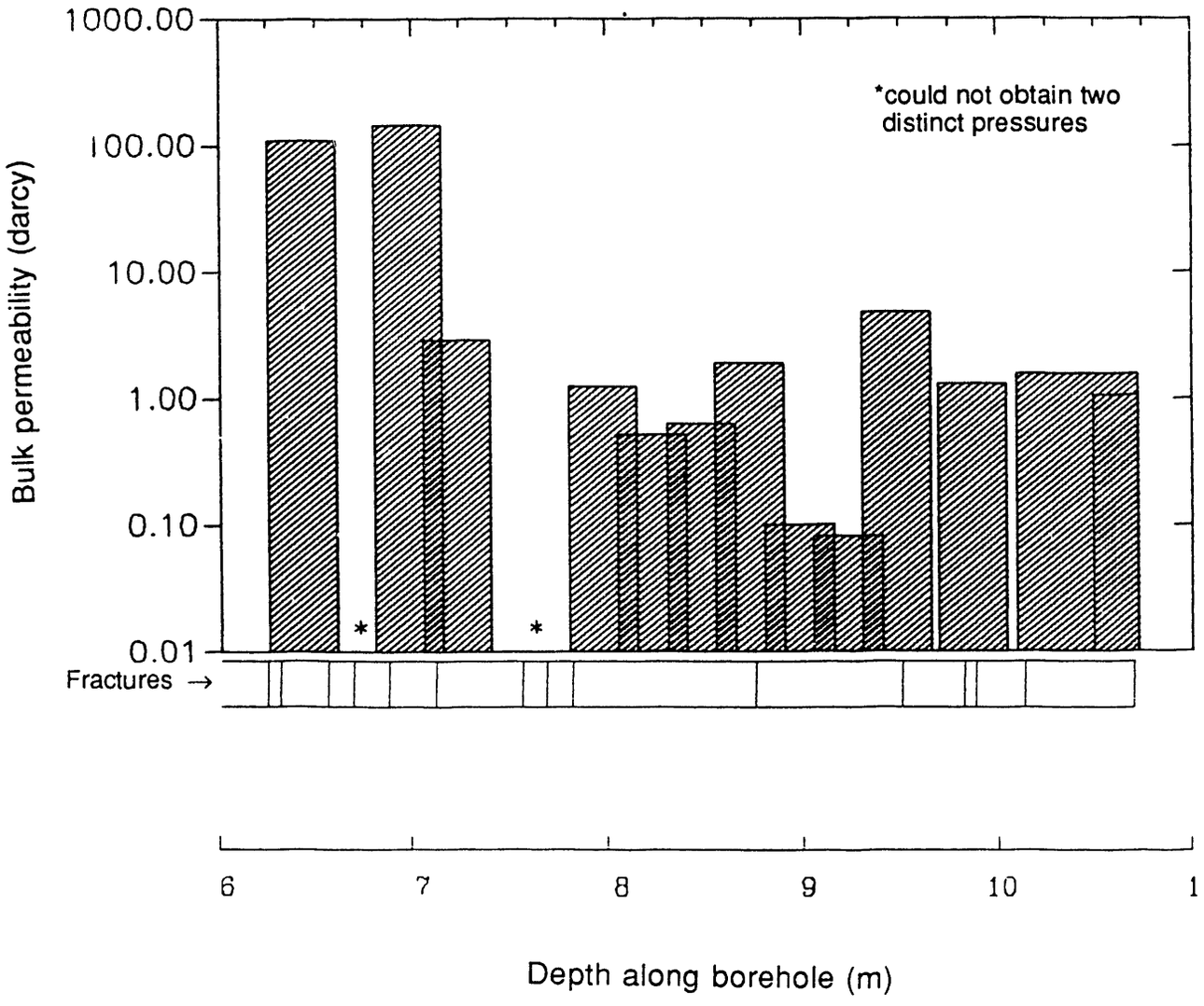

Figure 3-2. Preheating bulk permeability and mapped fracture locations between depths of 6.25 and 10.72 m along heater borehole. Bar width equals length of test interval.

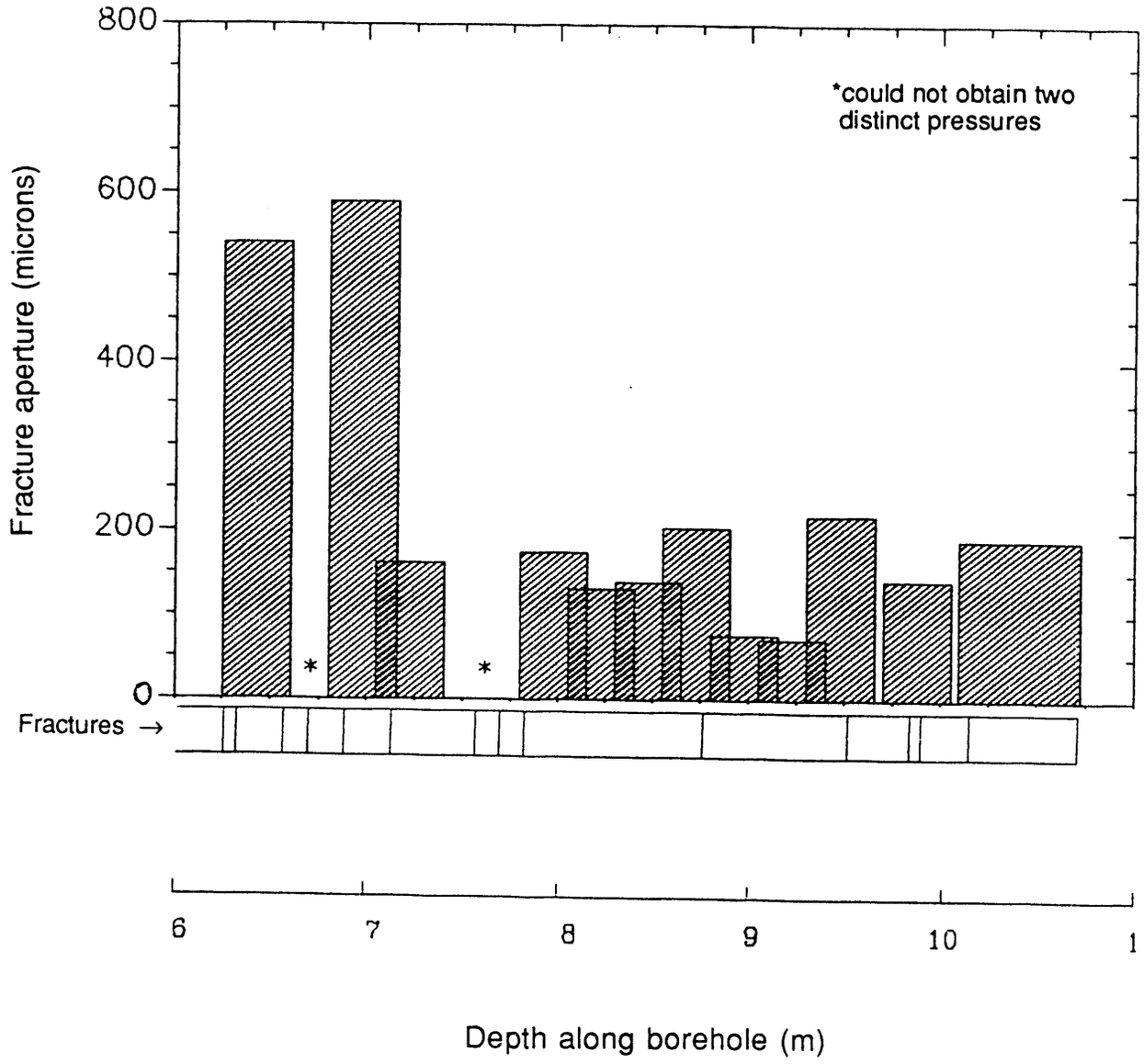

Figure 3-3. Preheating fracture apertures and mapped fracture locations between depths of 6.25 and 10.72 m along heater borehole. Bar width equals length of test interval.

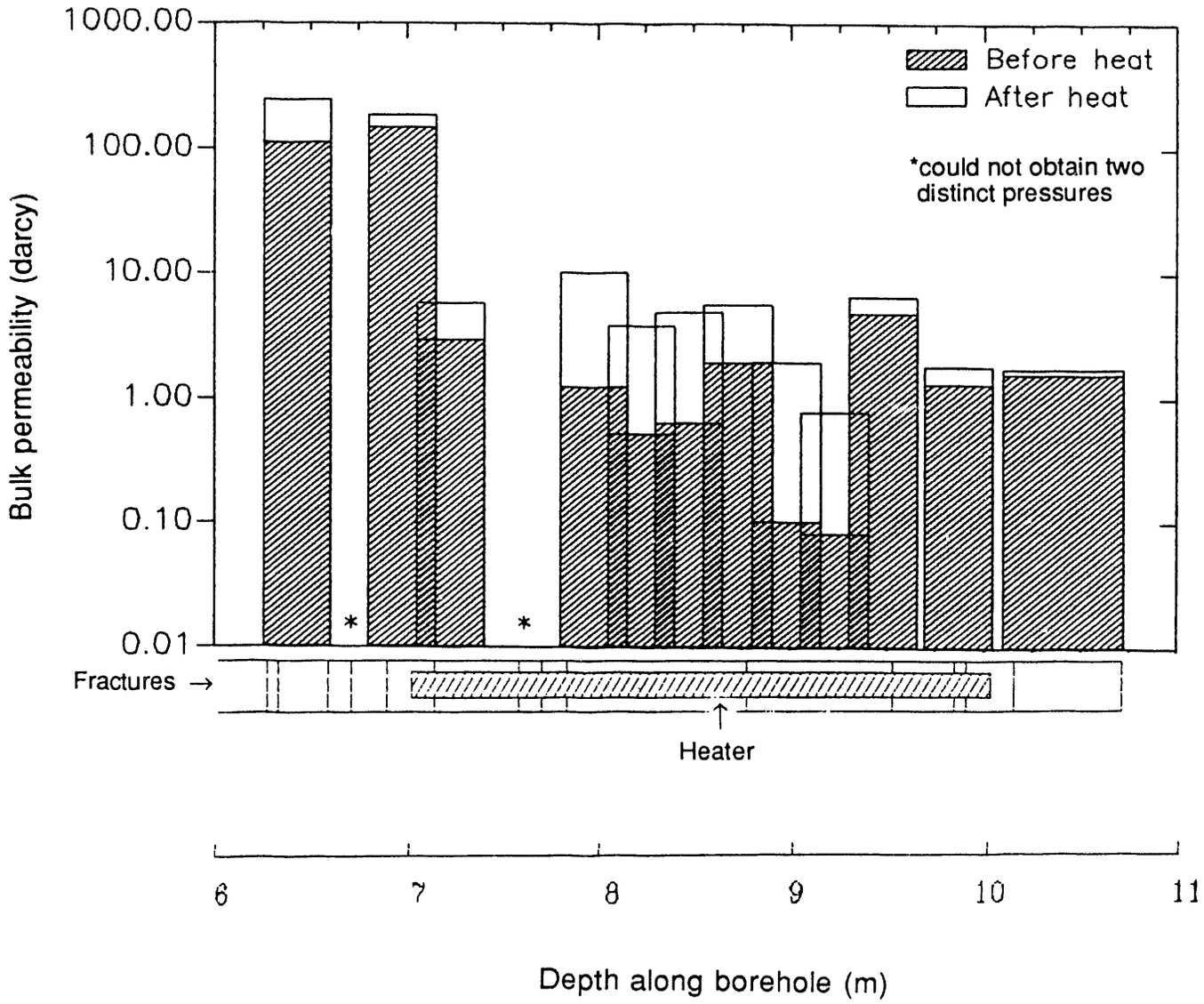

Figure 3-4. Comparison of preheating and postheating bulk permeability values along heater borehole. Locations of heater and mapped fractures indicated. Bar width equals length of test interval.

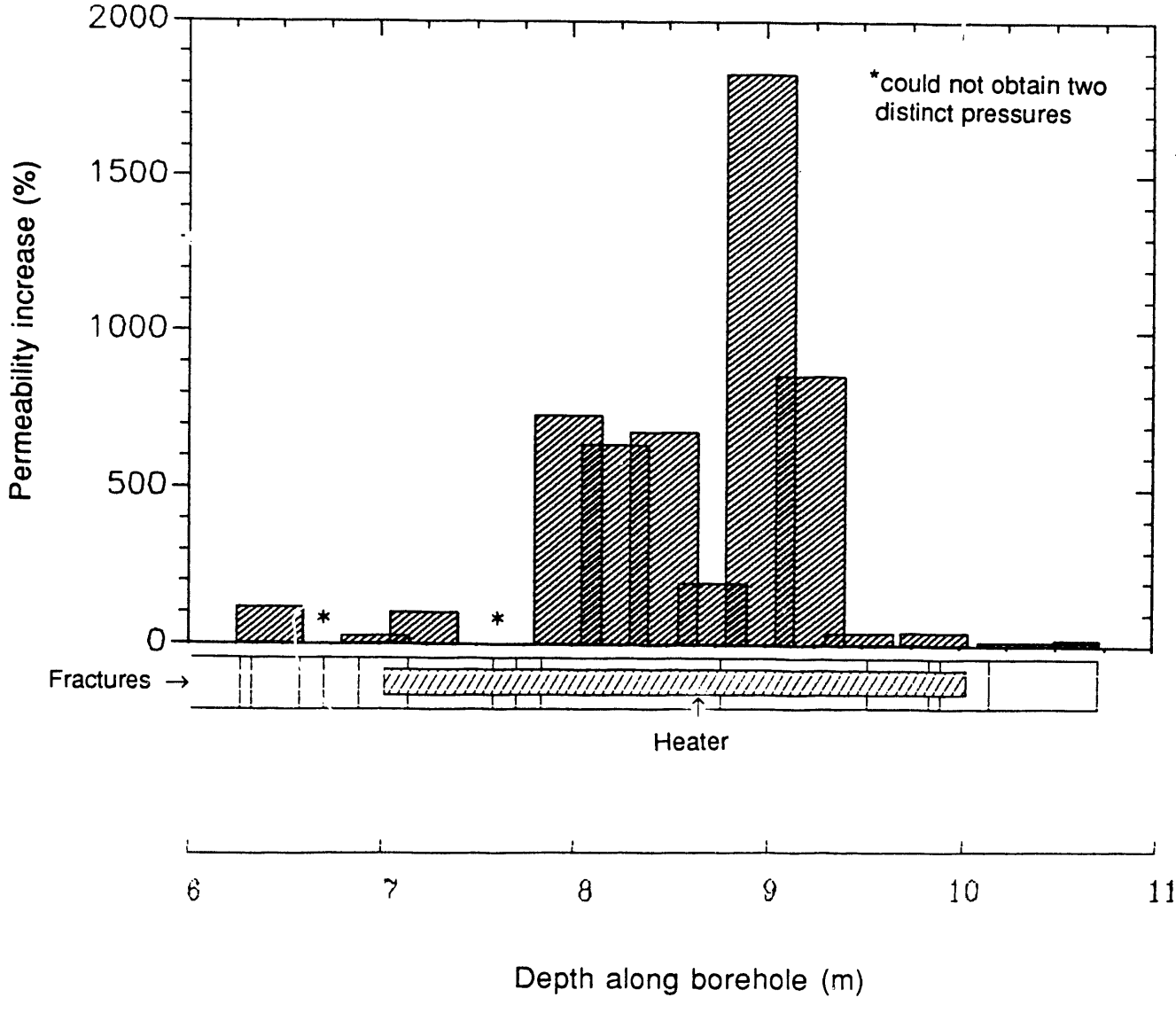

Figure 3-5. Percent bulk permeability increases following heat cycle. Locations of heater and mapped fractures indicated.

Chapter 4

Moisture Collection System

Kenrick Lee and Tzou-Shin Ueng

In an attempt to monitor the quantity of water migrating into the heater emplacement borehole, a moisture collection system was built to trap and measure the moisture volumes. A schematic of the borehole equipment for moisture collection is shown in Fig. 4-1. The borehole was sealed by a high-temperature inflatable packer fitted to a 51-mm (2-in.) I.D. aluminum center pipe. A relative humidity sensor, sticking out of the center pipe inlet, made relative humidity and temperature measurements of the environment close to the packer face. The packer, located 50 cm outward from the heater, allowed steam to enter the center pipe, condense, and flow out to the borehole collar. The borehole sloped 5 degrees downward to the collar so as to facilitate drainage of condensed moisture toward the collar. A Tee-joint at the collar separated the heater power leads and thermocouple extension wires from the moisture line. From the Tee-joint, a 25-mm (1-in.) copper pipe took the moisture down the Rock Mechanics Incline to a 203-mm (8-in.) diameter, stainless steel water collection tank fitted with an electronic liquid-level sensor. The tank, shown in Fig. 4-2, had a capacity of about 50 L (13 gal).

The liquid-level sensor was a linear displacement transducer based on the movement of a strain pulse resulting from the interaction of magnetic fields emanating from the gage head and the float. Sensor performance parameters include an accuracy of 0.05 mm (0.002 in.) and a repeatability of 0.001% of full scale. In volumetric terms, these values correspond to an accuracy of 1.6 mL and a repeatability of 0.5 mL. The electronics box was hermetically sealed for protection from dust and moisture. Calibration of the water volume collected in the tank versus the voltage output of the liquid-level sensor was performed in the laboratory prior to field application. A field calibration check was done immediately following tank installation, and then repeated after completion of the test. The data acquisition system (DAS) recorded output voltage and calculated water volumes using the calibration curve.

Results

Figure 4-3 presents the moisture volume collected as a function of heating time. Essentially, no water was collected during the first 16 days of heating. Thereafter, the collection rate quickly increased, and collection continued until the volume leveled off at 6.1 L, following about 110 days of heating. The power ramp down started after 128 days. Figure 4-4 shows the variation of moisture collection rate with time. The collection rate shows a peak of 0.11 L/day at day 48, followed by a nonuniform decrease, returning to 0 at day 110.

The reasons for the changes in moisture collection rate observed in Fig. 4-4 are unclear, however, an attempt is made to explain the observations. The initial 16-day heating period before water collection started was probably the time required to initiate substantial boiling in the rock immediately around the borehole wall and, subsequently, build up vapor pressures in the rock matrix. Once enough water was vaporized and higher pressures built up in the matrix, vapor pressure gradients caused a vapor flux into the fractures and the borehole. The gradients also drove vapor radially outward from the borehole axis. The rapid increase in collection rate after day 16 was probably caused by the high rate of vaporization as pore water close to the borehole wall was heated to the boiling point and driven into the borehole. The scale of this boiling around the borehole wall probably increased as heat was supplied, leading to the peak

collection rate at day 48. As heating continued, the boiling front advanced into the rock and the radius of the dried out zone increased. A larger dried out zone meant less vapor was available for migration into the borehole and, consequently, the collection rate decreased. After 110 days of heating, the volume of rock above the boiling point of water was essentially dried out, therefore, the vapor flux into the borehole returned to zero.

The peak moisture collection rate of 0.11 L/day is significantly less than the 0.5 L/day value predicted by scoping calculations. Three possible reasons are suggested to explain this discrepancy. First, an infinitely long heater was assumed in the scoping calculations. This assumption omitted heater end effects, which might have been significant in the experiment, possibly causing a substantial overestimate of the steam flux into the borehole. The second possible reason for the lower observed collection rate involves condensation of steam before entering the packer center pipe. In Fig. 4-5, the dew point at the center pipe inlet and the temperature on the packer aluminum plate adjacent to the inlet are plotted versus heating time. The dew point was calculated from temperature and relative humidity measurements made by the relative humidity sensor at the inlet. Packer temperatures were measured by a thermocouple fitted to the aluminum end plate of the packer hardware. After the first four days of heating, the packer temperature remained below the dew point, suggesting that substantial steam condensation might have occurred at the packer surface. Such condensation could have caused some ponding below the entry point and subsequent water losses into fractures or into the rock matrix. The third possible reason for the discrepancy is the selection of too high an initial rock moisture content for use in the scoping calculations.

Recommendations for Future Work

Future field investigations to determine water migration into a heater borehole should attempt to measure water volumes without water removal from the borehole. A collection system like the one used in this test should not be considered, because it alters the heat flow, temperature distribution, and water migration characteristics in the rock around the borehole. The focus of a future design should be to select or develop instrumentation to measure volumes of water entering the borehole, with minimum interference to the hydrothermal behavior of the system.

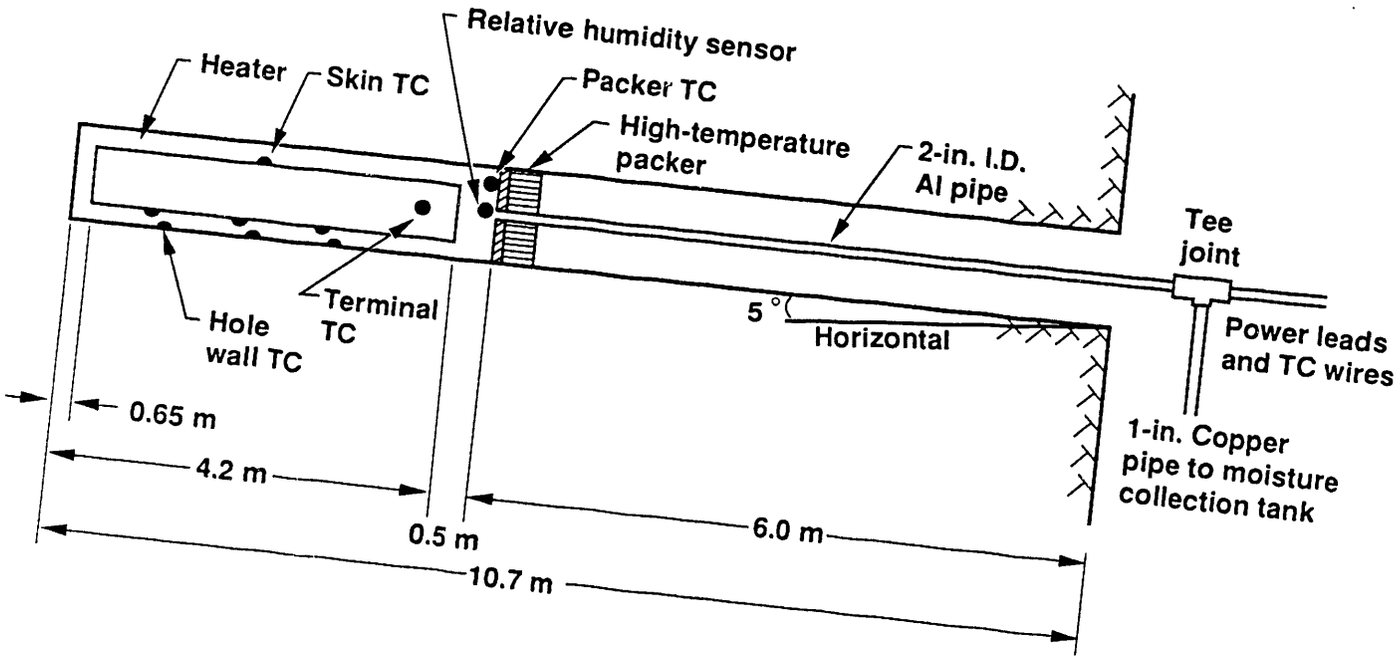

Figure 4-1. Schematic of vertical section through moisture collection system in the heater emplacement borehole.

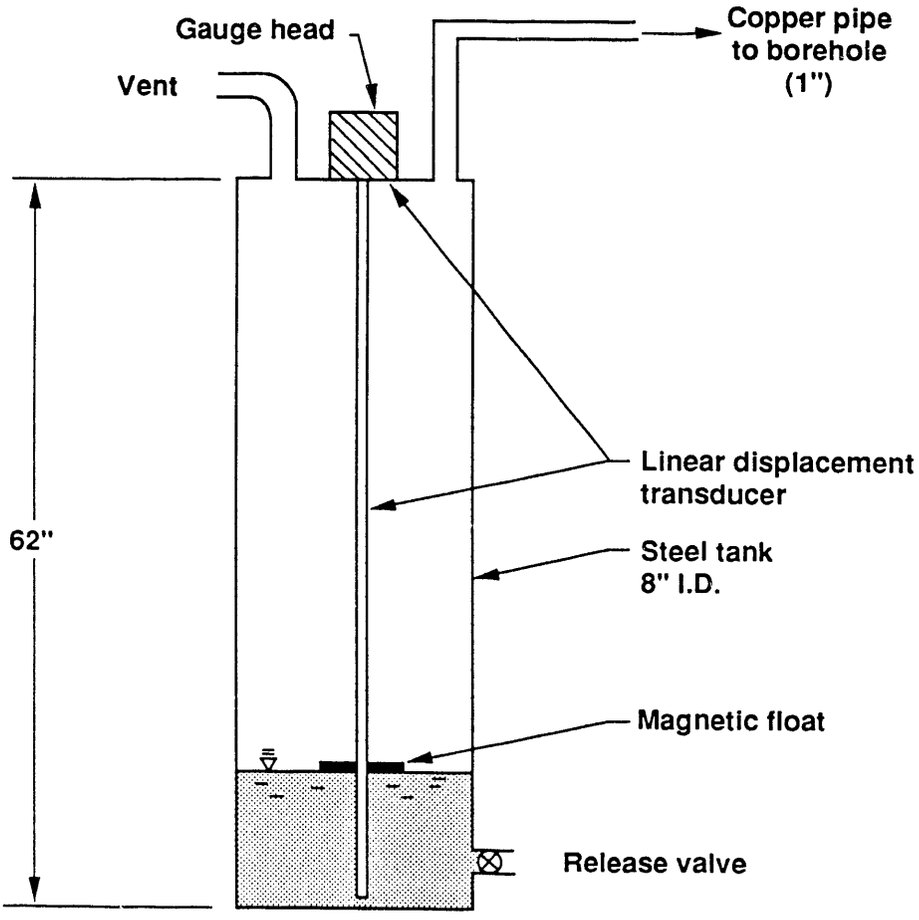

Figure 4-2. Moisture collection tank containing a liquid-level sensor.

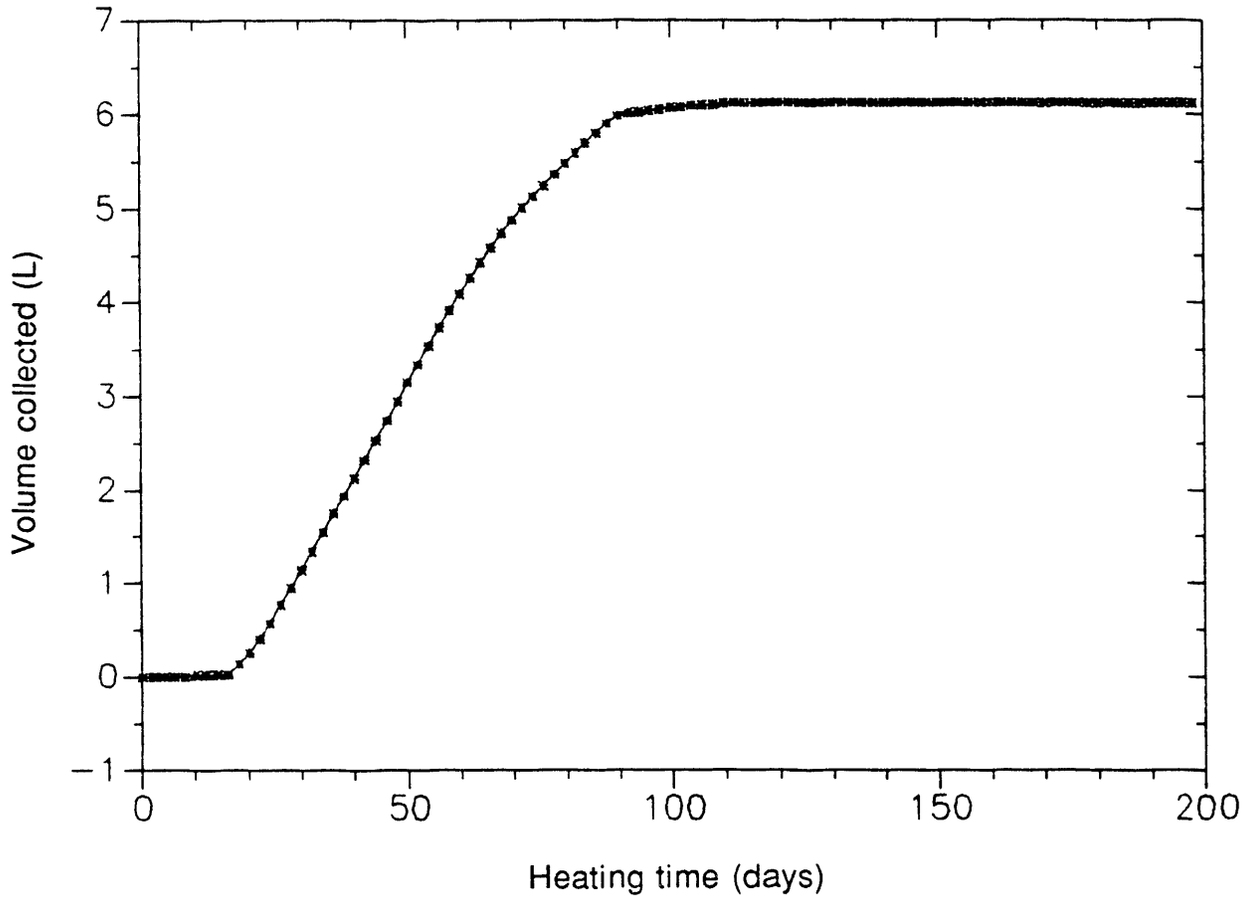

Figure 4-3. Moisture volume collected versus heating time.

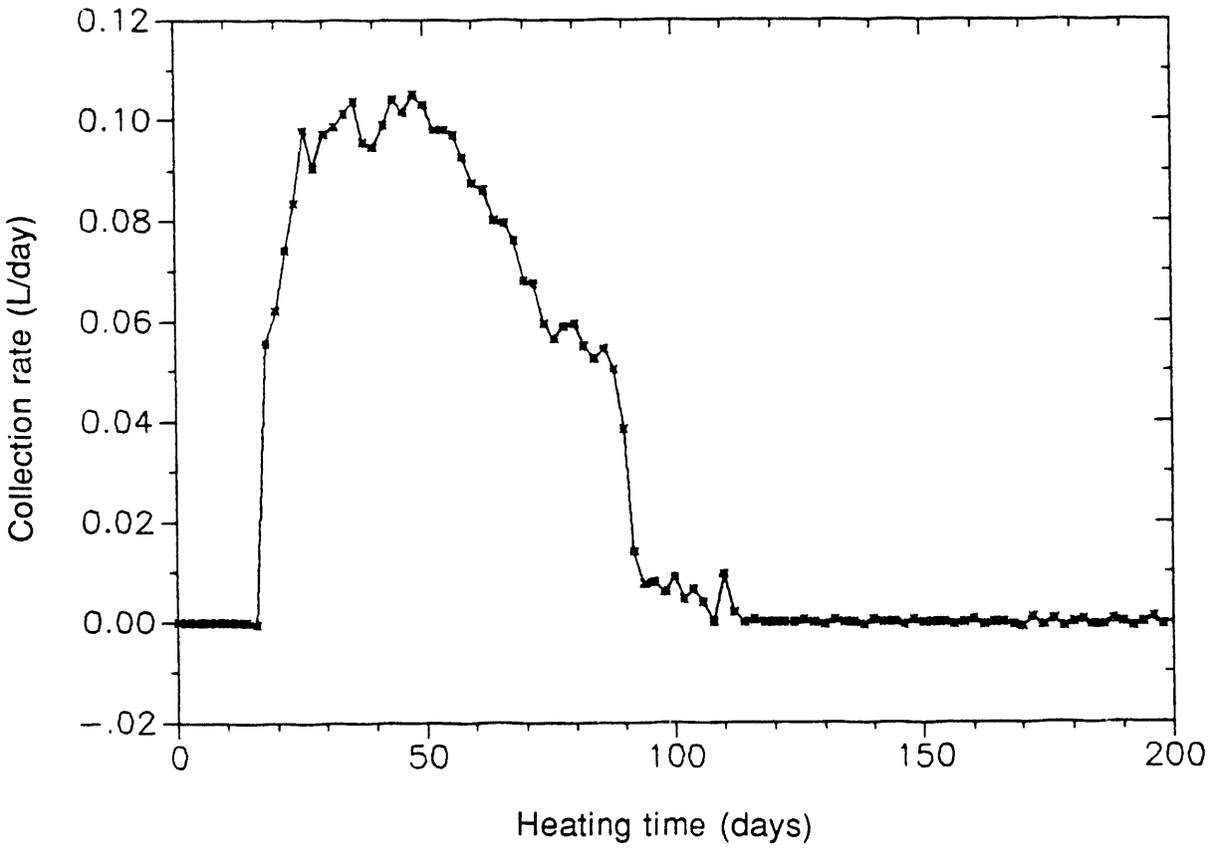

Figure 4-4. Moisture collection rate versus heating time.

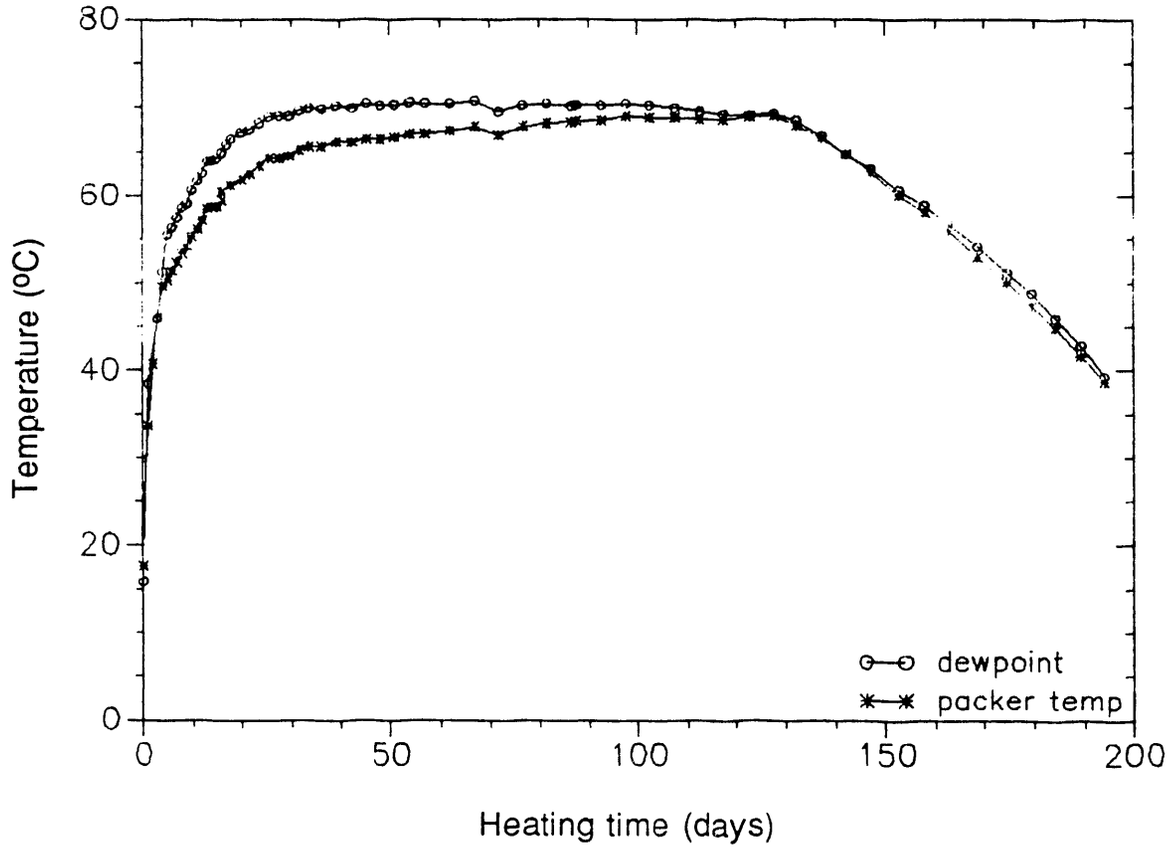

Figure 4-5. Dew point at center pipe inlet compared with temperature on adjacent packer plate.

Chapter 5

Water Potential Measurements with Thermocouple Psychrometers

Nai-hsien Mao and Herbert Wang

Relative humidity is an important hydrological parameter affecting waste package performance. In this chapter, we describe the development of a thermocouple psychrometer (TCP) instrument to measure this key variable. The TCP acts as a wet-dry bulb instrument, based on the Peltier effect, and it works with a relative humidity greater than 94%. For drier conditions, other sensors are needed. Therefore, we also used a capacitance sensor to measure the capacitance change due to relative humidity change. The operation range of the capacitance sensor was from 0 to 100% relative humidity up to 160°C (320°F). This chapter is a summary of a report on the same subject by Mao and Wang (1990).

A psychrometer has two thermocouple junctions. The copper-constantan junction serves as the reference temperature junction, and the constantan-chromel junction is the sensing junction. Current passes through the thermocouple causing cooling of the sensing junction by the Peltier effect for a predetermined duration (cooling time). When the temperature of the junction is below the dew point, water from the air will condense on the junction. As water condenses, it will heat the TCP slightly. This will be followed by cooling resulting from evaporation which is the temperature of interest. As the temperature of the thermocouple returns to ambient temperature, the Peltier current is discontinued and the thermocouple output is recorded . The temperature changes rapidly toward the ambient temperature until it reaches the wet bulb depression temperature. At this point, water evaporation from the junction produces a cooling effect on the junction that offsets the heat absorbed from the ambient surroundings. This continues until the water is depleted and the thermocouple temperature returns to the ambient temperature (Briscoe, 1984).

Three parameters are measured from a psychrometer: (1) the reference temperature, (2) the zero offset, and (3) a series of TCP outputs. The zero offset is the microvolts difference between the reference and sensing junctions before cooling. The magnitude of the effect is an indication of the degree of temperature equilibrium near the TCP. The data logger begins to record data roughly at the wet bulb depression temperature.

The water potential (WP) of a system defines the amount of work required to move an infinitesimal quantity of water reversibly and isothermally from a pool of pure water to that system and at the same elevation. Relative humidity measurements relate to the WP (Lang, 1967) by

$$WP = (1000\, RT / W_A) \ln(p/p_0), \qquad (5\text{-}1)$$

where:

- R = the universal gas constant [8.3143 J/(K mole)],
- T = the temperature (K),
- W_A = the molecular weight of water (18.016), and
- p/p_0 = ratio of the relative vapor pressure of water in equilibrium with the system to the vapor pressure over a flat surface of water; 100 (p/p_0) is the relative humidity.

The osmotic coefficient (∅) is defined (Lang, 1967) as

$$\varnothing = -1000 \ln(p/p_0)/(nmW_A), \tag{5-2}$$

where n is the number of ions per molecule of the salt, and m is the molality. Thus,

$$WP = -nRTm\varnothing. \tag{5-3}$$

Since osmolality (Ω) relates to ∅ by

$$\Omega = nm\varnothing, \tag{5-4}$$

we have WP directly related to osmolality as

$$WP = -RT\Omega. \tag{5-5}$$

Thus, for a salt solution of a known osmolality its WPs can be calculated as a function of temperature.

Calibration of the TCP

Interpretation of TCP measurements is based on calibration. Therefore, laboratory calibration of the individual TCP under controlled conditions is indispensable. This calibration must be carried out for the entire system, which includes Wescor stainless-steel cage TCPs (PST-55), a Campbell data logger (CR7X) with a psychrometer interface, and related software to record all data on floppy discs using an IBM PC. Calibrations were done at temperatures ranging from room temperature to 80°C (176°F), using standard sodium chloride (NaCl) solutions with osmolality from 100 to 1000 mmol/kg. The range of calibration conditions correspond to a relative humidity range of 98.15 to 99.8% at 20°C (68°F). A change in relative humidity of 1% is equivalent to a WP change of about 1.4 MPa (14 bar). The calibration procedures follow those described by Brown and Bartos (1982).

All calibrations were conducted under thermal and vapor equilibrium conditions. A typical set of calibration results is shown in Fig. 5-1, where voltage output from a TCP with different solutions at the same temperature [40°C (104°F) in this case] is plotted as a function of successive data points with a time interval of about 60 ms. Figure 5-2 shows the effect of temperature on TCP output for different solutions. Figure 5-3 shows the effect of solution strength on TCP output for different temperatures. For a given solution under a specific temperature, the TCP output can then be correlated with the WPs of the same solution and temperature.

Water potentials of NaCl solutions from 0 to 40°C (32 to 104°F) were reported by Lang (1967), and the TCP responses within this temperature range were measured by Brown and Bartos (1982), who proposed an empirical calibration model for TCP. The model correlates the WP of NaCl solutions with cooling time, temperature, TCP output, and TCP zero offset. A correction coefficient must be determined when applied to calibration data for other TCPs. We extended the model to a higher temperature to accommodate our data and found that the WP calculated from solution osmolality (Eq. 5-5) is not a simple constant ratio to that calculated from the model (WP_c), as proposed by Brown and Bartos (1982), but a function of both temperature (t in °C) and WP_c. The relationship between the WP (Eq. 5-5) and the WP_c empirically determined from our data is:

$$WP = 1.76 - 0.037t + 0.824WP_c + 0.007tWP_c \quad (5\text{-}6)$$

where the WP_c is calculated from the Brown and Bartos model using our calibration data. Figure 5-4 is a scatter plot between the WP calculated from Eq. (5-5) and those from Eq. (5-6) for all the calibration data. The agreement is very good for the entire range of WPs and temperatures. Once the coefficients are determined, Eq. (5-6) will also be used to calculate the WP from field data.

Clarke and Glew (1985) compiled and interpolated the osmotic coefficient for NaCl solutions for molality from 0 to saturation and temperature from 0 to 110°C. Using their data and Eq. (5-3), we can calculate the WP of NaCl solutions to a much larger range of molality and temperature.

Field Setup

Ten TCPs were installed in three boreholes (P1, P2, and P3). One additional TCP (Channel 4) was sealed inside a test tube filled with NaCl solution of osmolality 1000 mmol/kg. The test tube was placed inside a Thermos to keep the temperature constant. Channel 4 served as a reference channel to check the performance of the data logger. All TCPs were installed near the end of the hole. In the case of P1 and P2, three TCPs were installed in the sensor pockets of a rubber sleeve outside an inflatable packer (Fig. 5-4). By inflating the packer, the individual TCP is isolated from the environment but exposed to the borehole wall. This arrangement ensures local measurement and reduces the effect of fracture systems near the measurements. The packer also blocked the grout from invading the measurement area. In addition, another TCP was installed in front of the packer in P2 (Channel 11). For P3, three TCPs were bundled together in an aluminum housing backed by foam to prevent the grout from getting into the housing.

Table 5-1 shows the locations of each TCP. The locations of these holes with respect to the heater hole are shown in Fig. 8 in the Introduction of this report.

Table 5-1. Locations of TCPs.

Channel	Serial Number	Hole	Mode[a]
1	29751	P1	HT packer
2	29763	P1	HT packer
3	29771	P1	HT packer
4	29772	Inst. room	Thermos
5	29760	P3	Foam
6	29769	P3	Foam
7	29759	P3	Foam
8	29764	P2	LT packer
9	29773	P2	LT packer
10	29768	P2	LT packer
11	29756	P2	LT packer

[a]HT is high temperature; LT is low temperature.

A capacitance sensor was installed in the heater hole in front of the packer. The output of the capacitance sensor was configured to be voltages, which were factory-calibrated to be linearly proportional to both temperature and relative humidity.

All TCPs were installed on July 27, 1988, and the holes were grouted on July 28, 1988. The capacitance sensor was installed on August 24, 1988. The heater was turned on at 11:28 a.m. on September 7, 1988. Data were taken every 30 minutes starting July 27, 1988. However, the sensing junction of Channel 11 was bad from the very beginning; this channel only provides temperature data. A leak occurred in the pressure system outside the hole on October 12, 1988 (day 35 since heater was energized). Both packers were deflated and inflated again after the leak was fixed. Some channels went bad at that time (e.g., Channels 1, 2, and 8). All channels in P1 and P2 were affected by the leak as glitches in the output. On November 28, 1988 (day 82), the low-temperature packer failed. On January 13, 1989 (day 128), the heater power was ramped down. On May 15, 1989 (day 250), the heater was removed from the hole. Thus, the capacitance sensor measurements were terminated.

Results

The data plotted in Figs. 5-6 through 5-10 are from 8:33 a.m. on September 7, 1988 to 8:33 a.m. on July 4, 1989. The x-axis is in days since the heater was energized. These figures are composite plots of TCP data from all TCPs after a 10-point moving window smooth. The short-dashed lines are data from P1, the long-dashed lines are data from P2, and the solid lines are data from P3. The dotted line represents the data from the reference channel.

All TCPs were calibrated under isothermal conditions. However, the heater-test data indicated that the field condition was never isothermal. The temperature increased with time monotonically (Fig. 5-6). The highest temperature was about 84°C (183°F). The zero offset increased with temperature (in an algebraic sense). Data shown in Fig. 5-7 can be grouped by holes. Data from P1 (short-dashed lines) have a large negative offset, and data from P2 (long-dashed lines) have a large positive offset. Data from P3 (solid lines) have a small offset. A –60 microvolt offset indicates the sensing junction is 1°C (1.8°F) warmer, and a +60 microvolt offset indicates the sensing junction is 1°C colder than the reference junction (Brown and Bartos, 1982). All the psychrometers were installed with the sensing junction toward the bottom of the hole and the reference junction a few millimeters behind it. The TCPs in hole P1 were at the left side of the heater hole (see Fig. 8 in the Introduction). Therefore, the sensing junctions of the psychrometers should be warmer than the reference junctions and, consequently, negative zero offset values are expected. On the other hand, for psychrometers in holes P2 and P3, positive zero offset values are expected. The measured offsets are consistent with the locations (Fig. 5-7). The effects of the nonzero offset on the calculated WP had to be corrected. We used Brown and Bartos' model and Eq. (5-6) to correct the temperature and offset effects on the calculated WP from the field data. The TCP microvolt output is shown in Fig. 5-8, the corresponding relative humidity is shown in Fig. 5-9, and the calculated WP is shown in Fig. 5-10. The initial relative humidity was approximately 99.5%, corresponding to –5 bar WP. This was much wetter than we previously thought. Two prominent broad peaks of the calculated WP stand out at around day 140 and day 175. The first peak was in P3, which was below the heater and to the right. The second peak was in P2, which was above the heater and to the right. These data represented a drying and rewetting cycle with a delay of 35 days.

The TCPs in P2 were near NE6 at d = 5.86 m and d = 6.16 m, and the TCPs in P3 were near NE2A at d = 5.89 m. Figure 5-11 shows the change in moisture content as a function of time from the neutron measurements at these locations. Neutron data at locations below the heater (solid triangle) showed drying earlier than that above the heater (open square and diamond). However, neutron data were measured every 3 to 4 weeks. Consequently, they did not have the

same time resolution of TCP data that were measured every 30 minutes. These observed features can be explained by the gravity effect as described in Chapter 2 on neutron measurements. As temperatures increased, the evaporation rate of pore water increased. In unfractured rock, the gas phase flow was primarily outward. Water condensed above the heater would drain back to keep the boiling region wet, while water condensed below the heater would drain away from the boiling region. This conceptual model explained both the time and magnitude differences for data above and below the heater.

The temperature and relative humidity from the capacitance sensor in the heater hole are plotted in Figs. 5-12 and 5-13. The temperature increases monotonically to about 80°C (176°F), and the relative humidity decreases slowly to about 55%.

Conclusions

The TCP experiment in the heater test in G-Tunnel was the first attempt to use the TCP in such a hostile environment. Since the primary goal of the TCP experiment was to find out whether the combination of laboratory calibration and field use of TCPs can provide some useful data, we only selected three isolated locations for the test. Consequently, we cannot tell the whole story of the heater test based solely on TCP data. Yet, results from TCP measurement provide some information to the initial moisture condition and support some features shown by neutron measurements. This kind of consistent but redundant evidence makes the measurements of the heater test more credible. In summary, we note the following:

1. The TCPs were successfully calibrated in the laboratory up to 80°C.
2. A scheme was successfully established to calculate the WP based on laboratory calibration data, field data, and a modified Brown and Bartos model.
3. The packer sleeve arrangement for field setup of the TCP was fine if the type of packer (low or high temperature) was used appropriately.
4. The initial condition in the rock from TCP measurement was about 99.5% relative humidity or -5 bar WP. This indicated that the borehole wall was nearly saturated, much wetter than our initial estimate.
5. Two drying peaks were found at day 140 and day 175 in P3 (below the heater) and P2 (above the heater) that were qualitatively consistent with neutron data nearby. These features demonstrated that the gravity effects on moisture movement during the heater test were very important.
6. Large zero offsets were measured almost in every case due to nonisothermal conditions. Yet, the sign of the zero offset can be explained by the location of the TCP relative to the heater.

From these results, we conclude that the TCP is a very useful instrument for monitoring the change of moisture condition in the field. It can measure minute changes, within the operation limits, that no other known instrument can. However, because of the high sensitivity of the TCP to many environmental changes, proper field installation of the TCP is extremely important. Additional investigation is needed to optimize the installation procedure.

Future Work

Future work should emphasize a means to eliminate or control the nonisothermal effects on measurements. Since we did not do any post-test calibrations, we cannot tell whether there was any long-term drift of the TCPs or any possible effects of TCP sensor-tip contamination during the heater test. Therefore, the long-term drift of the TCPs and the possible effects of TCP sensor-tip contamination during the heater test should also be investigated.

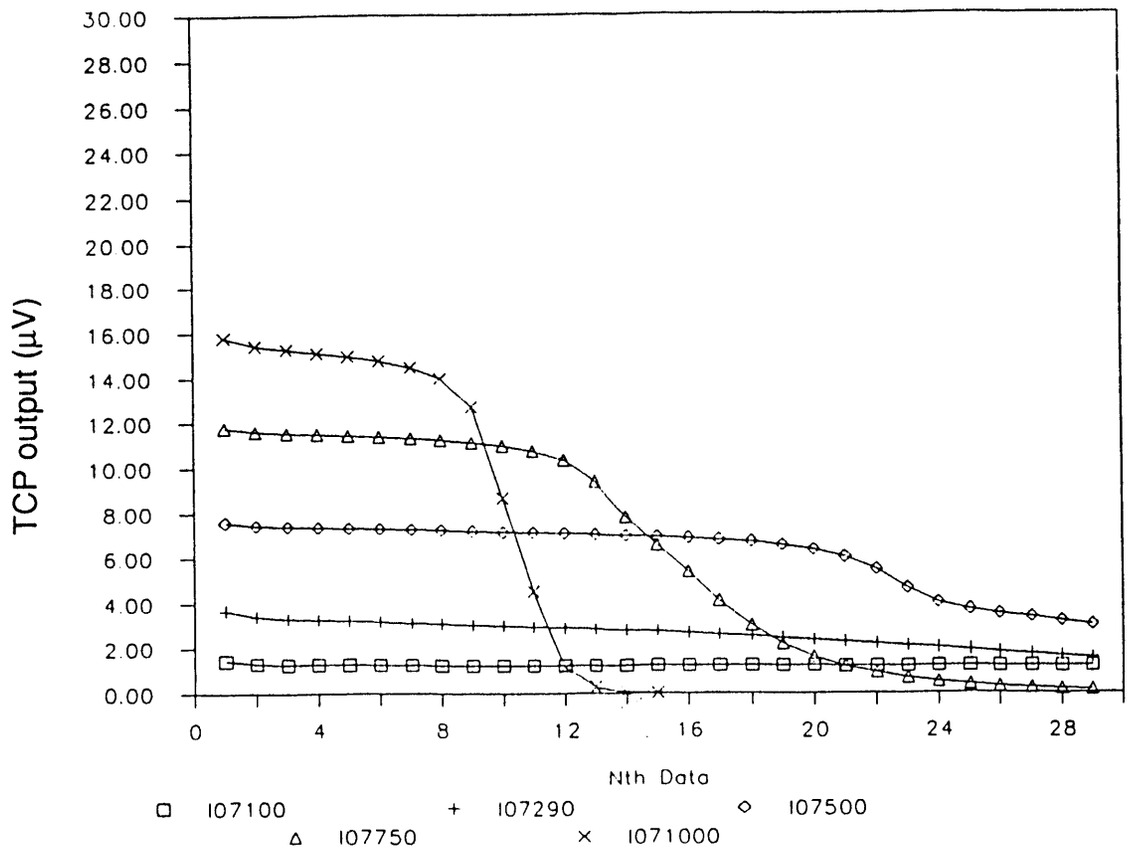

Figure 5-1. TCP output as a function of time for different NaCl solutions (approximately 60 ms between data points). The first three digits of the legend for each symbol are the TCP channel number; the remaining numbers indicate the osmolality of the NaCl solution in mmol/kg.

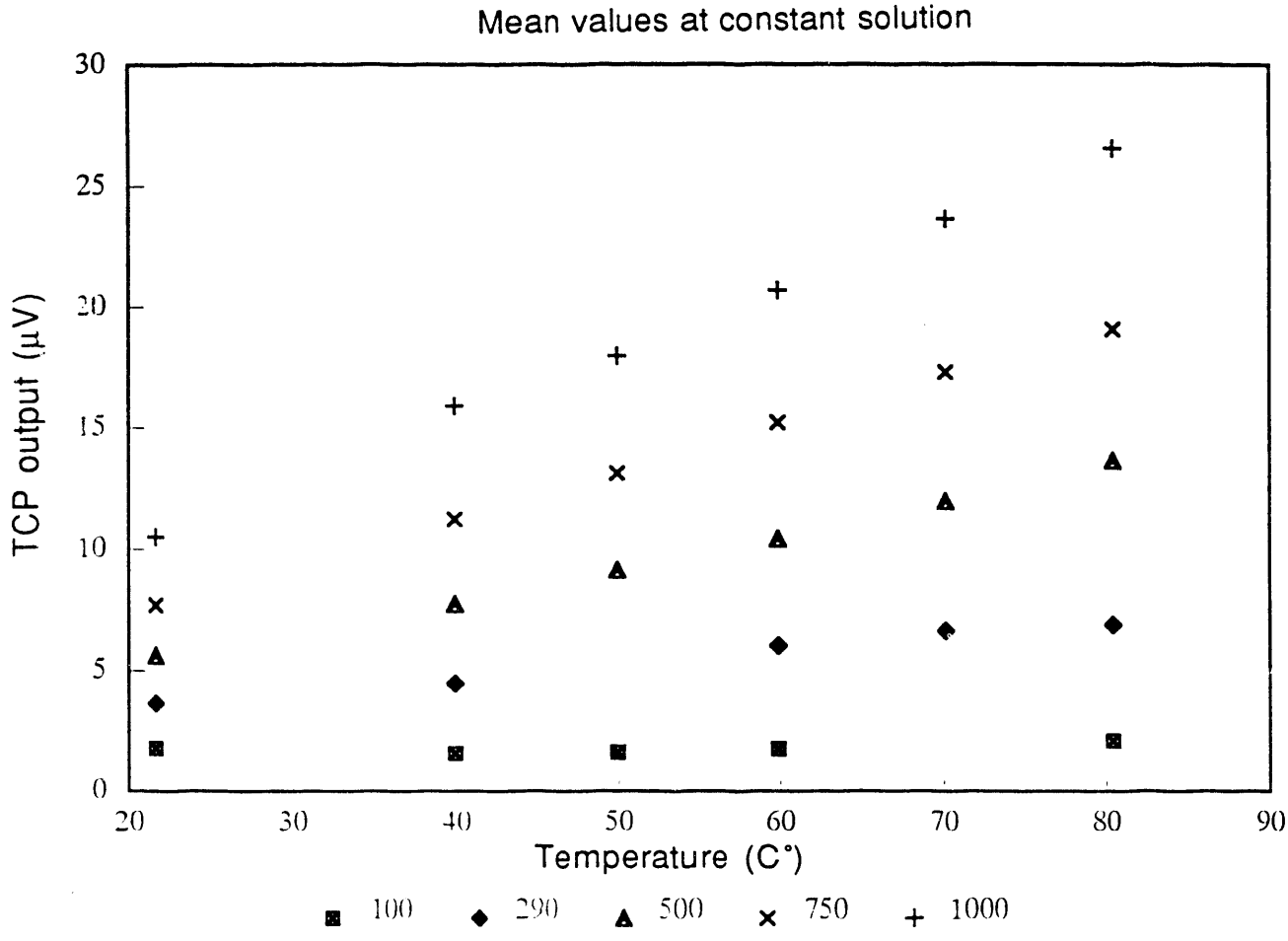

Figure 5-2. TCP output as a function of temperature at different NaCl solutions. The symbol legends are osmolality in mmol/kg.

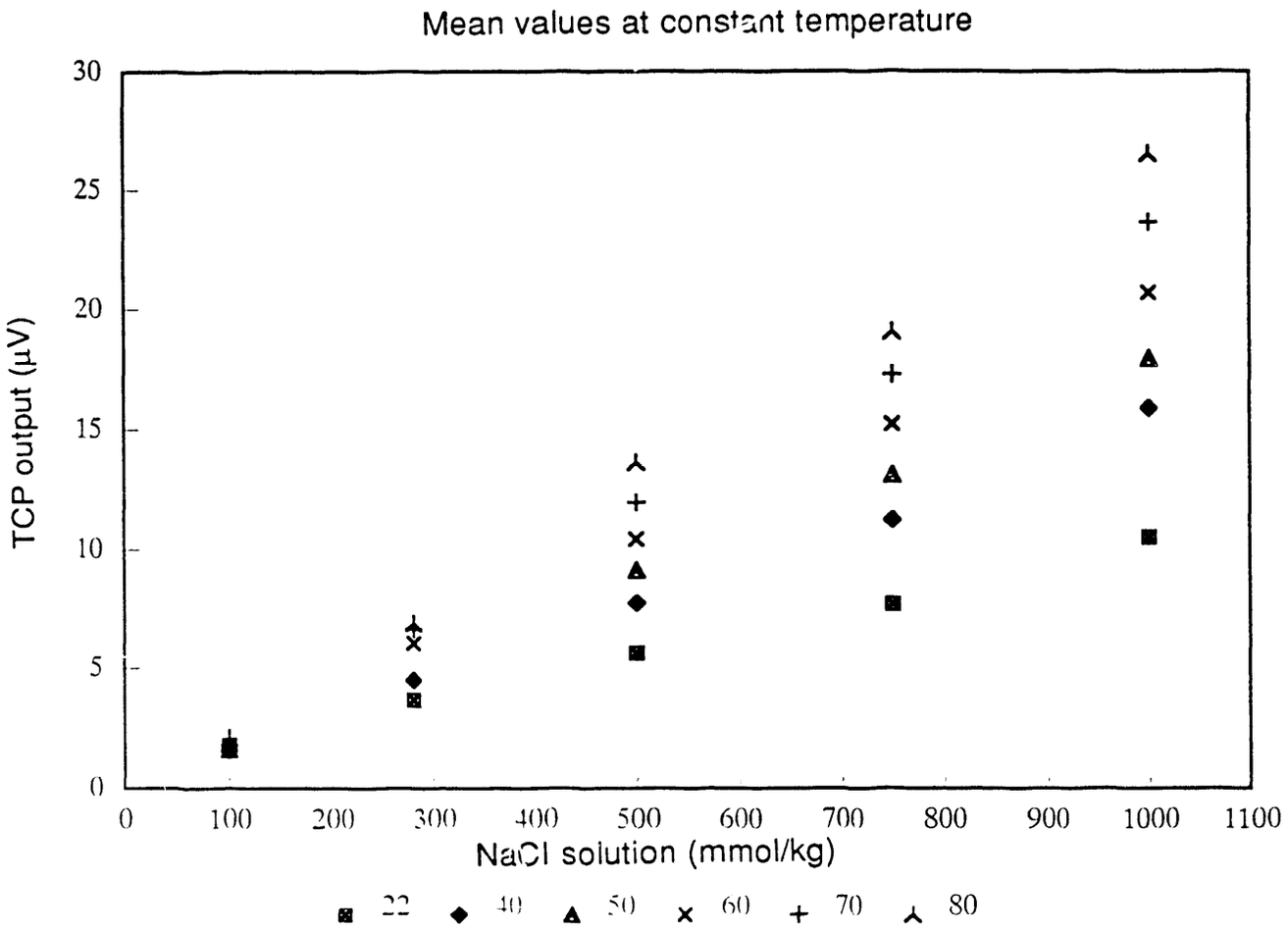

Figure 5-3. TCP output as a function of NaCl solution strength at different temperatures. The symbol legends are in °C.

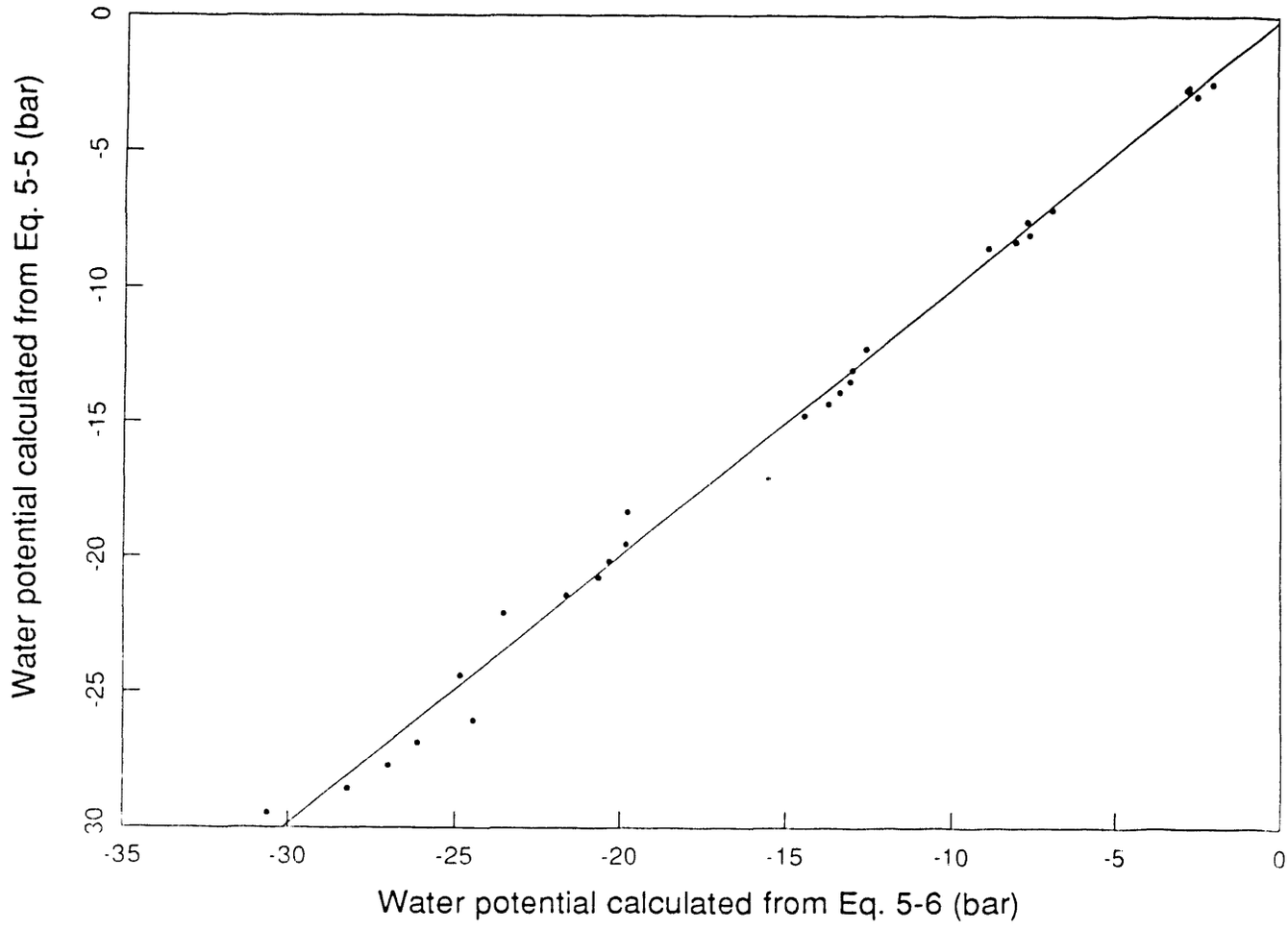

Figure 5-4. Scatter plot of water potentials calculated from Eqs. (5-5) and (5-6) for the laboratory TCP calibration data.

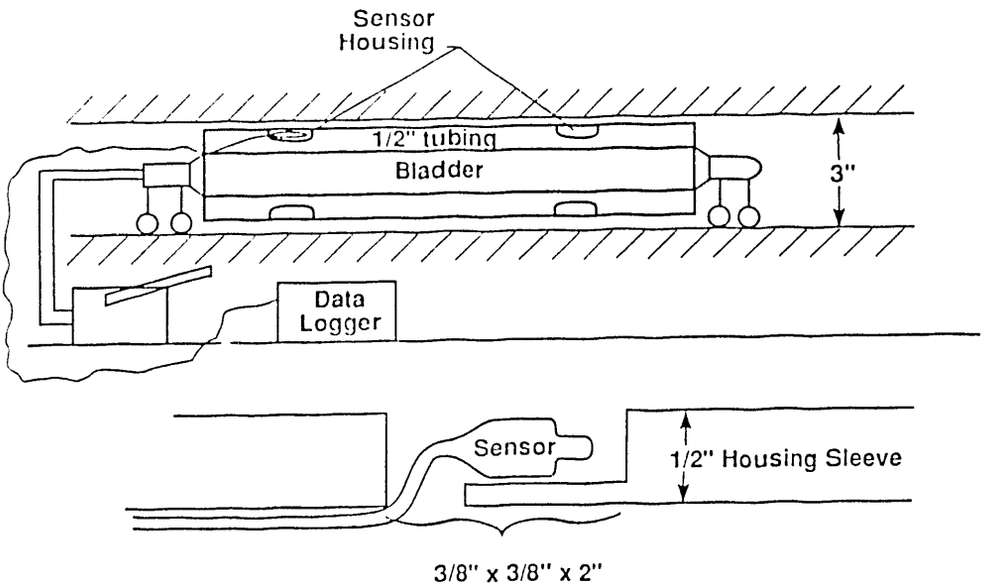

Figure 5-5. Packer sleeve assembly for the TCP.

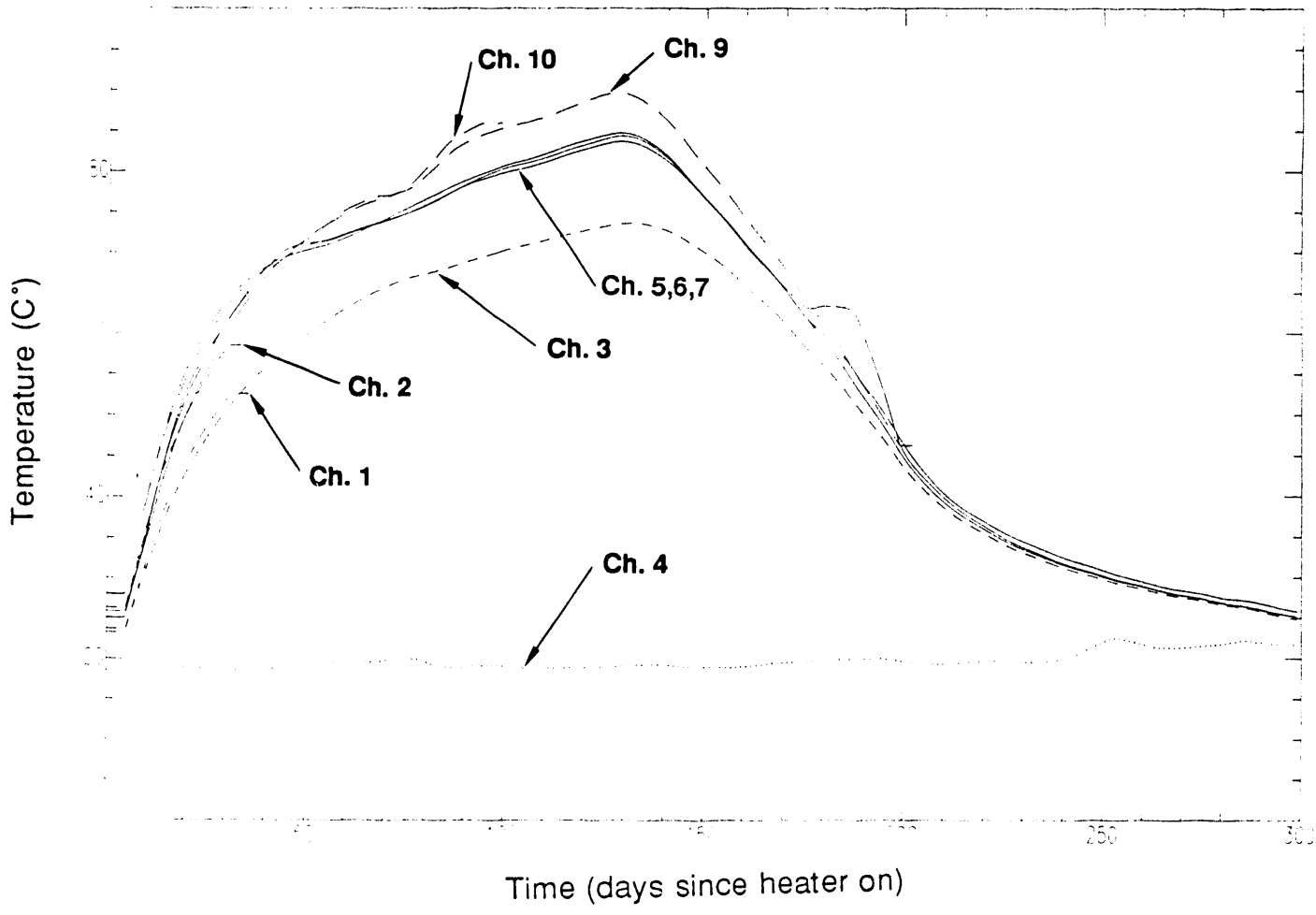

Figure 5-6. Temperature as a function of time for all TCPs of the heater test in G-Tunnel. Short dashed lines are data from hole P1; long dashed lines are data from P2; solid lines are data from P3; and the dotted line is for the reference channel.

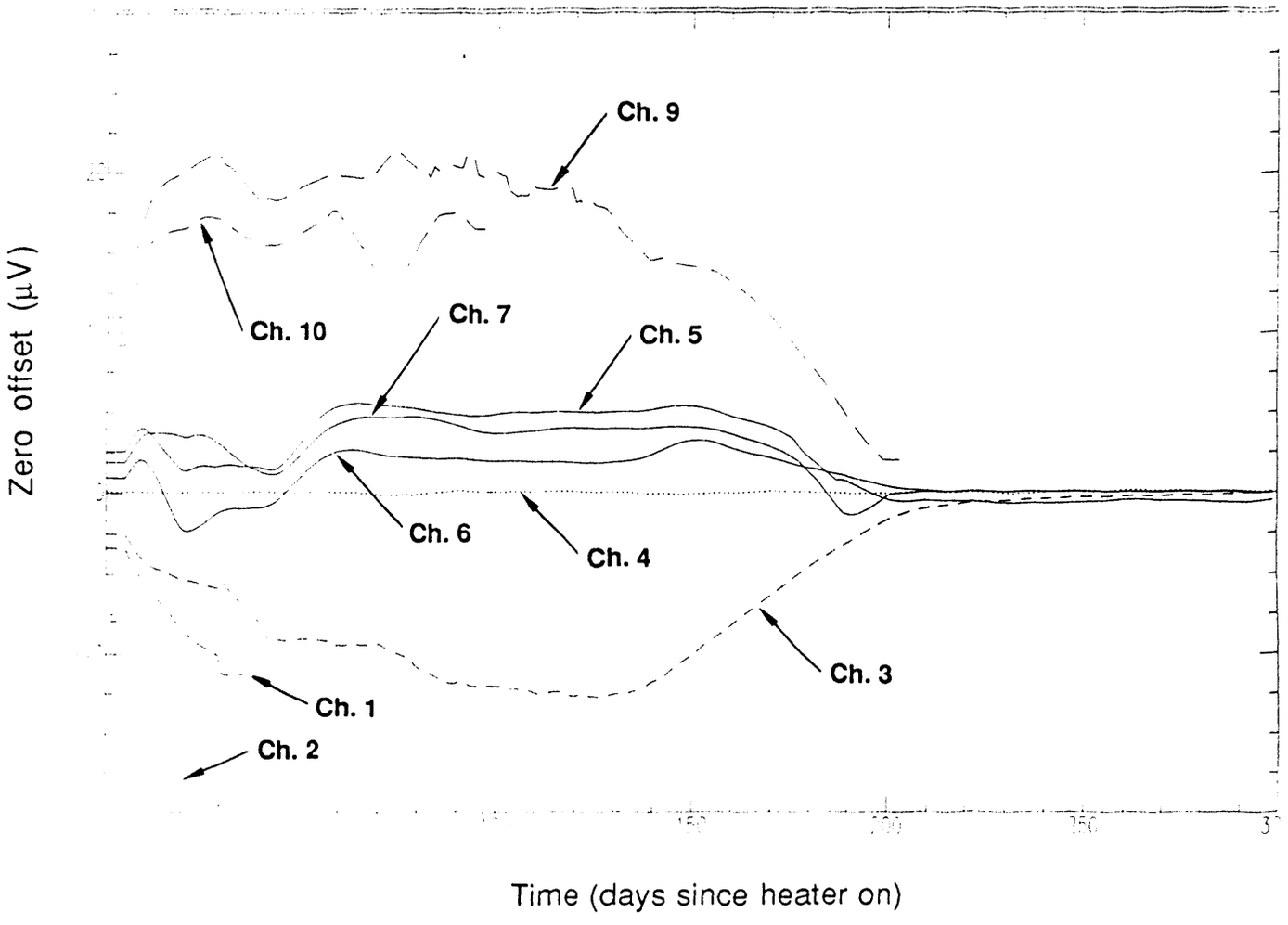

Figure 5-7. TCP zero offset as a function of time for all TCPs of the heater test in G-Tunnel. See caption of Fig. 5-6 for the legend.

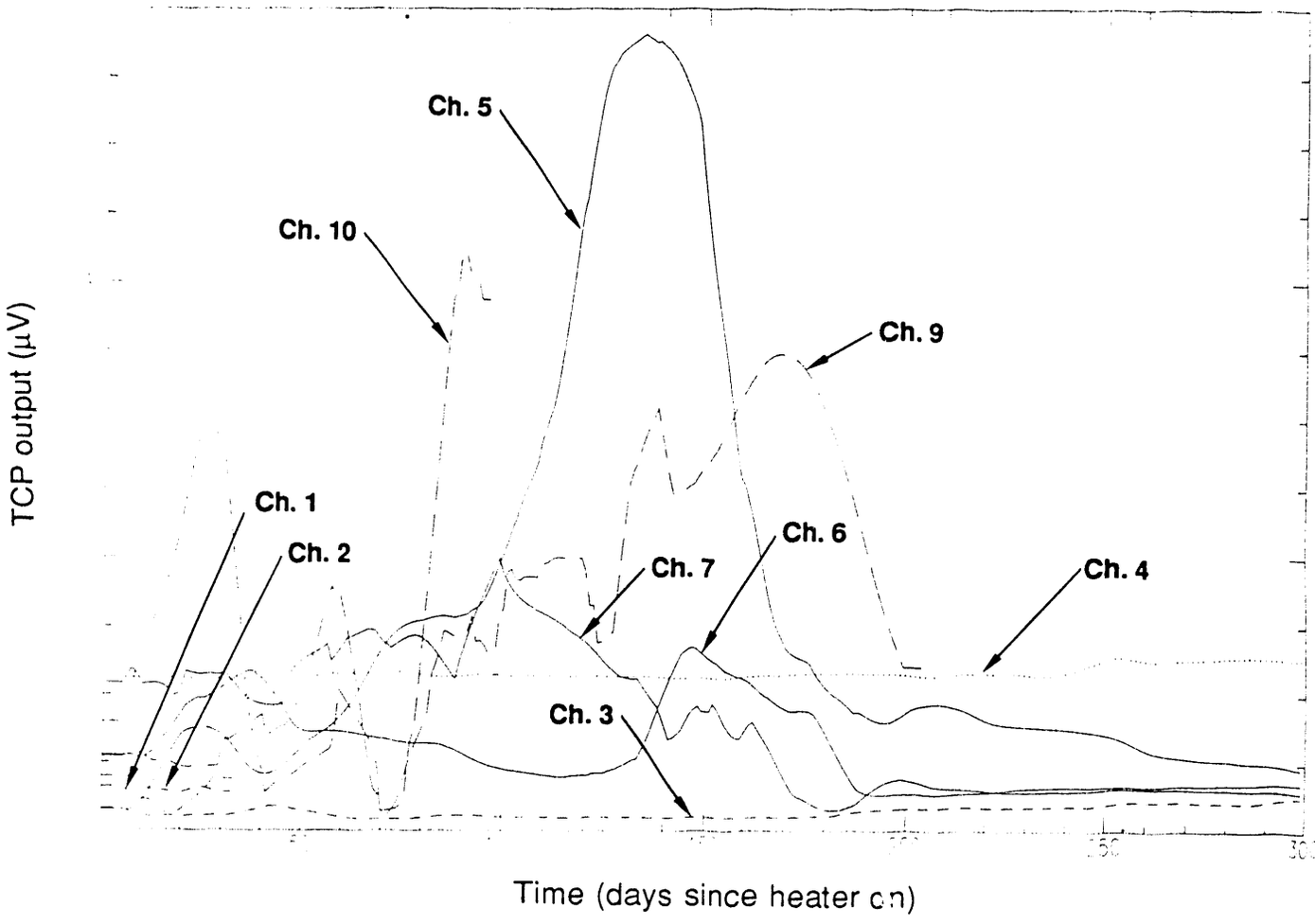

Figure 5-8. TCP microvoltage output as a function of time for all TCPs of the heater test in G-Tunnel. See caption of Fig. 5-6 for the legend.

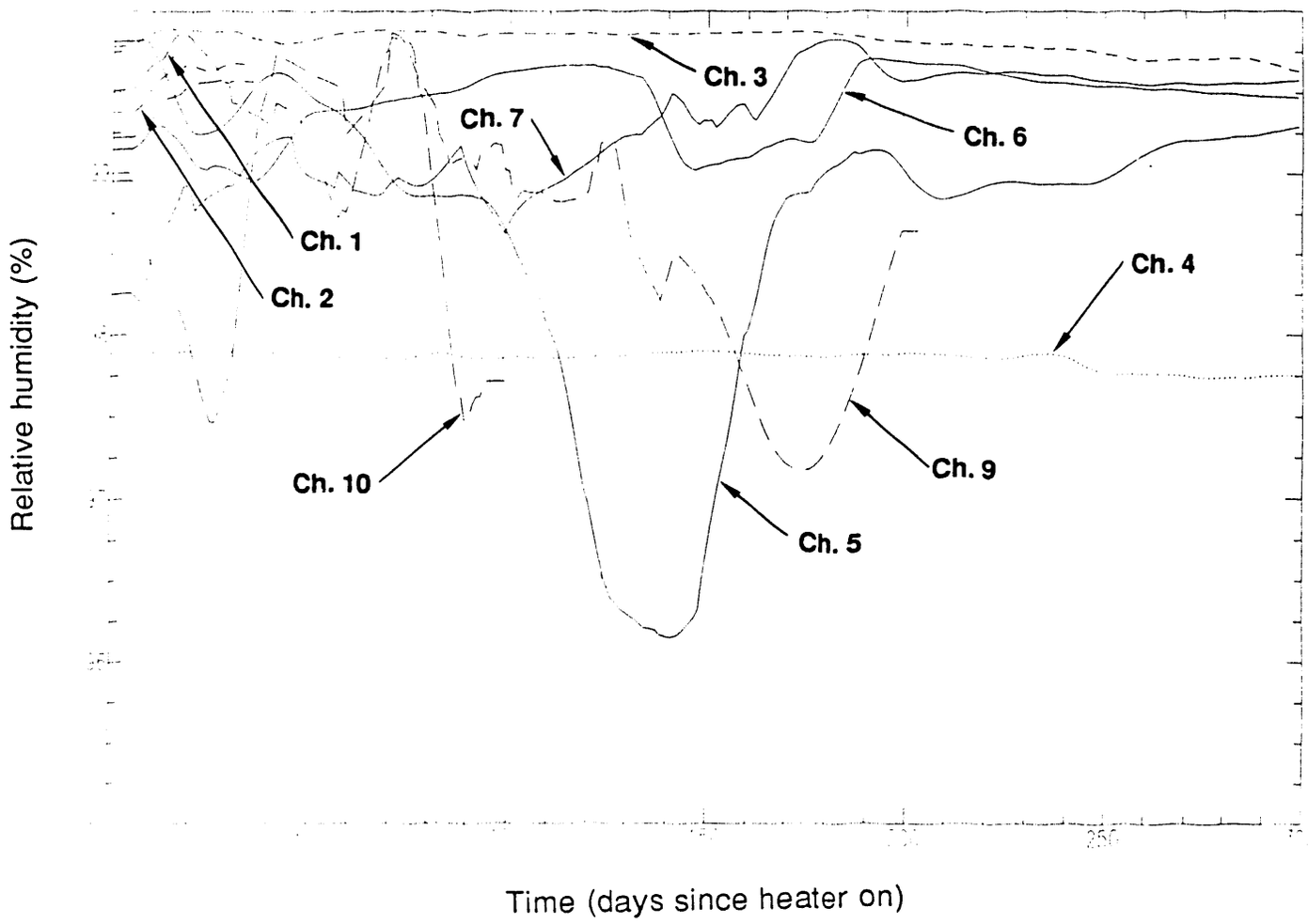

Figure 5-9. Calculated relative humidity as a function of time for all TCPs of the heater test in G-Tunnel. See caption of Fig. 5-6 for the legend.

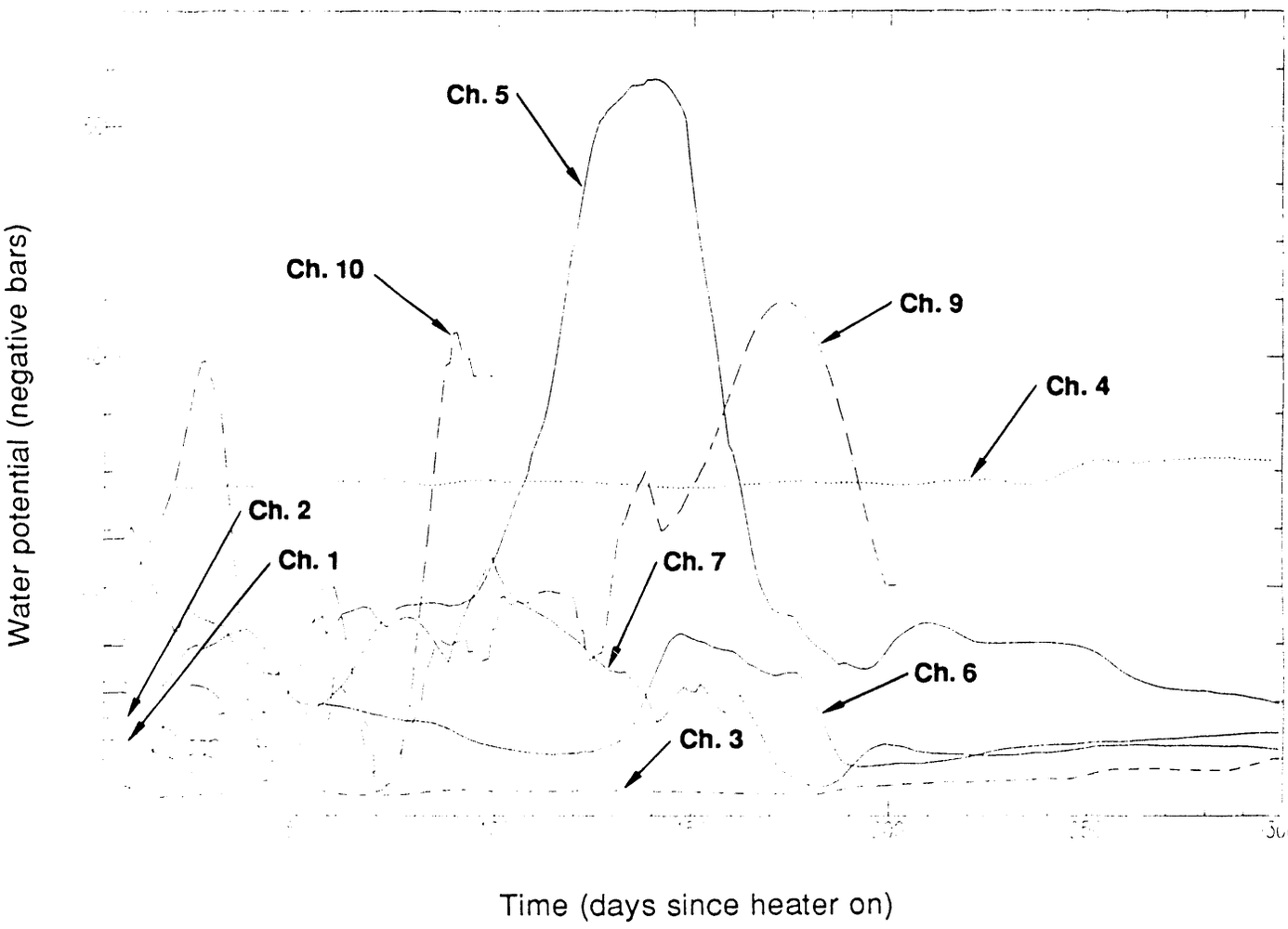

Figure 5-10. Calculated water potential as a function of time for all TCPs of the heater test in G-Tunnel. See caption of Fig. 5-6 for the legend.

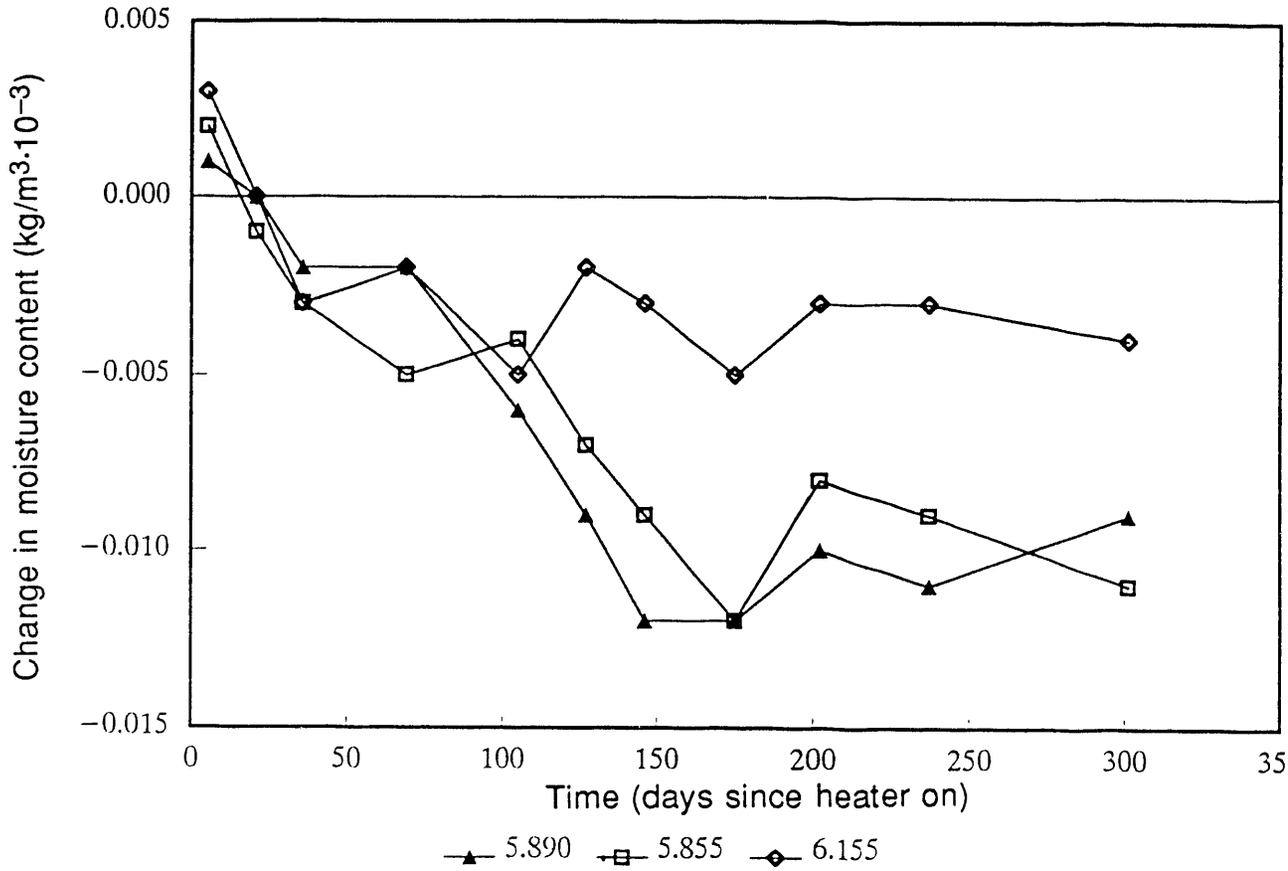

Figure 5-11. Change of moisture as a function of time for locations near the TCPs as determined from thermal neutron measurements.

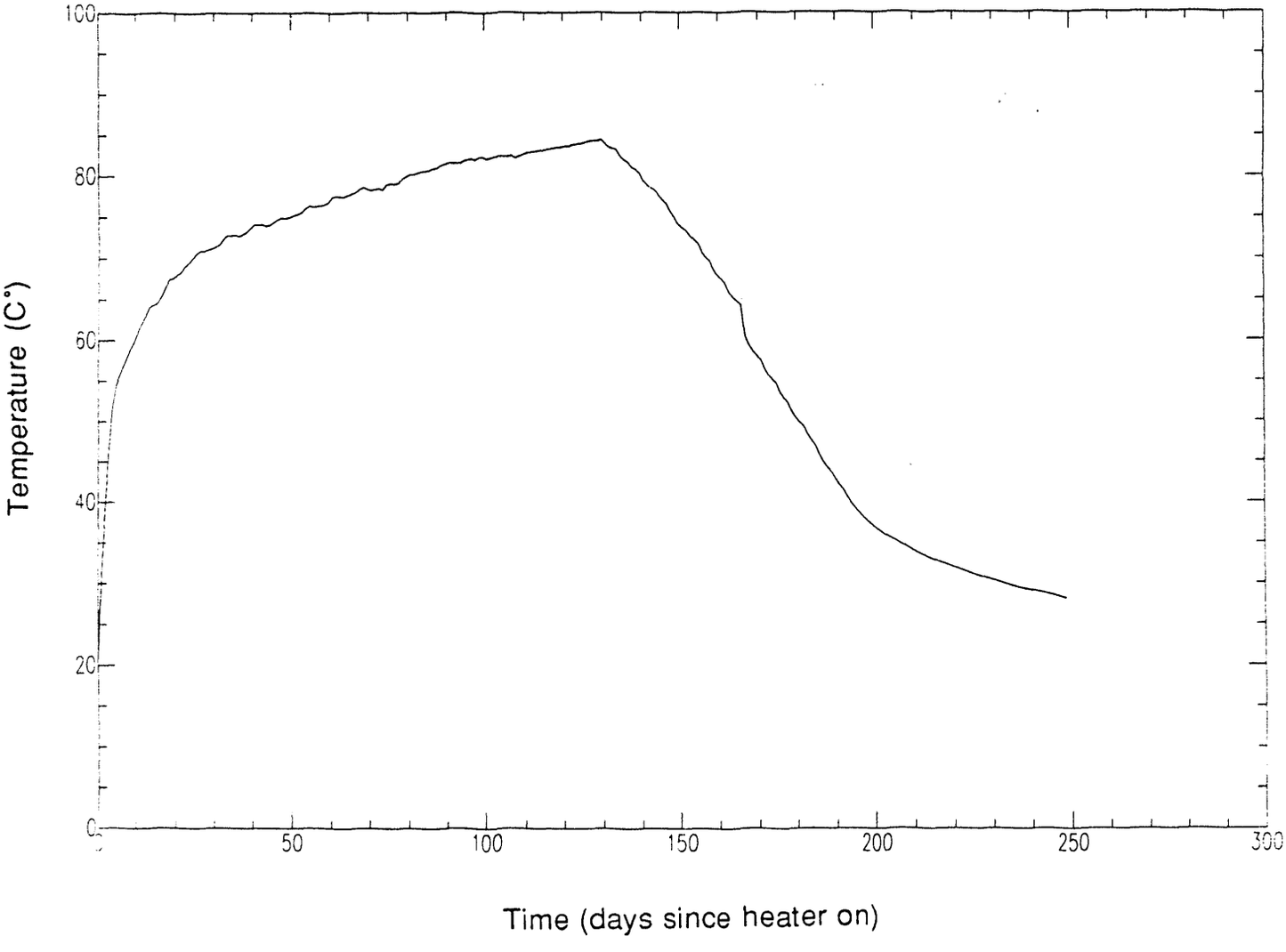

Figure 5-12. Measured temperature from capacitance sensor in the heater hole.

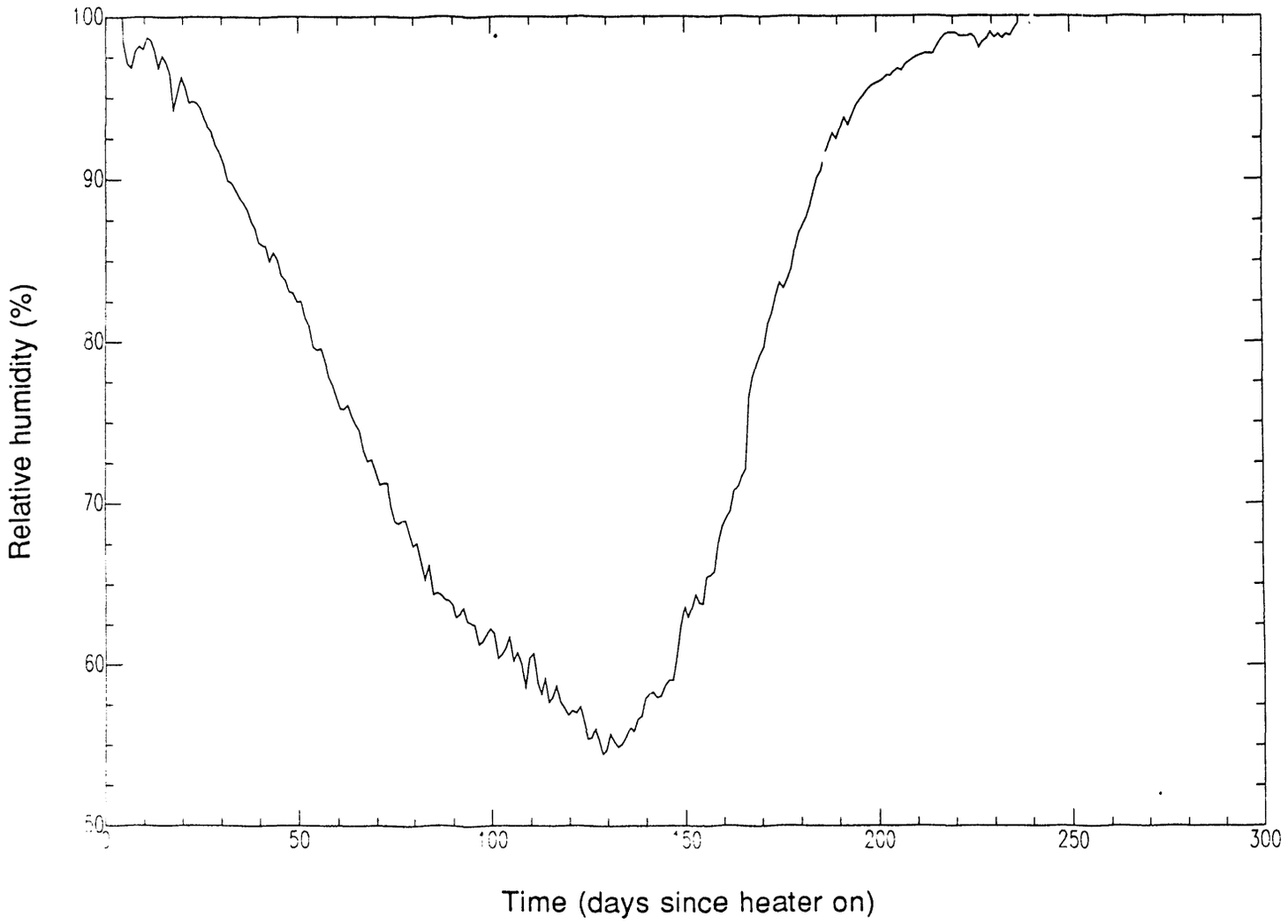

Figure 5-13. Measured relative humidity from capacitance sensor in the heater hole.

Chapter 6

Pressure Measurements

Wunan Lin

Transport of water in an unsaturated medium, such as the proposed study site at Yucca Mountain, Nevada, will very likely be two-phase: vapor (or steam) and liquid water. Therefore, determination of partial vapor pressure in the medium is desired for a model study of the transport mechanism. In the prototype test in G-Tunnel, we measured the relative humidity and moisture content of the rock around the heater. To determine the partial vapor pressure in the rock, we also determined the total pressure in the medium. Gas pressures are also needed to understand the flow of the gaseous phase. For that purpose, we decided to measure the pore-gas (including steam or vapor) pressure in the boreholes where relative humidity was determined (P1, P2, and P3). The total pore-air pressure was measured using a strain-gage pressure transducer. Other purposes of this test were to investigate both the capabilities of the pressure measuring technique and the long-term stability of sensitive pressure transducers. We also measured the barometric pressure in the alcove (outside the boreholes), where total pressure was measured.

Calibration of Pressure Transducers

We tried two typ pressure transducers in this test. The first was a piezoresistive-gage transducer, designed to measure fluid pressure at elevated temperatures. This type was not stable enough for our purpose. It was replaced by another piezoresistive-gage transducer for room temperature applications in mid-October 1988. The ambient pressure in the alcove was measured by a barometric pressure transducer, which was manufactured by Rosemount. All of our pressure transducers were calibrated by the Engineering Measurement and Analysis Section (EMAS), LLNL, using a Ruska 100-psi calibration system. The calibrations gave us the voltage output of the transducers at zero pressure (zero-offset) and the coefficient of voltage output versus applied pressure. Our data acquisition system (DAS) measures the voltage output of the transducers, subtracts the voltage with the zero-offset, then divides the net voltage by the coefficient to obtain absolute pressure of the measuring point.

Installation of Pressure Transducers

As mentioned previously, the pore-air pressure is measured in the psychrometer boreholes, P1, P2, and P3. To be able to reuse the transducers and to calibrate the transducers during the test, we decided to place the transducers outside of the boreholes and probe the pressure at the measuring point, which is in the vicinity of the psychrometer, by a stainless steel high-pressure tubing. In holes P1 and P2, due to the restriction of the psychrometer packer, a 1/8-in. high-pressure tubing was used. In P3, a 1/4-in. tubing was used.

In P1 and P2, the high-pressure tubing was embedded in the rubber sleeve of the psychrometer packer. The inner end of the tubing was open to the pressure port, which was pushed against the borehole wall as the packer was inflated. The pressure tubing and a portion of the borehole wall were sealed within the port by the rubber sleeve on the packer. One of the "sensor housings" in Fig. 5-5 was used as the pressure port. The pressure tubing was then grouted, along with the thermocouple bundle and psychrometer packer assembly, in the borehole. The outer end of the pressure tubing was connected to the pressure transducer. The connections were designed such that the transducers could be isolated from the pressure tubing so that in situ calibration and checks on the transducers could be performed. At the beginning of the test, we

connected one high-temperature pressure transducer and one room-temperature pressure transducer to P1, and one high-temperature pressure transducer to P2 and P3, so that the performance of these two types of transducers could be evaluated. About 43 days later, we decided to replace all of the high-temperature pressure transducers with the room-temperature transducers.

Results

Results of the pressure measurement in holes P1, P2, and P3 are shown in Figs. 6-1 through 6-3, respectively. The spikes on day 20 in Figs. 6-1 and 6-2 were due to an in situ pressure calibration. The spikes right after day 40 in these figures were due to the changing of pressure transducers. While pressure transducers were calibrated in the laboratory, field conditions were sufficiently different to cause spikes.

The pressure in P1 (Fig. 6-1), which was measured at about 0.8 m from the heater, built up quickly to a maximum of about 60 psi absolute on day 50 of heating. It then decreased to a minimum of about 38 psi on day 88 of heating. The short period of constant pressure between day 130 and day 137 was likely related to the beginning of the heater ramp-down since it coincided with the ramp-down; however, its cause is not known. But the pressure continued to increase and reached a maximum of 57 psi on day 170. This result is inconsistent with the current conceptual model of gas phase behavior near the heater. One possible explanation of the pressure variations during the heating phase and the heater ramp-down period is as follows. The packer has a metal mandrel and a tubing (see Fig. 5-5) and, therefore, conducts heat better than the rock mass. The gas in the port was warmed up faster than the rock mass nearby. The peak at day 50 was caused by the fast heating of the very small volume of gas in the port. The excess gas pressure in the port then leaked away causing the decrease between day 50 and day 100. The gas pressure in the port did not increase until the section of the borehole in front of the packer filled up with gas. Then both the pressures in the port and the borehole in front of the packer increased slowly between day 100 and day 170.

In P2, the pressure was measured at a distance of about 2 m from the center of the heater, at the two o'clock position (looking toward the bottom of the hole). Although the pressure history was not complete and the quality of the data was not very good, the pressure reached a value of about 14.5 psi within the first 80 days of heating. It is very likely that 14.5 psi was not the maximum pressure in P2. The big decrease in pressure in P2 on day 80 was associated with the packer failure. After that, no excess pressure was measured in P2.

The pressure measuring point in P3 was about 1 m from the center of the heater, at about the four o'clock position. The pressure increased gradually during the entire heating period. It reached a maximum of about 13.3 psi a few days after the heater ramp-down began. The pressure history in P3 can be explained by the thermal expansion of gas (including air, water vapor, and other gases) in the pores of an intact rock mass. The greater pressure measured in P2 than in P3 was probably because P2 was above the heater and P3 was below the heater. In a gravity-influenced system, gas has a stronger tendency to move upward. The rock above the heater is also hotter; this would lead to more thermal expansion. But probably the most important reason for P2 being greater than P3 is because it was sampling a much smaller volume of gas, therefore, causing a smaller time lag in pressure buildup. There is a difference in tubing volume (P3 was emplaced using a 1/4-in. tubing) that might also explain the more uniform response, however, the sampling volume difference is much greater than tubing volume differences. We judge that the sampling volume difference is the most likely factor.

The technique of measuring gas pressure remotely, using a pressure tubing to connect the pressure transducer and the measuring point, worked well. In future tests, we will select other strategic

locations for measuring both gas pressure and temperature. However, we have to find a better way of sealing the pressure port.

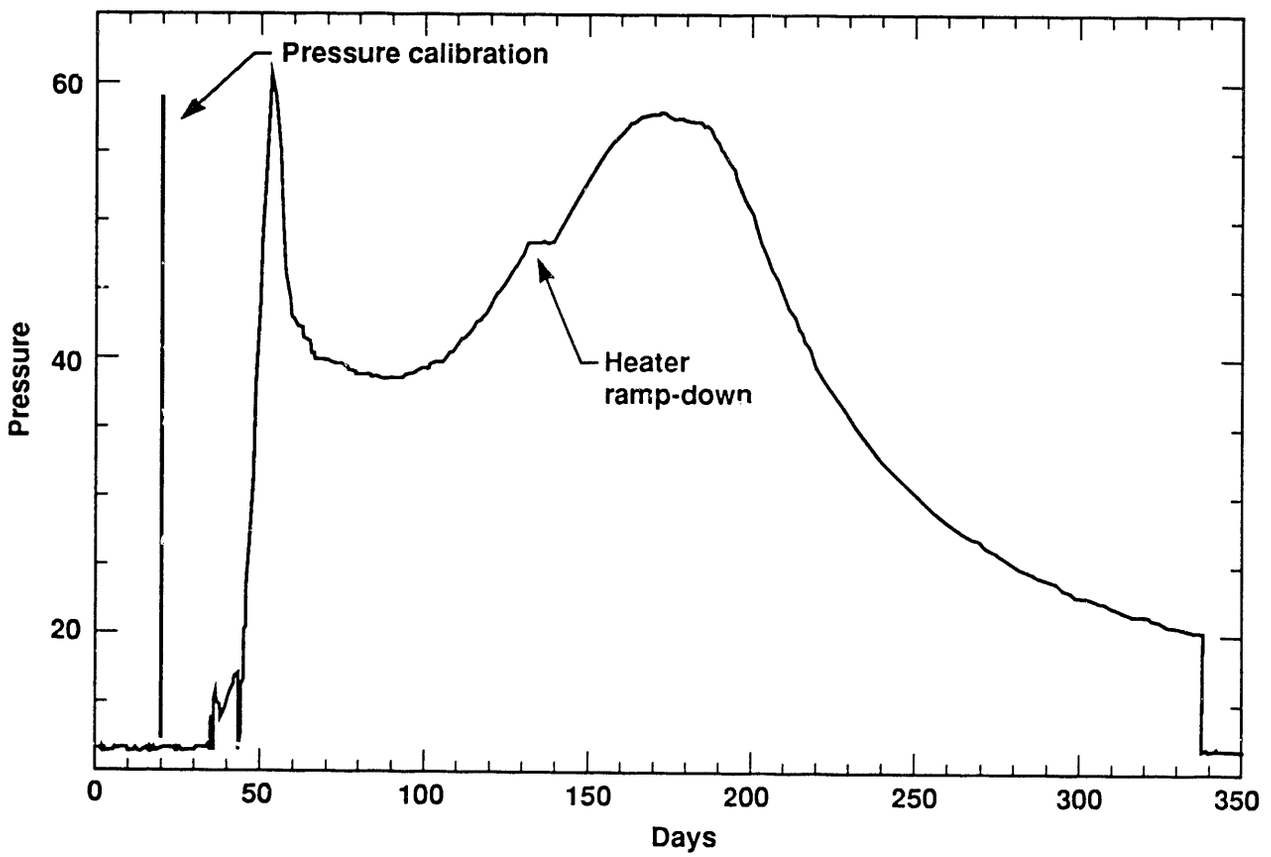

Figure 6-1. Pressure measurement in hole P1.

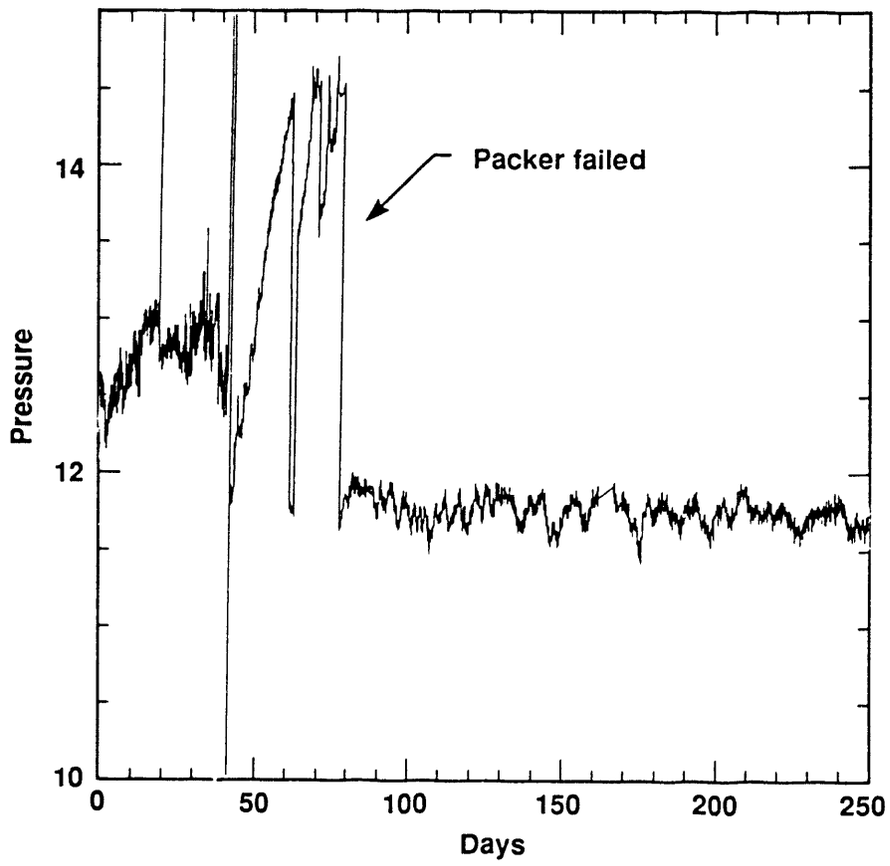

Figure 6-2. Pressure measurement in hole P2.

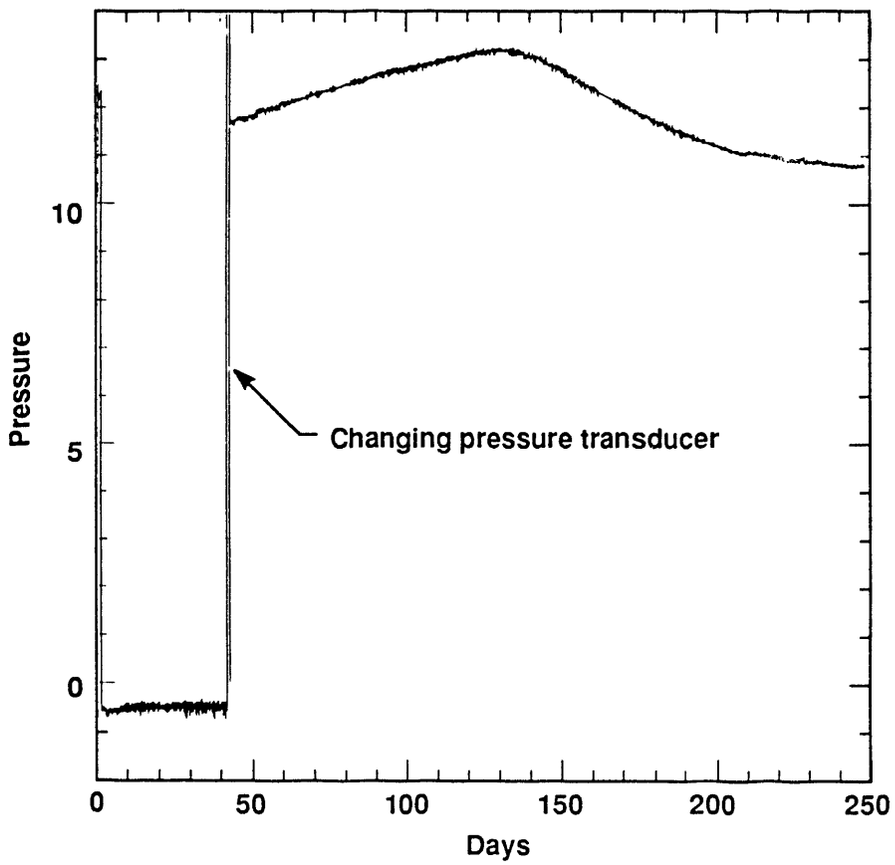

Figure 6-3. Pressure measurement in hole P3.

Chapter 7

Temperature Measurements

Wunan Lin, Abelardo Ramirez, and Donald Watwood

The purpose of the heater test was twofold: to test methods of measurement and instrumentation and to study the hydrothermal properties of the medium about the heater. The primary purpose of measuring temperature in this test was to understand the thermal response of the medium around the heater. Temperature is one of the primary variables measured in such a test. Temperature measurement techniques are well established. Thermocouples are usually very reliable. However, the installation of thermocouples requires further investigation. The thermocouples can be either grouted in-place in a borehole or installed in a retrievable configuration. The effect of each of these installation techniques on the accuracy of temperature measurement was investigated.

In this chapter, the calibration and installation of thermocouples are discussed. Some results of the temperature measurements are presented.

Calibration of Thermocouples

A total of 132 thermocouples were used in this test. All of these thermocouples were chromel-alumel (Type K), with stainless steel sheath. The thermocouple wires were grounded to the sheath at the sensing point. The outside diameter of the sheath was 0.16 cm. The thermocouples were calibrated using a Rosemount constant-temperature oil bath. Ten of the thermocouples were calibrated at temperatures of 0, 25, 100, 225, 249, 299, and 350°C (32, 77, 212, 437, 480, 570, and 662°F). The calibrations indicated that, at temperatures below 250°C (482°F), all the thermocouple readings were within 1°C (1.8°F) of the standard thermometer. At 250°C, 33 of these thermocouple readings differed from that of the standard thermometer by more than 1°C. Among those, only three thermocouple readings differed by more than 2°C (3.6°F) from the thermometer readings. During the installation of the thermocouples, the thermocouples with greater variance were installed in a cooler region where the temperature would probably not exceed 100°C (212°F). Therefore, the uncertainty of the temperature measurement will not exceed 1°C in this test.

Thermocouple Installation

The 10 thermocouples that were calibrated to 350°C were used in the heater hole (see Chapter 4, and Lee and Ueng, 1989, for the details). Twenty of the other thermocouples (none of which had a variance exceeding 1°C) were mounted into two Teflon brackets (10 in each bracket), with a 20-cm (7.9-in.) spacing between each thermocouple. These two strings of thermocouples were designed to be inserted into the NE holes (one in NE3, NE4, and NE5; the other in the remaining NE holes). The temperature measurements in the NE holes were used to help interpret the high frequency electromagnetic tomography.

The rest of the thermocouples (102 total) were installed in the thermocouple holes (TC1 and TC2) and the psychrometer holes (P1, P2, and P3). Figures 4 and 9 in the Introduction of this report show the locations of these holes relative to the heater hole. Figure 9 shows the distribution of thermocouples in the thermocouple holes and psychrometer holes. The thermocouples in each hole were bundled together with a spacing of either 20 cm (7.9 in.) or 30 cm (11.8 in.), depending on the distance from the heater; shorter spacing was used where the thermocouples were within 1.5 m (4.9 ft) of the heater. Because the decision to use

psychrometer packers was made after the thermocouple bundles had been completed, the thermocouple spacing in P1 and P2 holes was not consistent with the distance from the heater. Before installing a thermocouple bundle in a borehole, we bent each thermocouple so that its hot junction (the sensing tip) pointed away from the bundle. This should have decreased any effects of the bundle on the measured temperatures.

In TC2, P2, and P3 holes, a thin-walled stainless steel tubing [0.32-cm (0.13-in.) I.D. and 3.66-m (12-ft) length] was bound together with the outer portion of the thermocouple bundle. The last thermocouple in each bundle was put inside the tubing, to be used as a traveling thermocouple; this was to test the effect of the thin-walled tubing on the temperature measured from the thermocouple in it. To do that, the traveling thermocouple was moved to the same location as one of the thermocouples outside the tubing, and the temperature readings (within about 5 min) from the two were compared.

The thermocouple wires were connected to isothermal blocks outside of the boreholes. Special care was taken to make sure that the thermocouple polarity was correct. The temperature at the isothermal blocks was measured by resistance thermistor, which was calibrated in the same manner as were the thermocouples. The data acquisition system (DAS) calculates the absolute temperature at each measuring location using the thermocouple and the thermistor readings. After every thermocouple was checked, the holes (TC1, TC2, P1, P2, and P3) were grouted.

Test Procedures

The DAS started collecting baseline data 28 days before the heater was energized on September 7, 1988. A power of about 3.3 kW was applied to the heater on that date. The heater power was maintained at that level for 128 days (until January 13, 1989); then a power ramp-down began. As shown in Fig. 7-1, the ramp-down was accomplished in 20 steps over 67 days. During most of the test, the DAS took temperature readings every hour.

Results and Discussions

The Heater Source and Temperature Field

The temperatures on the heater container and the heater borehole are shown in Fig. 7-2 as a function of time. Thermocouples 105 and 107 were at the surface of the heater can, at the middle of the heater; thermocouple 107 was on the top and thermocouple 105 was at the bottom. Thermocouple 104 was on the borehole surface below the heater, near thermocouple 105. The temperature on the top of the horizontal heater can was about 30°C greater than that at the bottom of the heater. Based on our bench tests of the heater, this difference was an intrinsic characteristic of the heater assembly (probably caused by the convection of air in it), not caused by the surrounding rock mass. Because the difference existed from the beginning of heating, it is unlikely that the difference was caused by moisture-refluxing effects. The temperature variation on the heater can surface had some effect on the temperature distribution in the rock mass, as discussed below. The temperature distribution on our heater assembly was probably different than that of a real waste canister. The temperature on the bottom of the borehole wall (thermocouple 104) reached about 240°C, which is comparable to the maximum temperature expected from a true nuclear waste package.

Figure 7-3 shows the temperature contours of the thermal field in the test region on January 13, 1989, the last day of full-power heating. (The temperature contours were constructed from the T/C measurements using MacGRIDZO on an Apple Macintosh computer.) Also shown in Fig. 7-3 are the major fractures (short straight lines) in the boreholes. This temperature field

represents a combination of the temperatures in two vertical planes transverse to the middle of the heater, separated by about 0.5 m. Because the heater was 3-m long, the temperatures over a 0.5-m distance, near the midpoint, probably were not significantly different (see Fig. 4 in the Introduction). The heavy circle in Fig. 7-3 represents the heater hole. There were little temperature data within a 0.5-m radius of the heater; therefore, the contoured temperatures in that region cannot be well constrained. Otherwise, the contour map is a fair representation of the temperature distribution measured by the thermocouples. The isotherm plot is for qualitative interpretation only, due to the limited number of data points and their uneven spatial distribution. Generally, the isotherms, especially those greater than 80°C, elongate vertically upward with respect to the center of the heater hole. This phenomenon persisted throughout the heating and early cooling phases. Most of this asymmetrical temperature distribution can be attributed to the temperature variation on the heater surface, as mentioned earlier. In the future, we will require a uniform temperature on the heater surface, probably by minimizing air convection in the heater container. The slightly lower temperature toward the alcove was probably due to the heat dissipation in the alcove.

The Traveling Thermocouples

The temperatures measured by the traveling thermocouple in P3 are plotted with respect to time in Fig. 7-4. The line identified by "102" represents the temperatures measured by the traveling thermocouple. Also plotted in Fig. 7-4 are the readings of the stationary thermocouples ("94" through "99"), where the traveling thermocouple passed. The step decreases in temperature are caused by the traveling thermocouple being moved to the position of the next thermocouple at various locations during the test. The temperatures measured by a stationary thermocouple "96" are not shown in Fig. 7-4 because of a malfunction of that thermocouple. The temperature readings of the traveling thermocouple agree very well with those measured by the stationary thermocouples. A slight disagreement between "97" and "102" was probably due to a slight location mismatch of the two thermocouples. The difference, about 0.15°C, was well within the accuracy of the temperature measurement. This indicates that installing a thermocouple in thin-wall tubing did not impair the accuracy. The advantage of installing a thermocouple in thin-wall tubing is that the thermocouple can be removed for recalibration or replacement during a long duration test. The results from P2 and TC2 are similar to that in P3.

Comparison with the Scoping Calculation Model

The shape of a temperature-time plot of a thermocouple, as shown in Fig. 7-4, is very similar to those calculated by Montan (1986), who used a line-source conduction model with 5-kW heating for 13 weeks (91 days) and a ramp-down period of 24 weeks (168 days). Although magnitudes and amplitudes cannot be directly compared because of different power levels and times, the shape of the curve is dependent on the mechanisms for heat transfer. Since Montan used a similar declining power to the heater during ramp-down (similar number of steps), a comparison of curve shapes is justified. The similar shapes indicate that conduction was the primary heat transfer mechanism. Another way to analyze the data is to plot the temperature versus the radial distance from the heater. Generally speaking, the measured temperature versus radial distance plots agree well with the predictions of the V-TOUGH code (Buscheck and Nitao, 1991; Nitao, 1989), which coupled transport of water, vapor, air, and heat in fractured porous media. This suggests that transport of water, vapor, air, and heat in fractured media only caused secondary perturbation on the temperature in the rock mass (Fig. 7-5). It should be noted that continuing model evaluation work indicates that in comparison with fracture-matrix models equivalent continuum models tend to give slightly suppressed temperatures in the intermediate radial distances. This is consistent with the results shown in Fig. 7-5.

Effect of Fractures on Temperature

Figure 7-5 shows temperatures in P2 and P3 on January 13, 1989, as a function of radial distance from the center of the heater. The numbers in parentheses are the thermocouple identification numbers, as shown in Fig. 7-3. Within a radial distance of about 0.7 m, there are three thermocouples in P3 (82, 83, and 84) and one in P2 (58) that read cooler temperatures than would be expected from the trend of the temperatures of other thermocouples in these holes. This feature persisted through the heating and cooling phases whenever the maximum temperature in the borehole was greater than about 50°C (which was as early as September 12, 1988). Fracture mapping in these boreholes showed that there were fractures within close proximity of these thermocouples, as shown in Fig. 7-3.

Fractures can affect temperature in several ways:

1. Fractures provide a preferential pathway for drainage of the drilling and grouting water. The matrix around the fracture might have a chance to imbibe some of the water, making the initial moisture content of the rock greater relative to an unfractured region. Greater initial moisture content will make the region heat more slowly, due to a greater specific heat and thermal conductivity.

2. Fractures also provide a preferential pathway for vapor and steam to escape, thereby removing energy more effectively relative to an unfractured region. In addition, when boiling of water occurs, the temperature in a region with fractures will be lower than that in a region without fractures, due to a lower boiling point of water in fractures.

3. A region with higher initial moisture content will have more water available to maintain the boiling process; that will keep the temperature at a boiling point of water longer. Therefore, the temperature will be lower than in a region where the rock dries more quickly.

These effects of fractures on the temperature might have played roles of varying significance at different stages of the test. The water permeability of the intact tuff is very low (see Appendix A); therefore, the imbibition of drilling and grouting water into the matrix from the fractures was not significant, and the temperatures at these thermocouples (82, 83, 84, and 58) on January 13, 1989, were well above the boiling point of water. The second effect mentioned above (that is, the fracture provided a pathway for effective dissipation of energy) was more dominating, especially during the latter part of the heating phase. The effect of fractures became significant when the temperature was sufficiently high (above 50°C) to allow evaporation.

Boiling Process

Figure 7-5 also shows that between 0.7 and 1.2 m, the trend of the temperature data in P3 shows a flattening between 96 and 100° C. These temperatures (96 to 100°C) are about the boiling points of water in G-Tunnel (which depend on the air pressure). The model used in the scoping calculation predicted a similar discontinuity. However, the measured temperatures show a larger region associated with a flattened temperature trend. This phenomenon was only observed in P3, not in P2. If the flattening of the temperature-radius plot corresponds to the boiling of pore water (as suggested by the scoping calculations), P2 and P3 have different style of boiling. Based on the data we have analyzed, the boiling process in P3 began on or before November 26, 1988, when the flattening in the temperature-radius profile was just a simple offset, very similar to the model prediction; it ended before February 3, 1989, when the flattening disappeared.

Figure 7-6(a) shows the temperature history of the P3 thermocouples associated with the flattening in Fig. 7-5. The number on each curve represents the thermocouple identification number, as in Fig. 7-5. The striking feature in Fig. 7-6(a) is the difference between 88, 89, and 90 and others (86, 87, and 91). The temperature plateau in thermocouples 88 and 89 indicate active and prolonged boiling of the pore water. The sharp increase in temperature before each plateau indicates that additional energy was being delivered to these locations prior to attaining boiling conditions. This might be due to heating by the hot water that is draining from condensation regions above the thermocouples. Note that these thermocouples are below and to the side of the heater.

The region above the heater along P2 [see Fig. 7-6(b)] did not show a pronounced flattening of the temperature-radius profile. The temperature-time plots in Fig. 7-6(b) show a change of slope. Some of the slope changes might be associated with boiling (e.g., thermocouples 60 and 61); but the others occurred at temperatures too low to be associated with boiling. A big leak of the packer in P2 was discovered on November 23, 1988. The leak might have started earlier. Air leaking from the packer could also decrease the temperature and change the slope of the temperature-time curves. However, a leaking packer would have a greater effect on the temperature measured from thermocouples closer to the packer (for example, 58 and 59). There was no such change of the slope of the temperature-time curve of thermocouples 58 and 59. Although we cannot completely rule out the effect of a leaking packer, we do not believe that it was significant. Therefore, in the region above the heater, boiling of the pore water did occur, but without any replenishment of pore water as was observed on the lower flank of the heater. The changes of slope in the temperature-time plots might be due to the cooling effect of water condensing in the region directly above, then draining down to the thermocouples.

Zimmerman and Blanford (1986) reported a phenomenon similar to that shown in Fig. 7-6(a) from their small-diameter heater experiment in G-Tunnel. One of their thermocouples showed a temperature plateau at approximately 95°C for about 17 days after which the temperature increased to over 200°C. They attributed this phenomenon to a heat pipe effect, which involves boiling of water in the rock matrix, transport of steam along fractures, condensation of steam into water in the cooler fracture, and return of the condensed water toward the heat source by capillary suction. However, a second thermocouple about 27 cm away, along the same borehole wall, did not register the same phenomenon.

Although the capillary-driven heat-pipe model fits some of the data, some observations are unexplained, such as the different phenomena that we observed in regions above and below the heater, and the sudden rise in temperature observed for thermocouples 88, 89, and 90 before reaching the boiling point. A model to explain the observed phenomena is constructed and reported by Lin et al. (1990), which involves the introduction of additional heat to the region of these thermocouples from hot condensate water drained from above.

Conclusions

We have determined the spatial distribution and temporal variation of temperature around a horizontally emplaced heater. A comparison of our results with modeling studies shows that for this test, heat conduction was the major heat transfer mechanism in the test region. Minor variations (to about 15%) in temperature might be caused by the presence or absence of fractures, the variation of initial moisture content, nonsymmetric heat flux from the heater, and cooling effect of the alcove wall. Fractures provide cooling by facilitating the movement of steam and water and, thereby, the transport of energy. Fracture mapping will therefore provide very important information to help with the interpretation of the temperature data in future tests. These results show that temperature measurements provide important information of the thermal-hydrological response of the rock mass to a thermal load.

To obtain a better sampling of the thermal field, the thermocouples should be arranged radially. Several thermocouple arrays will be needed to obtain a three-dimensional picture of the thermal transfer mechanism around a heater. The thermocouples should be more evenly distributed in space so that a thermal field can be accurately represented. For a horizontal heater test, the need for temperature sampling along a vertical line above and below the heater is noted.

Some uncertainties in temperature measurement were caused by the nonuniform temperature on the surface of the heater assembly. The temperature on top of the heater was about 10% greater than that at the bottom. In future tests, this effect should be removed to enable better interpretation of the in-situ response to the thermal load. A possible solution considered is to include baffles within the canister to prevent convection.

In the case of horizontal heater emplacement, the drying and condensation processes depend on locations relative to the heater. Gravity might have played an important role on the movement of water and steam in the horizontal emplacement test.

We have verified that thermocouples placed in thin-wall tubing measure the same temperature as those grouted shut in a borehole. This method of installing thermocouples will be adopted for future tests, so that thermocouples can be removed for in-test calibration and bad thermocouples can be replaced or repaired.

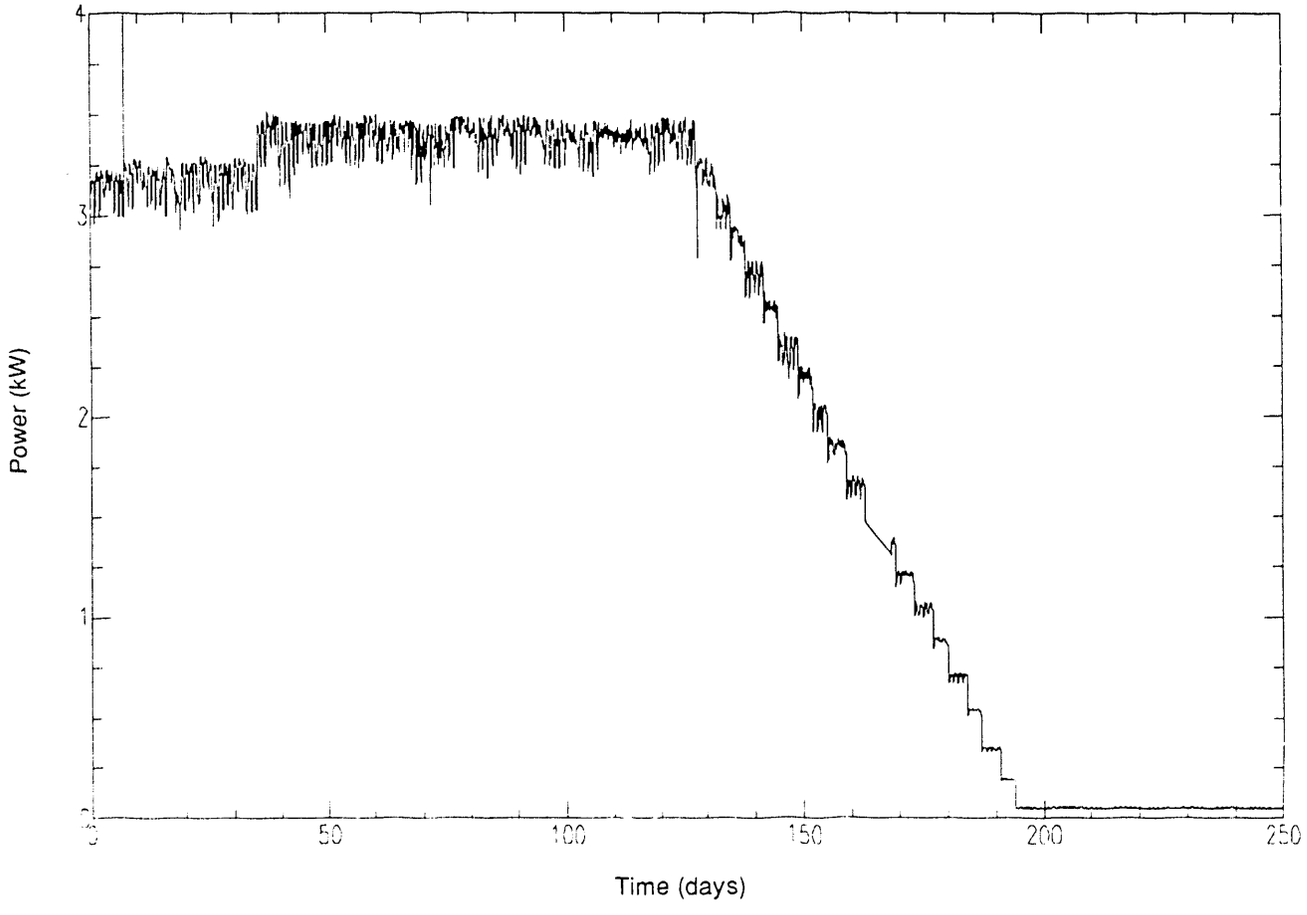

Figure 7-1. Heating history of the test.

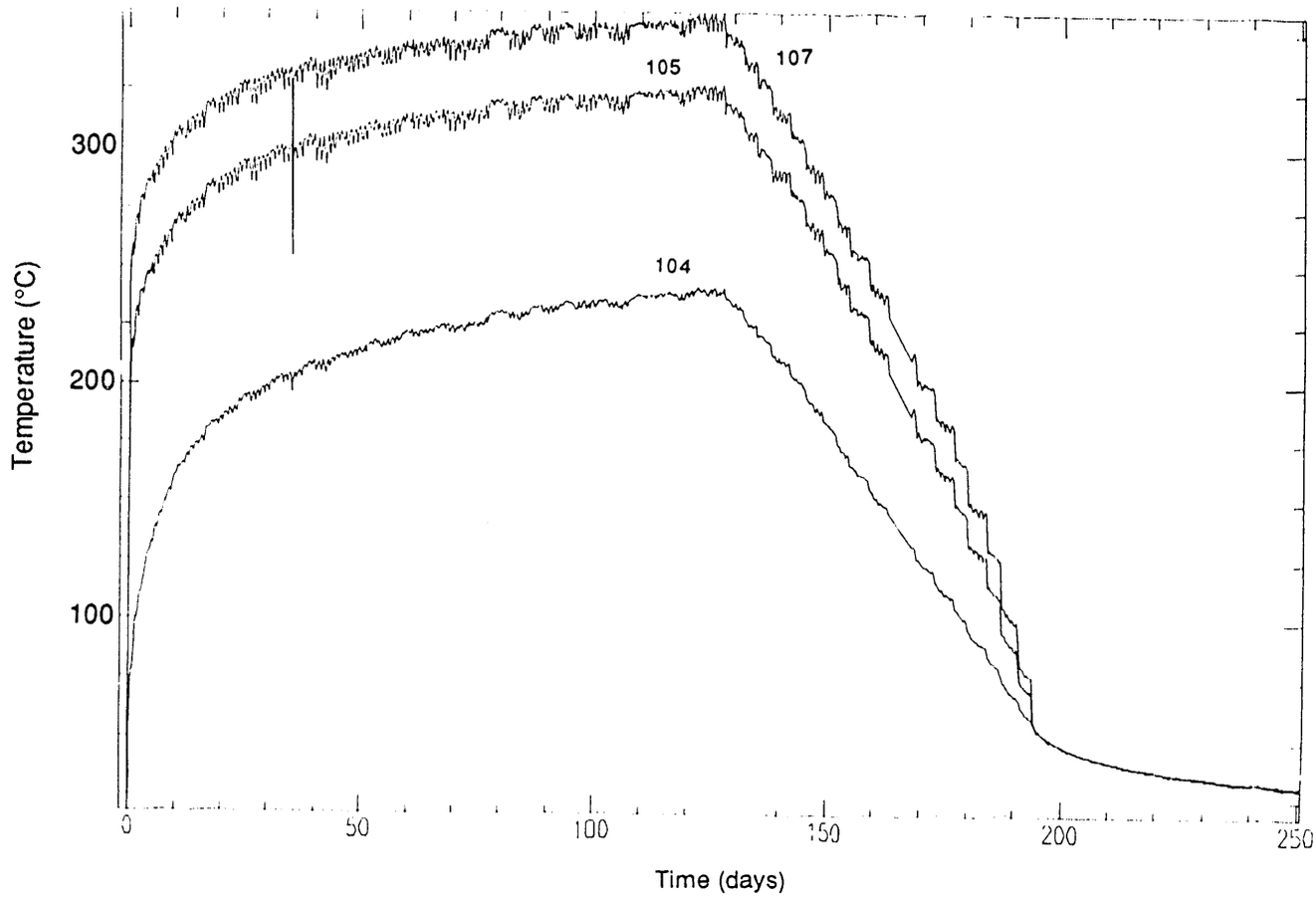

Figure 7-2. Temperature history on the heater and on the borehole wall. Thermocouples 107 and 105 are on the top and bottom of the heater, respectively; thermocouple 104 is on the bottom of the heater hole wall.

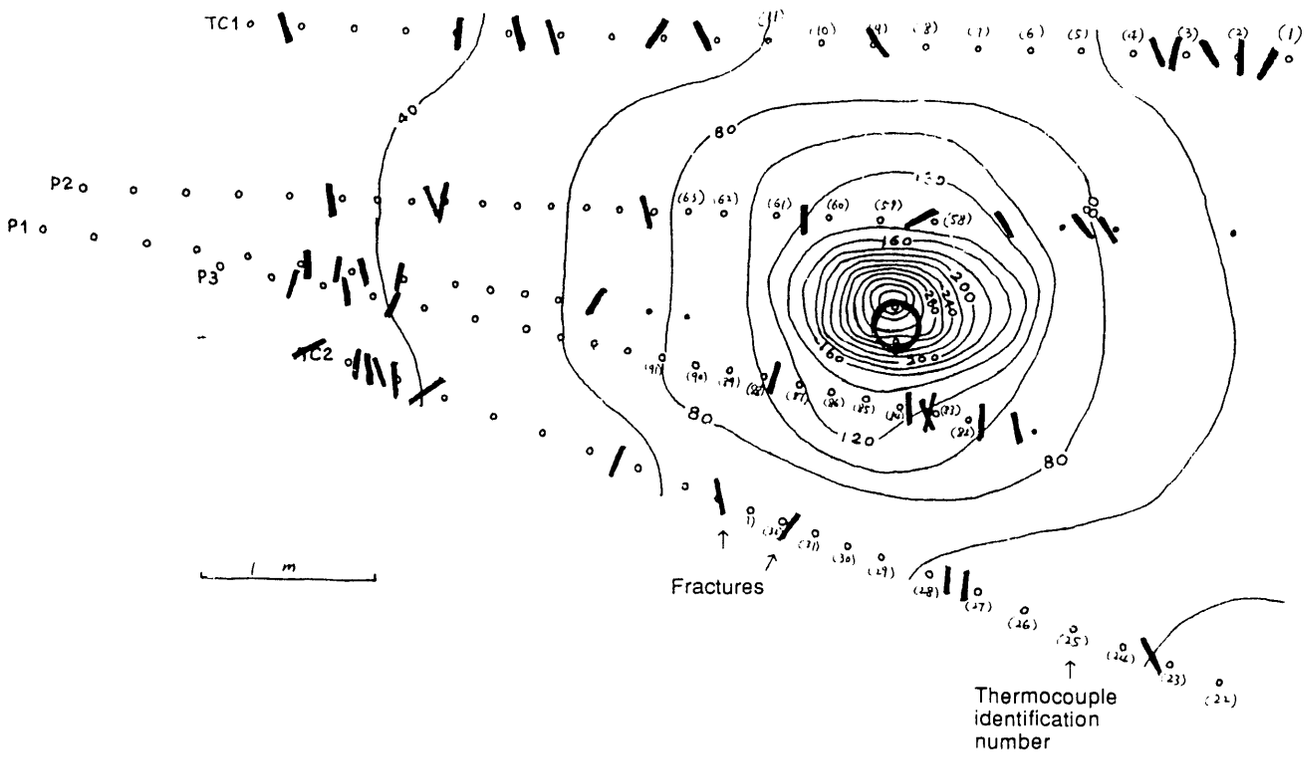

Figure 7-3. Location of thermocouples and major fractures observed in the boreholes. Also shown are the temperature contours measured on January 13, 1989. The numbers in parentheses are the thermocouple numbers as in the DAS.

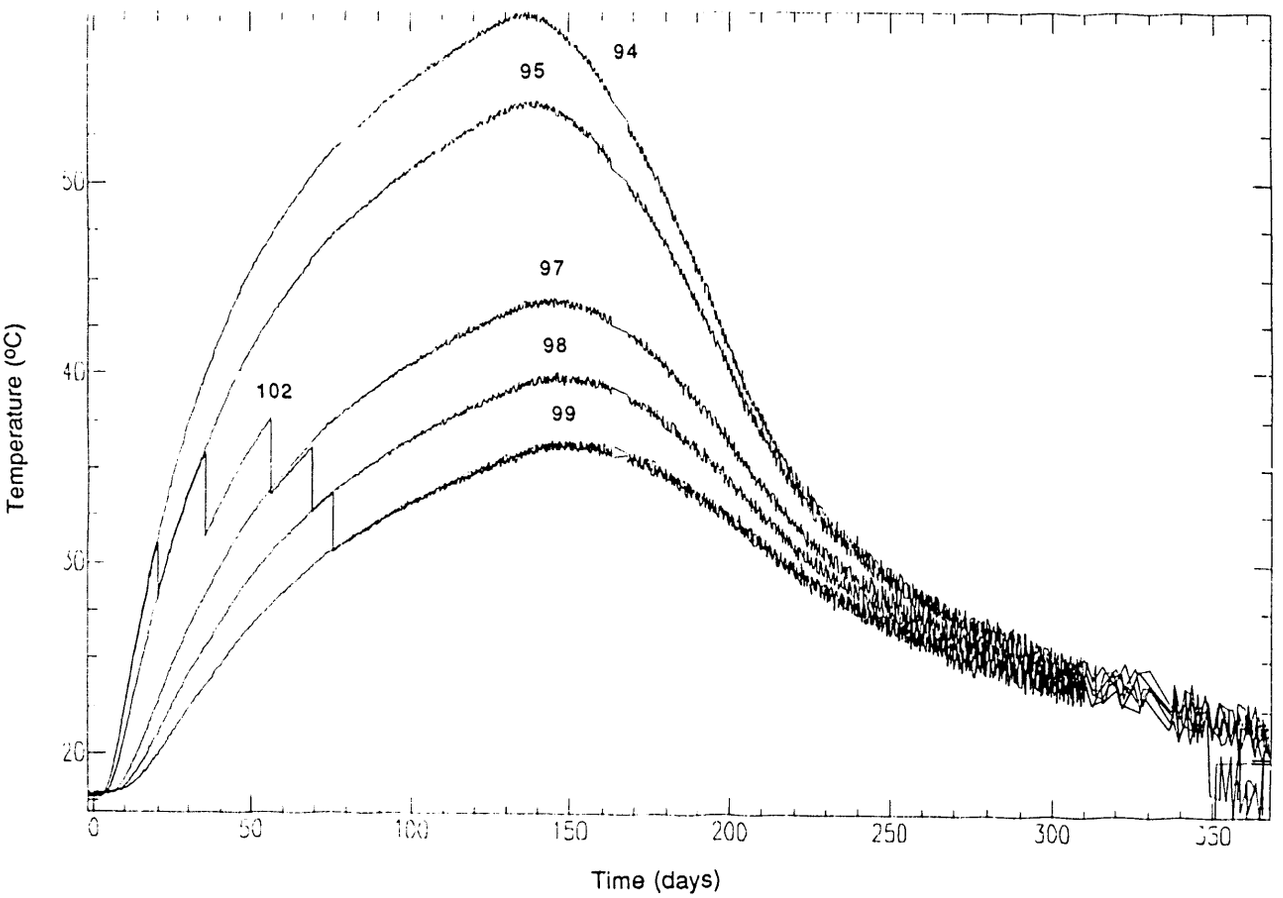

Figure 7-4. Temperature history of the traveling thermocouple (102) and the grouted thermocouples, numbered from 94 to 99.

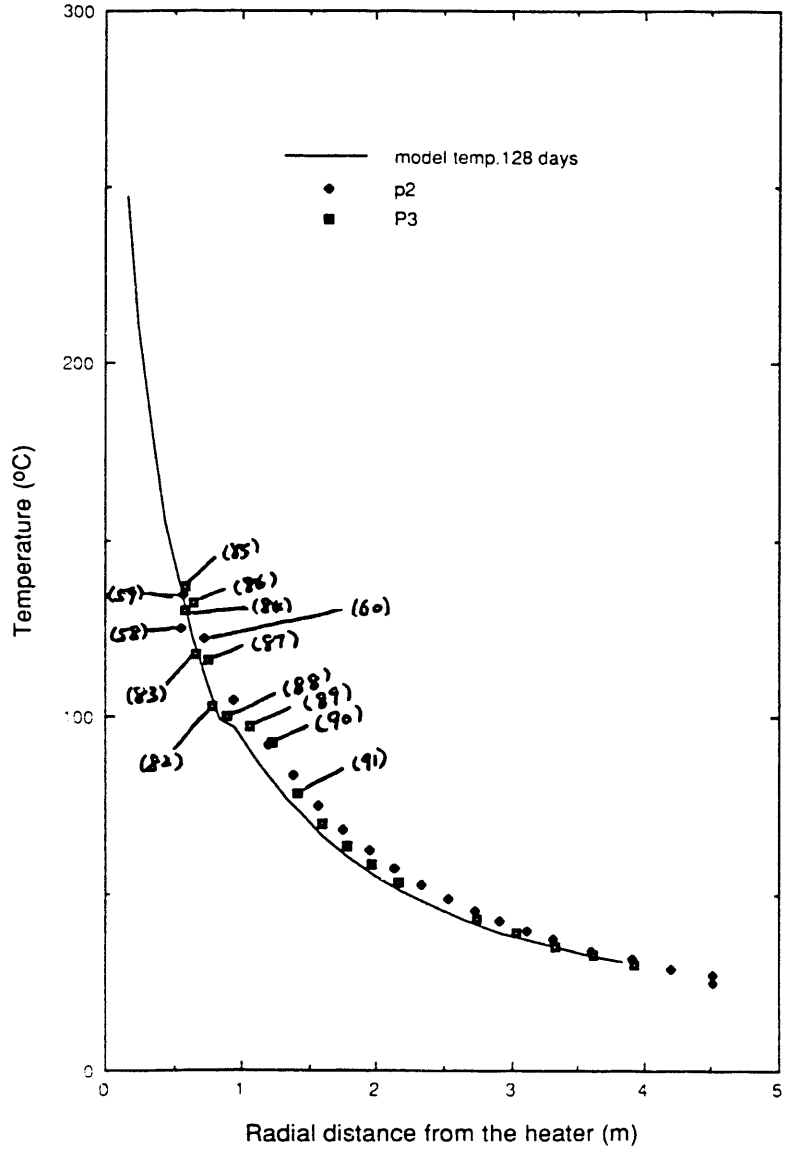

Figure 7-5. Temperature as a function of radial distance from the heater in P2 and P3 on January 13, 1989. The numbers on the curves are the thermocouple numbers.

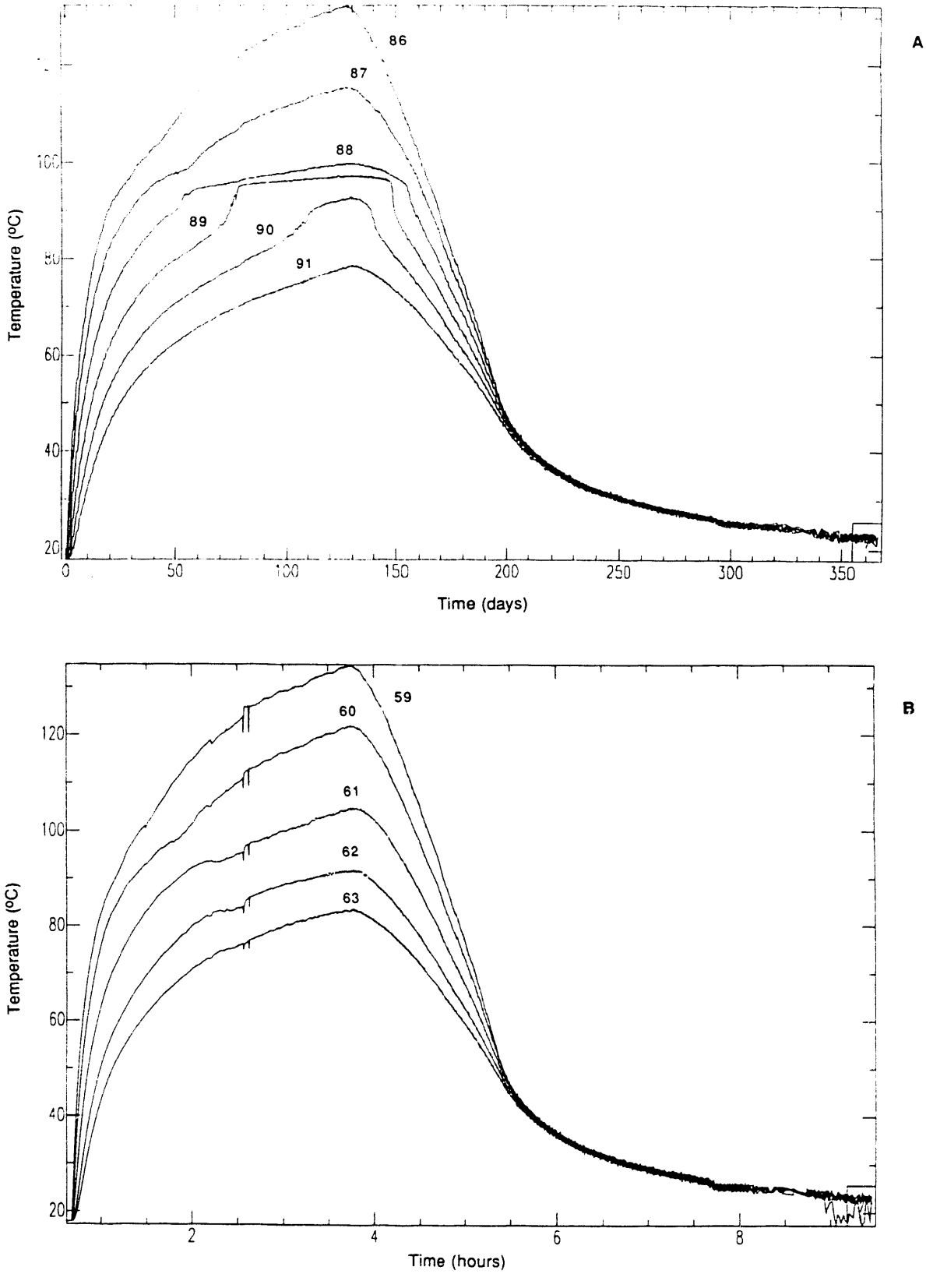

Figure 7-6. Temperature history at some of the thermocouples in (a) P3, below the heater and (b) P2, above the heater. The numbers on the curves are the thermocouple numbers.

Chapter 8

Summary of Results and Interpretations

Abelardo Ramirez

This report presents an overview of results obtained during the first Prototype Engineered Barrier System Field Test (PEBSFT) recently completed in G-Tunnel within the Nevada Test Site. The test described is a precursor to the Engineered Barrier Systems Field Tests (EBSFT) that will be conducted in the Exploratory Studies Facilities of the Yucca Mountain Project (YMP). The EBSFT will consist of in situ tests of the geohydrologic and geochemical environment in the near field (within a few meters) of heaters in welded tuff to simulate the thermal effects of waste packages. The PEBSFT was conducted to evaluate the applicability of measurement techniques, numerical models, and procedures for future EBSFT investigations. This report discusses the evolution of hydrothermal behavior during the first prototype test, including rock temperatures, changes in rock moisture content, matrix potentials, gas pressures, air permeability of fractures, and gas-phase humidity in the heater borehole.

The test included an accelerated thermal cycle to examine the effects of the heating and cooling phases of a thermal load. A heater was placed in an approximately horizontal heater borehole of 0.3-m diameter. The initial thermal loading for the 3-m (9.8-ft) long heater was approximately 3 kW (1.1 kW/m) and lasted 128 days. This initial thermal load per unit length of emplacement borehole was set higher than the loading expected for a typical spent fuel container (0.4–0.7 kW/m) in an attempt to increase the volume of rock to be disturbed in the relatively short period available for prototype testing and to create sufficiently high rock temperatures to drive two-phase fluid flow. The duration of this heating period was based on the criteria of heating the rock mass such that the boiling point isotherm moved approximately 0.6–0.7 m (2.0–2.3 ft) radially from the heater borehole wall. This spatial extent of heating affected a volume of rock large enough to include several fractures. Subsequently, the heater power was gradually decreased to 0.0 kW over a 68-day period. The total duration of the heating cycle was 196 days.

The PEBSFT described in this report has provided valuable experience that improves our ability to conduct the EBSFT planned for the Exploratory Shaft Facility in Yucca Mountain. The results to date from the PEBSFT have shown that, for the most part, environmental conditions expected to develop around a heater in welded tuff are as described in the Introduction; the results also suggest that some parts of the pretest conceptual model need to be modified. The test has also shown which of the measurement techniques and hardware performed adequately under realistic environmental conditions and which need to be modified or replaced. Also, the test has shown that vertical boreholes should be added to borehole layout near the heater borehole (horizontal emplacement) to better sample the vertical extent of the temperature and moisture fields.

The test confirmed many elements of the pretest conceptual model of hydrothermal behavior.

- Test results confirm that a dry zone developed around the heater borehole (refer to conceptual model in Fig. 2-5), and the degree of drying increased with proximity to the heater. A "halo" of increased saturation developed around the dry region and migrated away from the heater as rock temperatures increased. However, the "halo" was significantly smaller than expected.

- The predominant energy transfer mechanism was heat conduction.

- Fractures served as the predominant mass transfer paths for gases and liquids. Some of the fractures intercepting the heater borehole increase the penetration of hot-dry conditions into the rock mass. Sectors of the rock mass near fractures within the hot-dry region remained at a boiling temperature much longer than other sectors; this was probably caused by condensate moving along fractures into these regions from above (Fig. 2-6 shows a conceptual flow model within a fracture).

- During the portions of the test when the heater power was gradually reduced and eventually turned off, the dry region around the heater cooled and slowly regained water (refer to conceptual model in Fig. 2-7). A suction pressure gradient formed between regions depleted of water and regions farther from the heater that contained more water. Rewetting of the dry region occurred in rock adjacent to fractures. It is suggested that fractures accelerate rewetting by one or more of the following mechanisms: (1) provide flow paths for humid air to contact the dry region so that capillary condensation occurs along the fracture face, (2) allow binary diffusion of the air humidity from the fracture to the dry matrix, and (3) provide flow paths for water drips coming from saturated regions above the heater.

- Measurements of air permeability made along the heater borehole prior to heating show that the fracture system exhibits a strong heterogeneity in fracture permeability. Measurements made after the heater was turned off show that there was a general (small relative to the natural heterogeneity of permeability) increase in air permeability for the rock that reached the hottest temperatures.

Conceptual models have been developed based on the results shown here and in conjunction with the numerical modeling study to explain the movement of gas and liquid phase water in the rock within a few meters of the heater. In general, water vapor generated in a matrix block moves toward the closest fracture face (or surface of the heater borehole if the block is adjacent the borehole). Upon entering the fracture, water vapor tends to move radially outward through the fracture system until encountering condensation conditions. Due to the heater borehole moisture collection system and condensation on the heater packer, some of the vapor in the fractures moves radially inward toward the heater hole. Water that condenses above the heater drains downward through the fractures. Much of this downward flow intersects the boiling zone and is reboiled, thereby slowing the upward progress of the boiling front. Some downward flow of condensate was observed to be reboiled at the lower flank of the heater, thereby stabilizing the boiling front at that location. Water that condenses below the heater drains away from the boiling zone. Because matrix imbibition is slow relative to the condensate generation and drainage rates, most of the downward drainage of condensate below the heater leaves the system before it can be subsequently reboiled. It was also observed that the boiling zone effectively acts as an "umbrella" shielding the rock below the heater from the downward drainage of condensate generated above the heater. Rewetting of the rock above the heater and to one side of the heater was observed to be partially the result of condensate drainage in fractures. Throughout the fractured rock mass, rewetting also occurred via binary diffusion of water vapor (driven by relative humidity gradients) and via Darcy flow (driven by pressure gradients). As this water vapor reaches drier rock, it condenses along the fracture faces (by capillary condensation) and is imbibed by the matrix.

The test also yielded some surprises in terms of environmental conditions.

- The changes in moisture content were not radially symmetric relative to the heater axis. The drying front penetrated faster in the downward direction

(relative to the heater) during the maximum power phase of the test; this asymmetry is even more pronounced when compared to the temperature contours, which show higher temperatures above the heater. Rewetting conditions, on the other hand, penetrated the dry zone above the heater somewhat faster than the rock below. We recommend that, for future tests, vertical boreholes be added to borehole layout near the heater borehole (horizontal emplacement) to better sample the vertical extent of the temperature and moisture fields.

- Rewetting of the dry zone appears to have occurred primarily by capillary condensation of gas-phase humidity in the fractures; rewetting of the dry region by imbibition appears to be relatively insignificant, probably as a result of the accelerated power ramp-down curve used for this test.

- The temperature above the heater container was approximately 30°C (54°F) higher than the temperature below the container. This condition might be a consequence of hotter air accumulating at the top of the container.

- The amount of steam which invaded the heater borehole is much less than that predicted by scoping calculations. The reasons for this discrepancy remain unclear. Possible reasons include: (1) an inadequate system was used to collect and condense the steam invading the heater borehole, and (2) wetting characteristic curves were not available for the Grouse Canyon welded tuff, resulting in inaccurate modeling predictions.

Instrumentation Performance

The instrumentation performance for the various sensors exhibited considerable variability. As expected, temperature measurements made with thermocouples and resistance thermometer devices (RTD) show that both types of sensors are sufficiently rugged and accurate. Similarly, the neutron and gamma ray logging tools were demonstrated to be rugged enough to withstand temperatures of up to 70°C (manufacturer's specification); in borehole locations where temperatures were above 70°C, the probe was removed periodically to allow probe temperatures to drop below 70°C. Another sensor exhibiting reliable performance was the capacitance sensor, used to measure air humidity in the heater borehole.

The experience gained during the test suggests that some of the measurement techniques and hardware used need to be modified.

1. The air permeability of the fracture network was higher than anticipated when the components of the air permeability system were selected; as a result, optimal test pressures were lower than anticipated. Future air permeability systems need to use pressure gages with lower pressure rating, higher sensitivity, and higher precision.

2. The field calibration process for the high frequency electromagnetic (HFEM) system was found to be inadequate and was modified; also, special equipment racks were found to be necessary and were purchased to provide dust protection for the up-hole instrumentation.

3. Laboratory measurements of air humidity made with the microwave resonator showed that, in principle, the technique is sufficiently sensitive. However, field results indicated that its calibration curves shifted, probably as a result of corrosion

caused by water collecting inside the sensor; a new resonator design incorporating materials with a higher corrosion resistance has been proposed.

4. Suction pressure measurements made with thermocouple psychrometers suggest a hydrologic scenario consistent, in a qualitative sense, with that expected a priori and with changes in moisture content measured during the test. However, some of the psychrometers gave inconsistent readings for unknown reasons, and the calibration process used has yet to be demonstrated as valid over the range of relevant test temperatures.

5. Gas pressure transducers used during the early part of the test showed a significant change in their calibration characteristics as the pressures changed. These sensors were replaced with sensors from a different manufacturer and the problem was solved.

6. The system used to collect and condense steam within the heater borehole may have collected only a small fraction of the steam available; this system will need to be modified to provide accurate measurement of steam flux into the heater borehole without removing the steam from the borehole.

References

Beiriger, J., and W. B. Durham (1984), *SEM Studies of Stressed and Irradiated Climax Stock Quartz Monzonite*, Lawrence Livermore National Laboratory, Livermore, CA, UCID-20052. NNA.900806.0149.

Bish, D. L., and D. P. Vaniman (1985), *Mineralogic Summary of Yucca Mountain, Nevada*, Los Alamos National Laboratory, Los Alamos, NM, LA-10543-MS. NNA.870407.0330.

Briscoe, R. D. (1984), "Thermocouple Psychrometers for Water Potential Measurements," *Proceedings, NATO Advance Study Institute on Agricultural Instrumentation*, II Cicco (Pisa, Italy, May 27–June 9), pp. 1–14. NNA.891212.0024.

Brown, R. W., and D. L. Bartos (1982), *A Calibration Model for Screen-Caged Peltier Thermocouple Psychrometers*, U.S. Department of Agriculture, Washington, D.C., Forest Service Research Paper INT-293. NNA.891221.0013.

Buscheck, T., and J. Nitao (1988), *Preliminary Scoping Calculations of Hydrothermal Flow in Variably Saturated, Fractured, Welded Tuff During Engineered Barrier Design Test at the Yucca Mountain Exploratory Shaft Test Site*, Lawrence Livermore National Laboratory, Livermore, CA, UCID-21571. NNA.890224.0009.

Buscheck, T., and J. Nitao (1989), "Preliminary Scoping Calculations of Hydrothermal Flow," in *Prototype Engineered Barrier System Field Tests (PEBSFT), Progress Report Through November 1, 1988*, A. L. Ramirez and D. G. Wilder, Eds., Lawrence Livermore National Laboratory, Livermore, CA, UCID-21640. NNA.910207.0024.

Buscheck, T., and J. Nitao (1991), *Modeling Hydrothermal Flow in Variably Saturated, Fractured, Welded Tuff During the Prototype Engineered Barrier System Field Test of the Yucca Mountain Project*, Lawrence Livermore National Laboratory, Livermore, CA, UCRL-ID-106521. (Readily Available).

Clarke, E. C. W., and D. N. Glew (1985), "Evaluation of the Thermodynamic Functions for Aqueous Sodium Chloride from Equilibrium and Calorimetric Measurements Below 154°C," *J. Phys. Chem. Ref. Data* **14**(2), 489–610. NNA.910410.0170.

Daily, W., and A. Ramirez (1989), "Evaluation of Electromagnetic Tomography to Map In Situ Water in Heated Welded Tuff," *Water Resources Res.* **25**(6), 1083–1096. NNA.91326.0097.

Daily, W., A. L. Ramirez, T. S. Ueng, and V. R. Latorre (1990), "High Frequency Electromagnetic Tomography," *Proc. Nuclear Waste Isolation in the Unsaturated Zone, Focus '89*, (Am. Nuc. Soc., La Grange Park, IL), pp. 409–416. NNA.910326.0098.

Daily, W., V. R. Latorre, and H. M. Buettner (1989), *Calibration of a High Frequency Electromagnetic Measurement System Used in Geophysics*, Lawrence Livermore National Laboratory, Livermore, CA, UCRL-102049; submitted to IEEE Geosciences and Remote Sensing. NNA.900312.0199.

Daily, W., W. Lin, and T. Buscheck (1986), "Hydrology of Topopah Spring Tuff—Laboratory Measurements," *J. Geophys. Res.* **92**(B8), 7854–7864. HQS.880517.2416.

Dines, K. A., and R. J. Lytle (1979), "Computed Geophysical Tomography," *Proc. IEEE* **67**, 1065–1073. NNA.891109.0067.

Freeman, M. S., R. N. Nottenburg, and J. B. DuBow (1979), "An Automated Frequency Domain Technique for Dielectric Spectroscopy of Materials," *J. Phys. E.: Sci. Instrum.* **12**, 899–903. NNA.910326.0099.

Katz, D. L., D. Cornell, R. Kobayashi, F. H. Poettmann, J. A. Vary, J. R. Elenbaas, and C. F. Weinaug (1959), *Handbook of Natural Gas Engineering*, (McGraw-Hill, New York). NNA.900626.0212.

Klavetter, E. A., and R. R. Peters (1986), *Estimation of Hydrologic Properties of an Unsaturated, Fractured Rock Mass*, Sandia National Laboratories, Albuquerque, NM, Report No. SAND84-2642. NNA.870317.0738.

Lang, A. R. G. (1967), "Osmotic Coefficients and Water Potentials of Sodium Chloride Solutions from 0 to 40°C," *Aust. J. Chem.* **20**, 2017–2023. NNA.891109.0068.

Lee, K., and T. Ueng (1989), "Permeability Tests" in *Prototype Engineered Barrier System Field Tests (PEBSFT), Progress Report Through November 1, 1988*, A. L. Ramirez and D. G. Wilder, Eds., Lawrence Livermore National Laboratory, Livermore, CA, UCID-21640. NNA.910207.0024.

Lin, W., and W. Daily (1984), *Transport Properties of Topopah Spring Tuff*, Lawrence Livermore National Laboratory, Livermore, CA, UCRL-53602. HQS.880517.2486.

Lin, W., A. Ramirez, and D. Watwood (1990), *Temperature Measurements from Prototype Engineered Barrier System Field Tests*, Lawrence Livermore National Laboratory, Livermore, CA, UCRL-ID-104757. (Readily Available).

Montan, D. (1986), *Thermal Calculations Pertaining to Experiments in the Yucca Mountain Exploratory Shaft*, Lawrence Livermore National Laboratory, Livermore, CA, UCID-20780. NNA.900816.0011.

Nitao, J. J. (1988), *Numerical Modeling of the Thermal and Hydrological Environment around a Nuclear Waste Package Using the Equivalent Continuum Approximation: Horizontal Emplacement*, Lawrence Livermore National Laboratory, Livermore, CA, UCID-21444. NNA.890317.0021.

Nitao, J. J. (1989), *V-TOUGH—An Enhanced Version of the TOUGH Code for the Thermal and Hydrologic Simulation of Large-Scale Problems in Nuclear Waste Isolation*, Lawrence Livermore National Laboratory, Livermore, CA, UCID-21954. NNA.900508.0040.

Nitao, J. J., and T. Buscheck (1989), *On the Movement of a Liquid Front in an Unsaturated, Fractured Porous Medium, Part I*, Lawrence Livermore National Laboratory, Livermore, CA, UCID-21714. NNA.891130.0050.

Ramirez, A., and D. Wilder (Eds.) (1989), *Prototype Engineered Barrier System Field Tests (PEBSFT), Progress Report Through November 1, 1988*, Lawrence Livermore National Laboratory, Livermore, CA, UCID-21640. NNA.910207.0024.

Ramirez, A. L. , R. C. Carlson, and T. A. Buscheck (1990), *In Situ Changes in the Moisture Content of Heated Welded Tuff Based on Thermal Neutron Measurements*, Lawrence Livermore National Laboratory, Livermore, CA, UCRL-ID-104715. (Readily Available).

Ramirez, A. L., and W. D. Daily (1987), "Evaluation of Alterant Geophysical Tomography in Welded Tuff," *J. Geophys. Res.* 92(B8), 7843–7853. NNA.900115.0271.

Wang, H. F., B. P. Bonner, S. R. Carlson, B. J. Kowallis, and H. G. Heard (1989), "Thermal Stress Cracking in Granite," *J. Geophys. Res.* 94(B2), 1745–1758. NNA.910131.0265.

Watwood, D., and J. Beatty (1989), "Data Acquisition System" in *Prototype Engineered Barrier System Field Tests (PEBSFT), Progress Report Through November 1, 1988*, A. L. Ramirez and D. G. Wilder, Eds., Lawrence Livermore National Laboratory, Livermore, CA, UCID-21640. NNA.910207.0024.

Wilder, D. G. (1990), "Engineered Barrier Systems and Canister Orientation Studies for the Yucca Mountain Project, Nevada," in *Proceedings of the International Symposium on Unique Underground Structures*, Vol. 2, (Colorado School of Mines, U.S. Bureau of Reclamation), p. 62-1. NNA.910711.0041.

Yow, J., Jr. (1985), *Concept for Waste Package Environment Tests in the Yucca Mountain Exploratory Shaft*, Lawrence Livermore National Laboratory, Livermore, CA, UCID-20450. NNA.870522.0041.

Zimmerman, R. M., and M. K. Blanford (1986), "Expected Thermal and Hydrothermal Environments for Waste Emplacement Holes Based on G-Tunnel Heater Experiments," in *27th U.S. Symposium on Rock Mechanics*, H. Hartman, Ed., (Society of Mining Engineers, Inc., Littleton, CO), pp. 874–882. NNA.891212.0018.

Zimmerman, R. M., and R. E. Finley (1986), *Summary of Geomechanical Measurements Taken in and Around the G-Tunnel Underground Facility, NTS*, Sandia National Laboratories, Albuquerque, NM, Report No. SAND86-1015. NNA.870526.0015.

Bibliography of Related Reports

Preliminary Evaluation of Alterant Geophysical Tomography in Welded Tuff, A. Ramirez and W. Daily, UCID-20289, Lawrence Livermore National Laboratory, Livermore, CA, December 1984.

Evaluation of Alterant Geophysical Tomography in Welded Tuff, A. Ramirez and W. Daily, in Journal of Geophysical Research, Vol. 92, No. B8, pp. 7843–7853, (July 1987); also available as UCID-20675, Lawrence Livermore National Laboratory, Livermore, CA, February 1986.

Thermomechanical Scoping Calculations for the Waste Package Environment Tests, T. R. Butkovich and J. L. Yow, Jr., Lawrence Livermore National Laboratory, Livermore, CA, UCID-20758, March 1986.

Thermal Calculations Pertaining to Experiments in the Yucca Mountain Exploratory Shaft, D. N. Montan, UCID-20780, Lawrence Livermore National Laboratory, Livermore, CA, March 1986.

Preliminary Evaluation of an Electromagnetic Experiment to Map in Situ Water in Heated Welded Tuff, W. Daily and A. Ramirez, UCRL-96816, Lawrence Livermore National Laboratory, Livermore, CA, February 1987.

An Experiment to Determine Drilling Water Imbibition by in Situ Densely Welded Tuff, W. Daily and A. Ramirez, UCID-21249, Rev. 1, Lawrence Livermore National Laboratory, Livermore, CA, April 1987.

Test Concept for Waste Package Environment Tests at Yucca Mountain, J. L. Yow, Jr., in 28th U.S. Symposium on Rock Mechanics, Tucson, AZ, pp. 1035–1042, (June 26–July 1, 1987); also available as UCRL-95568, Lawrence Livermore National Laboratory, Livermore, CA, June 1987.

Estimates of the Hydrologic Impact of Drilling Water on Core Samples Taken from Partially Saturated Densely Welded Tuff, T. Buscheck and J. Nitao, UCID-21294, Lawrence Livermore National Laboratory, Livermore, CA, September 1987.

Estimates of the Width of the Wetting Zone Along a Fracture Subjected to an Episodic Infiltration Event in Variably Saturated, Densely Welded Tuff, T. Buscheck and J. Nitao, UCID-21579, Lawrence Livermore National Laboratory, Livermore, CA, May 1988.

Preliminary Scoping Calculations of Hydrothermal Flow in Variably Saturated, Fractured, Welded Tuff During the Engineered Barrier Design Test at the Yucca Mountain Exploratory Shaft Test Site, T. Buscheck and J. Nitao, UCID-21571, Lawrence Livermore National Laboratory, Livermore, CA, November 1988.

Evaluation of Electromagnetic Tomography to Map in Situ Water in Heated Welded Tuff, W. Daily and A. Ramirez, Lawrence Livermore National Laboratory, in Water Resources Research, Vol. 25, No. 6, pp. 1083–1096, June 1989.

Prototype Engineered Barrier System Field Test-Progress Report, A. Ramirez, T. Buscheck, R. Carlson, W. Daily, V. Latorre, K. Lee, W. Lin, N. Mao, D. Towse, T. Ueng, and D. Watwood, submitted to Proceedings of the ANS Topical Meeting, Focus '89 Nuclear Waste Isolation in an Unsaturated Zone, Las Vegas, NV (September 18–21, 1989); also available as UCRL-101615, Lawrence Livermore National Laboratory, Livermore, CA, July 1989.

Microwave Measurements of Water Vapor Partial Pressure at Temperatures up to 350°C, V. Latorre, submitted to Proceedings of the ANS Topical Meeting, Focus '89 Nuclear Waste Isolation in an Unsaturated Zone, Las Vegas, NV (September 18–21, 1989); also available as UCRL-101866, Lawrence Livermore National Laboratory, Livermore, CA, September 1989.

Calibration of a High Frequency Electromagnetic Measurement System Used in Geophysics, W. Daily, V. Latorre, and H. Buettner, submitted to IEEE Geoscience and Remote Sensing Journal; also available as UCRL-102049, Lawrence Livermore National Laboratory, Livermore, CA, September 1989.

High Frequency Electromagnetic Tomography, A. Ramirez, W. Daily, T. Ueng, and V. Latorre, UCRL-100624, Lawrence Livermore National Laboratory, Livermore, CA, September 1989.

High Frequency Electromagnetic Tomography, W. Daily, A. Ramirez, T. Ueng, and V. Latorre, submitted to Proceedings of the ANS Topical Meeting, Focus '89 Nuclear Waste Isolation in an Unsaturated Zone, Las Vegas, NV (September 18–21, 1989); also available as UCRL-101865, Lawrence Livermore National Laboratory, Livermore, CA, September 1989.

Prototype Heater Test of the Environment Around a Simulated Waste Package, A. Ramirez, T. Buscheck, R. Carlson, W. Daily, V. Latorre, K. Lee, W. Lin, N. Mao, D. Towse, T. Ueng, and D. Watwood, in International High Level Radioactive Waste Management Conference, Las Vegas, NV, Vol. 2, pp. 870–881, 1990; also available as UCRL-101693, Lawrence Livermore National Laboratory, Livermore, CA, December 1989.

Prototype Engineered Barrier System Field Test-Progress Report through November 1988, A. Ramirez and D. Wilder (Eds.), UCID-21640, Lawrence Livermore National Laboratory, Livermore, CA, December 1989.

Air Injection Field Measurements to Determine the Effect of a Heat Cycle on the Permeability of Welded Tuff, K. H. Lee, and T-S. Ueng, UCRL-ID-105163, Lawrence Livermore National Laboratory, Livermore, CA, October 1990.

Thermocouple Psychrometer Measurements of In Situ Water Potential Changes in Heated, Welded Tuff, N-H. Mao and H. F. Wang, UCRL-ID-104729, Lawrence Livermore National Laboratory, Livermore, CA, September 1990.

In Situ Changes in the Moisture Content of Heated Welded Tuff Based on Thermal Neutron Measurements, A. Ramirez, R. Carlson, and T. Buscheck, UCRL-ID-104715, Lawrence Livermore National Laboratory, Livermore, CA, August 1990.

Appendix A
Effective Porosity and Water Permeability of G-Tunnel Tuff Samples

We have measured the effective porosity of 25 tuff samples selected from the cores (including the overcores) of the horizontal emplacement prototype test in G-Tunnel at NTS. The effective porosity of a sample was calculated from the saturated and dry densities of the sample. To determine the saturated density, a sample was placed in water under a pressure of about 100 psi until its weight remained unchanged for at least a few days. The final weight of the sample was assumed to be the saturated weight. Then the sample was put in a vacuum oven at 35°C, again, until its weight remained unchanged for a few days. The weight was assumed to be the dry weight. The density was calculated from the measured weight and the sample volume. The samples were cylinders of either 2.54 cm in diameter drilled in laboratory from bigger cores, or sections of various lengths, cut from the 4.7-cm diameter cores drilled in G-Tunnel before the test.

The porosity data are listed in Table A-1, where the samples are identified by borehole name and depth (in feet), such as "P2-17.6-1," which means the sample was the No. 1 sample from P2 hole at a depth of 17.6 feet. The average porosity of the 25 samples is 12.8% with a standard deviation of 2.3%. Four of the samples in Table A-1 (P1-17.5-1, P1-17.5-2, P2-17.6-1, and P2-17.6-2) were the postheating samples. All others were the preheating samples.

Saturated water permeability was measured on sample H1-20-2. The confining pressure was 5 MPa. Four measurements were made at pore pressures of 0.4, 0.45, 1.08, and 1.51 MPa. The permeability values were 0.9, 1.1, 0.9, and 1.9 microdarcy, respectively. The uncertainty of the permeability measurements could be as high as 30%, especially for the low permeability values, mainly caused by the small flow rate of water.

Table A-1. Effective Porosity of G-Tunnel Tuff Samples

Sample	Diameter (cm)	Length (cm)	Porosity (%)
H1-20-1	2.55	2.60	10.2
H1-22.7-1	2.55	2.58	13.1
H1-22.7-2	2.55	2.60	11.9
H1-26.2-1	2.55	2.54	9.8
H1-26.2-2	2.55	2.45	11.1
P1-17.5-1	2.55	2.64	10.5
P1-17.5-2	2.55	2.55	10.6
P2-17.6-1	2.55	2.52	13.6
P2-17.6-2	2.55	2.59	16.2
NE2A-14.6	2.55	2.19	12.0
NE2A-17.4	2.55	2.49	14.2
NE3-23.7	2.55	2.43	11.8
NE4-23.2	2.55	2.63	13.3
P1-13.3	2.55	2.18	13.0
P2-16.8	2.55	2.57	16.0
NE3-23.5	4.39	2.42	14.7
NE7-16.7	4.76	2.45	10.4
P1-13.5	4.76	2.51	13.5
P2-13.6	4.76	2.57	13.5
P2-16.5	4.75	2.48	19.7
TC1-17.7	4.76	2.49	10.7
NE2A-15	4.75	2.48	13.8
NE2A-17.3	4.75	2.52	13.2
NE4-23.3	4.44	2.48	12.9
NE5-21	4.45	2.61	11.3

The following number is for Office of Civilian Radioactive Waste Management Records Management purposes only and should not be used when ordering this document:

Accession Number: NNA.910711.0047

END

DATE FILMED

11/01/91